

Copyright
by
Gihye Shin
2016

The Dissertation Committee for Gihye Shin
certifies that this is the approved version of the following dissertation:

**A subgrid approach for unresolved topography in shallow
water hydrodynamic modeling**

Committee:

Ben R. Hodges, Supervisor

Daene C. McKinney

Desmond F. Lawler

M. Bayani Cardenas

Paola Passalacqua

**A subgrid approach for unresolved topography in shallow
water hydrodynamic modeling**

by

Gihye Shin, B.S.E.; M.S.C.E.

DISSERTATION

Presented to the Faculty of the Graduate School of
The University of Texas at Austin
in Partial Fulfillment
of the Requirements
for the Degree of

DOCTOR OF PHILOSOPHY

THE UNIVERSITY OF TEXAS AT AUSTIN

December 2016

Dedicated to my parents, Hyunseon Suh and Donghyuk Shin.

Acknowledgments

I would like to express my truthful gratitude to my advisor, Dr. Ben R. Hodges for his support during my PhD study. He encouraged me to accomplish my research, and guided me in all the time of writing. I am truly grateful to the rest of my committee: Dr. Daene C. McKinney, Dr. Desmond F. Lawler, Dr. M. Bayani Cardenas, and Dr. Paola Passalacqua. I thank all my friends in Austin and in South Korea, who have been a great consolation to me during this long journey. Lastly, I express my thanks to K-water (Korea Water Resources Corporation) and my colleagues there, who supported me during the study.

And first and foremost, I thank my parents. I have always been proud of being your daughter, and I will be proud of it.

A subgrid approach for unresolved topography in shallow water hydrodynamic modeling

Publication No. _____

Gihye Shin, Ph.D.

The University of Texas at Austin, 2016

Supervisor: Ben R. Hodges

This study develops methods to represent the effect of subgrid scale topography for shallow water hydrodynamic models using Cartesian grids. Neglect of subgrid scale topographic variability is recognized as causing misrepresentation of wetting and drying processes (Defina, 2000). Subgrid topography has been previously parameterized at model-resolved grid scales using data from high-resolution digital elevation models to capture flow area and volume effects (e.g., Casulli, 2009), but proposed approaches have neglected key aspects of flow resistance. Form drag exerted by unresolved subgrid features cannot be arbitrarily neglected for shallow flow dynamics as it introduces complexity through directional variability. That is, the conventional approach to modeling subgrid frictional effects is through drag coefficients that apply identically to all flow directions through a grid cell; however, subgrid features can introduce directional bias through form drag, e.g., an embankment that blocks flow in only one direction.

In the present work, two new model schemes were developed to address the frictional forcing on subgrid scale. These schemes are extensions of the subgrid modeling ideas of [Volp et al. \(2013\)](#) and [Casulli \(2009\)](#). The first new scheme is a subgrid drag model that determines directional drag coefficients representing the integrated and directionally-biased effects of subgrid drag. The second new scheme is a subgrid momentum model using the integrated fluxes through faces of a grid cell to represent subgrid forces and acceleration at the resolved-scale interface between two grid cells. The combination of these two methods is demonstrated to provide an approach to representing subgrid physical processes that have been missing in prior models.

The new subgrid models were implemented in the Fine Resolution Environmental Hydrodynamics Model (Frehd) and validated using model-model comparisons at fine and coarse grid resolution. The validation test cases use real-world estuarine topography of a section from a 1×1 m lidar survey of the Nueces River Delta (Texas, USA). The new subgrid models are shown to reduce discrepancies between coarse-grid and fine-grid simulations over the time-space domain. Of key importance is that the new models can represent the flow deflection by subgrid topographic obstructions that cannot be captured without directional drag coefficients. This study indicates that application of the new subgrid modeling approaches can reduce grid-scale dependency that otherwise requires finer grid resolution to adequately capture flow physics.

Table of Contents

| | |
|---|------------|
| Acknowledgments | v |
| Abstract | vi |
| List of Tables | xi |
| List of Figures | xii |
| Chapter 1. Introduction | 1 |
| 1.1 Unresolved topography and subgrid methods | 1 |
| 1.2 Research objectives and approach | 18 |
| 1.3 Contributions to science and technology | 20 |
| 1.4 Dissertation outline | 21 |
| Chapter 2. Subgrid Methods | 23 |
| 2.1 Prior work in subgrid geometric parameterization | 23 |
| 2.2 Prior work in subgrid friction parameterization | 25 |
| Chapter 3. Fine Resolution Environmental Hydrodynamics Model | 30 |
| 3.1 Introduction | 30 |
| 3.2 Numerical method | 30 |
| 3.3 2D shallow water equations | 33 |
| 3.4 Bottom friction model | 34 |
| 3.5 Discrete free-surface solution | 35 |
| Chapter 4. Subgrid Drag Model | 39 |
| 4.1 Introduction | 39 |
| 4.2 Model formulation | 42 |

| | |
|---|------------|
| Chapter 5. Subgrid Momentum Model and Solution | 53 |
| 5.1 Introduction | 53 |
| 5.2 Subgrid momentum model | 54 |
| 5.3 Model solution | 64 |
| 5.4 Subgrid topography sampling | 70 |
| Chapter 6. Validation and Verification of Subgrid Models | 74 |
| 6.1 Introduction | 74 |
| 6.2 Numerical experiments, reference, and control cases | 74 |
| 6.3 Test bathymetry | 77 |
| 6.4 Boundary conditions and model parameters | 77 |
| 6.5 Standard statistical metrics | 82 |
| 6.6 Test results and discussion | 89 |
| 6.7 Global indicators for evaluation of subgrid models | 133 |
| Chapter 7. Conclusions and Future Works | 147 |
| 7.1 Addressing the research objectives | 147 |
| 7.2 Recommendation for future work | 149 |
| Appendices | 150 |
| Appendix A. Nueces Delta and Restoration Efforts | 151 |
| A.1 Geography and climate | 151 |
| A.2 Threats to the Nueces Delta | 152 |
| A.3 Restoration effort for the Nueces Delta | 154 |
| A.4 Role of the Frehd model for restoring the Nueces Delta | 159 |
| Appendix B. Free-surface Solution Applying the Flux Integration Approach for the flow continuity | 162 |
| B.1 Flow continuity equation | 162 |
| B.2 Momentum conservation equation | 163 |
| B.3 Free-surface elevation solution | 165 |
| Appendix C. Definition of Subgrid Quantities for New Subgrid Model | 167 |

| | |
|----------------------------------|-----|
| Appendix D. Look-up Table Scheme | 170 |
| Bibliography | 173 |
| Vita | 188 |

List of Tables

| | | |
|-----|---|-----|
| 6.1 | Run cases | 76 |
| 6.2 | Absolute mean errors | 90 |
| 6.3 | Average and standard deviation of the Willmott Skill Score | 90 |
| 6.4 | Absolute mean errors of all the experiments and control | 121 |
| 6.5 | Willmott Skill Scores of all the experiments and control | 122 |
| 6.6 | Time fraction and error metrics of the experiments and the control in the test section A | 132 |
| 6.7 | Magnitude of global indicators for the test bathymetries | 145 |
| A.1 | Environmental flow recommendations for the Nueces Delta and Bay . | 158 |

List of Figures

| | | |
|-----|--|----|
| 1.1 | Locally refined grid schemes in time-space domain | 3 |
| 1.2 | A representative cross-section of a grid cell with resolved topography (left) and unresolved topography (right). The nomenclature, $d\eta$ denotes a change of the free-surface elevation (η), Z_b and $\max z_b$ denote the resolved-grid bottom elevation and the highest subgrid elevation, respectively. | 6 |
| 1.3 | Storage volume (V) of fine grid bathymetry and coarse grid bathymetry in relation with a change of the surface elevation (η). The nomenclature, Z_b and $\max z_b$ denote the resolved grid bottom elevation and the highest subgrid elevation, respectively. | 7 |
| 1.4 | A representative cross-section of a grid cell with resolved topography (left) and unresolved topography (right). The nomenclature, \bar{u} and C_{Dc} denote the velocity and drag coefficient of the resolved grid cell; u_i and C_{Di} denote the local velocity and local drag coefficient at the location i ($i \in \{1, 2, \dots, 5\}$); and A_f denotes a representative flow area of the grid cell. | 9 |
| 1.5 | A cross-section of two neighboring grid cells with resolved topography (left) and unresolved topography (right). Unresolved subgrid topographic features: (top) subgrid embankments, (middle) subgrid flow passages, and (bottom) isolated ponds. Blue arrows indicate flow velocity. | 12 |
| 1.6 | Nueces Delta. (top) Satelite image (image source: Hill et al. (2012)); (bottom) $1 \times 1\text{m}$ grid scale bathymetry. The color scale is of the bottom elevation (m) | 17 |
| 2.1 | Quadtree grid | 28 |
| 3.1 | Computation nodes at a grid in Frehd. Squares: computational node for the free-surface elevation (η) and depth (h); Circles: computational nodes for velocities (u, v) | 32 |
| 4.1 | Coarse-grid (i, j) and fine-grid (r, s) coordinate systems | 44 |
| 5.1 | Surface forces exerting on the net face flow areas of a resolved grid cell | 55 |

| | | |
|------|--|-----|
| 5.2 | (top) Flow continuity with the net fluxes at the faces of a grid cell (Q_x , Q_y) and a difference of the surface elevation $\Delta\eta$ over Δt . (bottom) Volume change (ΔV) scaled with the surface area A (left) and with the effective surface area A_{xy} (right). | 65 |
| 5.3 | Schematic diagram of a grid cell with resolved topography (top) and unresolved topography (bottom). The nomenclature, Q_x and Q_y denote x and y -directional fluxes on the faces of the cell (displayed with arrows); A_{xz} and A_{yz} denote the flow areas of the faces of the cell. | 67 |
| 5.4 | Computation nodes at a grid. Squares: free-surface elevation (η), depth (h), water volume (V), and surface flow area (A_{xy}); Circles: velocities (u, v), fluxes (Q), and face flow areas (A_{yz}, A_{xz}) | 71 |
| 6.1 | $1\times 1\text{m}$ grid scale bathymetry of the test section A. The color scale is of the bottom elevation (m). Bold lines indicate the boundaries of the test section. | 78 |
| 6.2 | $1\times 1\text{m}$ grid scale bathymetry of the test section B. The color scale is of the bottom elevation (m). Bold lines indicate the boundaries of the test section. | 79 |
| 6.3 | Boundary conditions for the numerical test. (top) Black lines: tidal boundaries, red arrows: inflow, and black dashed box: test section. (bottom) Black line: tidal boundary elevation, blue “X”s: time-steps of comparing projected flow variable, and black dashed lines: time-span of analyzing errors. | 81 |
| 6.4 | Absolute mean errors of the <i>MDB</i> experiment and control in the test section A | 91 |
| 6.5 | Willmott Skill Scores of the <i>MDB</i> experiment and control in the test section A | 92 |
| 6.6 | Absolute mean errors of the <i>MDB</i> experiment and control in the test section B | 93 |
| 6.7 | Willmott Skill Scores of the <i>MDB</i> experiment and control in the test section B | 94 |
| 6.8 | Spatial distribution of absolute mean errors in the test region A | 96 |
| 6.9 | Spatial distribution of absolute mean errors in the test region B | 97 |
| 6.10 | Spatial average free-surface elevation of the <i>MDB</i> experiment and control in the test section A | 100 |
| 6.11 | Spatial average free-surface elevation of the <i>MDB</i> experiment and control in the test section B | 101 |
| 6.12 | Fluxes projected in the test section A at $\eta_t = 0.32\text{ m}$ ($t = 14.1\text{ hours}$). The grey scale is of the bottom elevation (m). A blue arrow indicates a flux vector on the resolved coarse-grid cell (m^3/s). | 103 |

| | | |
|------|---|-----|
| 6.13 | Fluxes projected in the test section A at $\eta_t = 0.07$ m ($t = 15.2$ hours). The grey scale is of the bottom elevation (m). A blue arrow indicates a flux vector on the resolved coarse-grid cell (m^3/s). | 104 |
| 6.14 | Fluxes projected in the test section A at $\eta_t = 0.32$ m ($t = 16.4$ hours). The grey scale is of the bottom elevation (m). A blue arrow indicates a flux vector on the resolved coarse-grid cell (m^3/s). | 105 |
| 6.15 | Fluxes projected in the test section A at $\eta_t = 0.63$ m ($t = 17.6$ hours). The grey scale is of the bottom elevation (m). A blue arrow indicates a flux vector on the resolved coarse-grid cell (m^3/s). | 106 |
| 6.16 | Flow depths on the fine-grid scale projected in the test section A at $\eta_t = 0.32$ m ($t = 14.1$ hours). The color scale is of the depth (m) . . . | 108 |
| 6.17 | Flow depths on the fine-grid scale projected in the test section A at $\eta_t = 0.07$ m ($t = 15.2$ hours). The color scale is of the depth (m) . . . | 109 |
| 6.18 | Flow depths on the fine-grid scale projected in the test section A at $\eta_t = 0.32$ m ($t = 16.4$ hours). The color scale is of the depth (m) . . . | 110 |
| 6.19 | Flow depths on the fine-grid scale projected in the test section A at $\eta_t = 0.63$ m ($t = 17.6$ hours). The color scale is of the depth (m) . . . | 111 |
| 6.20 | Flow depths on the fine-grid scale projected in the test section B at $\eta_t = 0.32$ m ($t = 14.1$ hours). The color scale is of the depth (m) . . . | 112 |
| 6.21 | Flow depths on the fine-grid scale projected in the test section B at $\eta_t = 0.07$ m ($t = 15.2$ hours). The color scale is of the depth (m) . . . | 113 |
| 6.22 | Flow depths on the fine-grid scale projected in the test section B at $\eta_t = 0.32$ m ($t = 16.4$ hours). The color scale is of the depth (m) . . . | 114 |
| 6.23 | Flow depths on the fine-grid scale projected in the test section B at $\eta_t = 0.63$ m ($t = 17.6$ hours). The color scale is of the depth (m) . . . | 115 |
| 6.24 | x -directional drag coefficients applied to the <i>MDB</i> experiment in the test section <i>A</i> . The grey scale is the scale of the drag coefficient. . . . | 117 |
| 6.25 | y -directional drag coefficients applied to the <i>MDB</i> experiment in the test section <i>A</i> . The grey scale is the scale of the drag coefficient. . . . | 118 |
| 6.26 | x -directional drag coefficients applied to the <i>MDB</i> experiment in the test section <i>B</i> . The grey scale is the scale of the drag coefficient. . . . | 119 |
| 6.27 | y -directional drag coefficients applied to <i>MDB</i> experiment in the test section <i>B</i> . The grey scale is the scale of the drag coefficient. | 120 |
| 6.28 | Absolute mean errors of the <i>M</i> experiment and control in the test section <i>A</i> | 123 |
| 6.29 | Comparison of projected fluxes between the <i>MB</i> and <i>M</i> experiments in the test section A at $\eta_t = 0.32$ m ($t = 14.1$ hours). The grey scale is of the bottom elevation (m). A blue arrow indicates a flux vector on the resolved coarse-grid cell (m^3/s). | 125 |

| | | |
|------|---|-----|
| 6.30 | Comparison of projected fluxes between the <i>MB</i> and <i>M</i> experiments in the test section B at $\eta_t = 0.07$ m ($t = 15.2$ hours). The grey scale is of the bottom elevation (m). A blue arrow indicates a flux vector on the resolved coarse-grid cell (m^3/s). | 126 |
| 6.31 | Absolute mean errors of the <i>M</i> and <i>MB</i> experiments in the test section A | 127 |
| 6.32 | Comparison of projected fluxes between the <i>MD</i> and <i>M</i> experiments in the test section A at $\eta_t = 0.63$ m ($t = 17.6$ hours). The grey scale is of the bottom elevation (m). A blue arrow indicates a flux vector on the resolved coarse-grid cell (m^3/s). | 129 |
| 6.33 | Spatial average free-surface elevation of the <i>M</i> , <i>MB</i> , <i>MD</i> experiments, control, and reference in the test section A | 130 |
| 6.34 | Average grid cell surface area with a change of $\Delta\eta$ in the test section A | 133 |

Chapter 1

Introduction

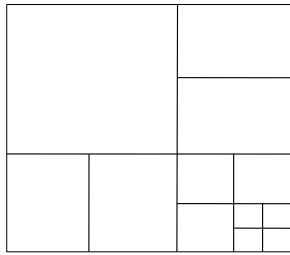
1.1 Unresolved topography and subgrid methods

It is well understood that numerical models for real-world shallow water flows are sensitive to the model grid scale, i.e., the relationship between the resolved model grid and unresolved subgrid features (Yu and Lane, 2006a; Horritt and Bates, 2001). The grid scale controls both the resolved flow scale and the submerged topography that can be directly represented in the discrete governing equations (Nicholas and Mitchell, 2003). Until recently, practical grid scales for shallow-water hydrodynamic models were often finer than, or similar to the surveyed topographic data (Blöschl and Grayson, 2001). For such conditions the grid-scale bottom topography can be reasonably approximated by simple interpolation from survey data and the unknown subgrid features can be represented by a friction parameter, which usually is obtained from literature estimates or calibration. The resulting model fidelity is constrained by survey data rather than model physics and numerical methods (McMillan and Brasington, 2007). However, with the recent developments in topographic survey technologies (e.g., aerial photometry, remote sensing, hyper-spectral image processing, etc.), it is possible to obtain topographic detail that is far finer than the practical discretization grid scales (Dottori et al., 2013). Therefore, we are faced with an open question of how to effectively use such detailed topographic information (hereinafter,

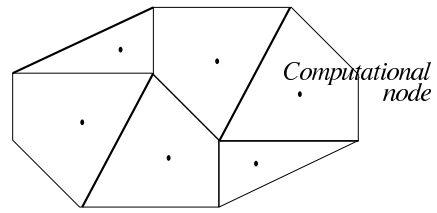
denoted as “subgrid topography”) for the greatest fidelity without actually resolving the finest known details.

A fine grid allows a numerical hydrodynamic model to capture flow effects of minor topographic features, but can dramatically increase computational cost (Özgen et al., 2015). For example, a two-dimensional (2D) model with a 1×1 m grid will require 100 times more grid cells than a model with a 10×10 m grid, and will require a time step that is $1/10^{th}$ the size, so the overall computational cost increases by 1,000 for a linear change from 10 m to 1 m resolution. Although massively parallel supercomputers with direct computation of hydrodynamics at fine scales is possible (e.g., Aizinger et al., 2013; Lambrechts et al., 2008), such computational capabilities are not readily accessible to many engineers and scientists who need to use hydrodynamic models for real-world solutions. Furthermore, engineering analyses of “what if” cases typically use multiple model runs with a variety of environmental forcings, which might require more supercomputing CPU time than is cost effective. Thus, despite advances in supercomputing, there is a need for efficient hydrodynamic modeling at grid scales that are coarser than the known topographical features.

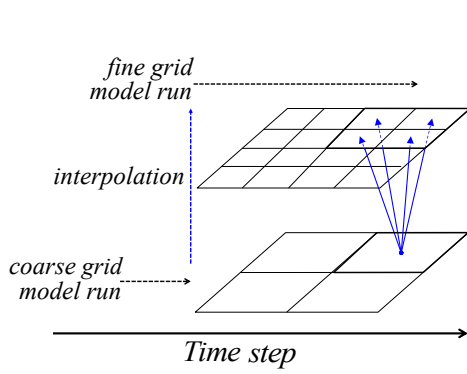
Various grid schemes have been developed in a form of (i) adaptive grids (e.g., Liang and Borthwick, 2009), (ii) unstructured grids (e.g., Sehili et al., 2014; Begnudelli and Sanders, 2007), (iii) multi-scale grid modeling such as hierarchical grid refinement (Platzek et al., 2015), and (iv) cut-cell approach (e.g., Rosatti et al., 2005) (see Figure 1.1). Such schemes use refined grids locally in time-space domain for representing the effects of small topographic features. Resolving fine-scale features with the schemes outlined in Figure 1.1 typically increases computational complexity



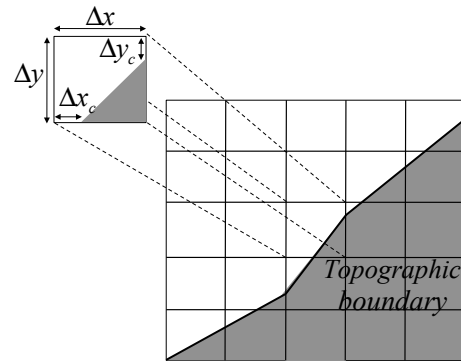
Adaptive grid



Unstructured grid



Multi-scale grid modeling



Cut-cell approach

Figure 1.1: Locally refined grid schemes in time-space domain

of grid generation and/or solution algorithms. In contrast, a structured grid scheme is easy to implement and typically has computationally-efficient solutions, but requires the same grid resolution throughout the model grid (Platzek et al., 2015). Numerical schemes addressing this disagreement between topographic data resolution and model grid resolution (hereinafter, denoted as a “subgrid method”) have been of interest for their potential computational efficiency (Casulli, 2009; Yu and Lane, 2006a; Defina, 2000). A subgrid method generally parameterizes the effects of topographic details into the governing equations (Platzek et al., 2015; Dottori et al., 2013). A goal for any subgrid method is to accurately reproduce the resolved-scale flow processes influenced by subgrid features at lower computational costs than a fine-scale resolved model.

Subgrid topographic structures can deflect, force, or impede flow (Chen et al., 2012; Yu and Lane, 2006a), and affect the local storage volume for a given surface elevation (Dottori and Todini, 2013; Yu and Lane, 2006a). Subgrid spatial heterogeneity in emergent/submerged topography creates a geometry problem because the net inflow volume into a resolved grid cell and the elevation change are no longer related by the simple resolved grid geometry (Defina, 2000). That is, a net inflow volume (dV) into a resolved grid cell of discrete surface area $A = \Delta x \Delta y$ without emergent subgrid topography will result in an elevation change of $d\eta = dVA^{-1}$. However, emergent subgrid topography creates a relationship between the wet surface area and dry surface area as a function of elevation (η), such that a relationship of the form $d\eta = \alpha(\eta)VA^{-1}$ is required, where $\alpha(\eta)$ is a function representing the effects of the emergent subgrid topography that can vary nonlinearly with η . Further-

more, at the face between two resolved grid cells, any subgrid topography (emergent or submerged) affects the flow area between the cells and hence the relationship between velocity and flux. The resulting discrepancies between the resolved-scale and fine-scale water volumes and fluxes will, in turn, cause errors in critical wetting and drying processes such as flow rate, time-space coverage of inundation, and flow path (Yu and Lane, 2006a).

The effects of emergent topography can be examined through a conceptual model relating η , the mean bottom elevation (Z_b) and a range of subgrid bottom elevations (z_b). With a change of the surface elevation ($d\eta$), we can consider three possible conditions illustrated in Figure 1.2: (i) the upper panels illustrate the fully-flooded condition when $\eta > \max(z_b)$ and $\eta > Z_b$, (ii) the middle panels illustrate the emergent topography condition when $\eta < \max(z_b)$ and $\eta > Z_b$, and (iii) the lower panels show the unresolved volume condition when $\eta < Z_b$ and $\eta > \min(z_b)$.

In conventional Cartesian-grid models such as ELCOM (Hodges et al., 2000) or TRIM (Casulli and Cheng, 1992), the volume change at a discrete cell (dV) is determined with $dV = A dh$, where A is the cell surface area and h is the depth, defined as $h = \eta - Z_b$. For our conceptual model, in condition (i) the dV is unchanged from the conventional Cartesian-grid approach, but for conditions (ii) and (iii) requires $A = f(h)$ or $A = f(\eta)$, which introduces an additional nonlinearity into the governing equations. Furthermore, for sufficiently complex topography the water storage volume below the fully flooded condition will depend upon the grid scale, as illustrated in Figure 1.3.

Neglect of subgrid topographic variability can cause unresolved local forcing

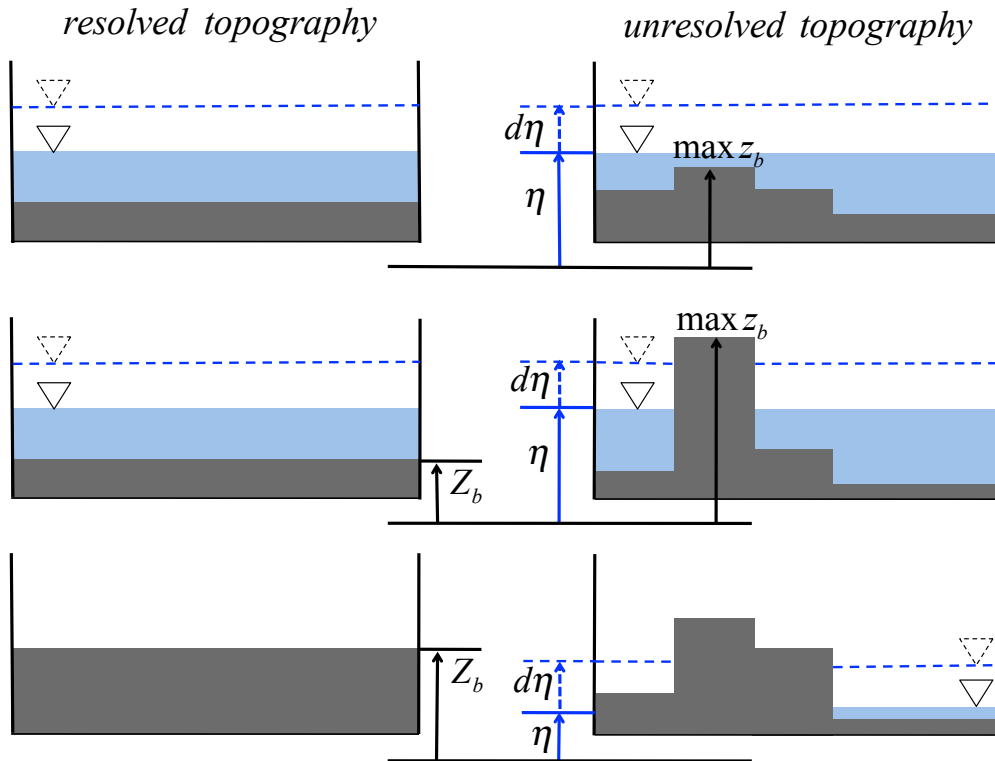


Figure 1.2: A representative cross-section of a grid cell with resolved topography (left) and unresolved topography (right). The nomenclature, $d\eta$ denotes a change of the free-surface elevation (η), Z_b and $\max z_b$ denote the resolved-grid bottom elevation and the highest subgrid elevation, respectively.

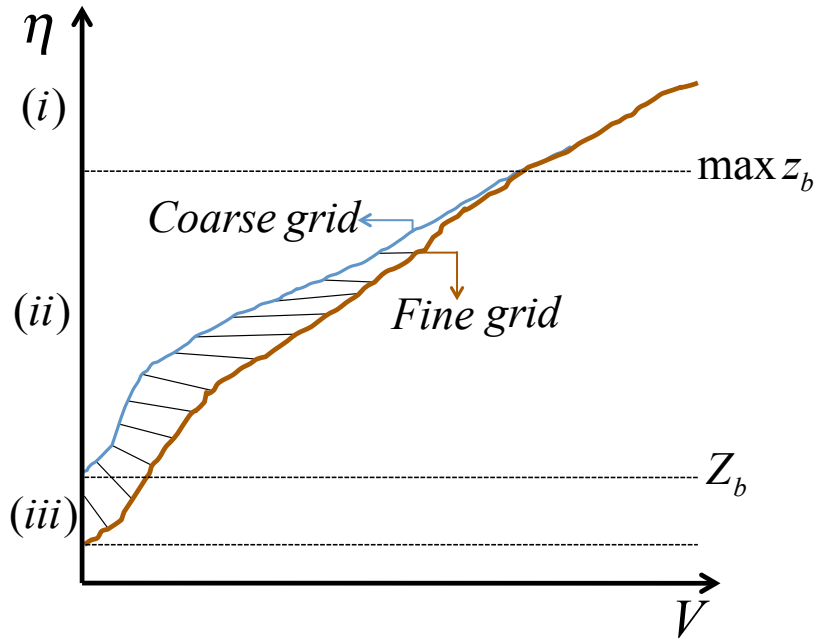


Figure 1.3: Storage volume (V) of fine grid bathymetry and coarse grid bathymetry in relation with a change of the surface elevation (η). The nomenclature, Z_b and $\max z_b$ denote the resolved grid bottom elevation and the highest subgrid elevation, respectively.

and under/overestimation of friction (Volp et al., 2013; Yu and Lane, 2006a). The bottom friction in a momentum equation typically is a functional form of $C_D u^2$, where C_D is an empirical drag coefficient or any friction parameter and u^2 is the square of the flow velocity. The upper panel of Figure 1.4 shows an extension of our conceptual model to consider velocity/drag effects associated with variability associated with subgrid obstructions; specifically, the local velocity variability (i.e., $u_i: i \in \{1 : N\}$, with N denoting the number of discrete subgrid units) and a locally-varying drag coefficient (i.e., $C_{Di}: i \in \{1 : N\}$) that might represent different forms of submerged vegetation. The bottom friction at a resolved grid cell is $C_{Dc} \bar{u}^2$ with the resolved flow velocity \bar{u} and drag coefficient C_{Dc} . We expect that $C_{Dc} \bar{u}^2 = \sum_i (C_{Di} u_i^2) / N$ only under conditions where the C_{Dc} is carefully tuned. There is no reason to expect that such a tuning should be independent of \bar{u} .

Finally, our conceptual model needs to consider cross-sectional area effects for shear terms in the momentum equation that are affected by emergent topography, as illustrated in the lower panel of Figure 1.4. Surface forces (F) between the fluid in two resolved grid cells are functions of the turbulent shear stress τ and the cell face flow area A_f , such that $F = \tau A_f$. The flow area A_f in the resolved grid geometry is simply $A_f = h \Delta x$ or $h \Delta y$ compared to a more complicated nonlinear function of h implied in the sketch for emergent subgrid topography.

Some previous subgrid methods represented the effects of unresolved topography with a porosity parameter (e.g., Cea and Vázquez-Cendón, 2010; Guinot and Spares-Frazão, 2006). Others used an averaging approach for the “wet-dry” phase-modified governing equations over a computation unit (e.g., Defina, 2000). These

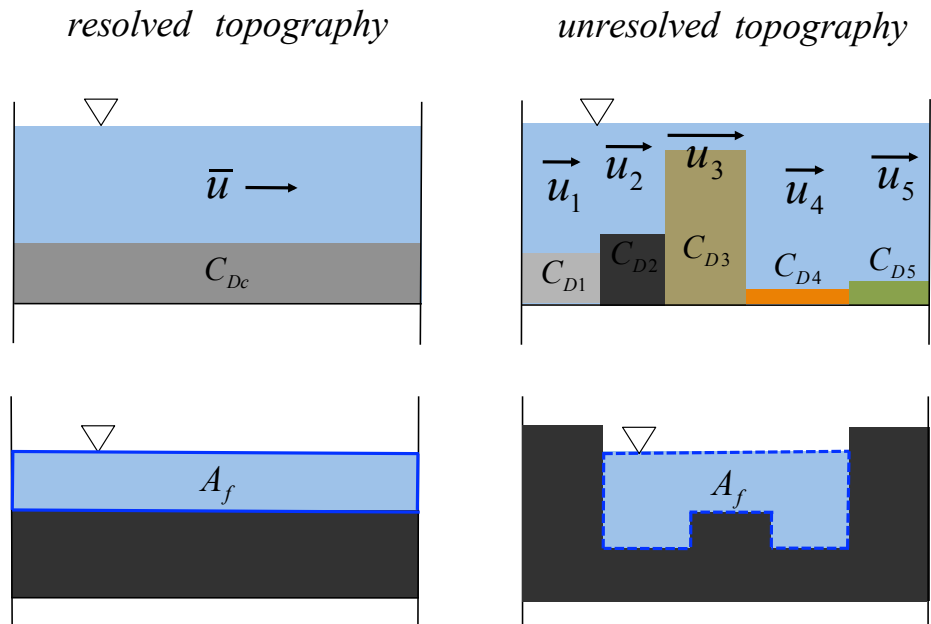


Figure 1.4: A representative cross-section of a grid cell with resolved topography (left) and unresolved topography (right). The nomenclature, \bar{u} and C_{Dc} denote the velocity and drag coefficient of the resolved grid cell; u_i and C_{Di} denote the local velocity and local drag coefficient at the location i ($i \in \{1, 2, \dots, 5\}$); and A_f denotes a representative flow area of the grid cell.

can be considered forms of “subgrid geometric parameterization” as they rely only on the geometry and for parameterization and do not consider dynamic flow effects. The approach of Defina (2000) addressed the geometry problem corresponding to a change of the free-surface elevation ($d\eta$) that provides nonlinearity associated with emergent/submerged topography (Figs. 1.2~1.3, as discussed above).

An approach introduced by Casulli (2009) used integrated fluxes in/out of a grid cell over subgrid topography linked to $d\eta$ in a volume-conserving scheme. Two key drawbacks have been previously noted with the Casulli (2009) approach: (i) the inability to represent unresolved flow connectivity or blockage on subgrid scale as illustrated in Figure 1.5, and (ii) the friction slope requirement within a model-resolved grid cell (Platzek et al., 2015; Volp et al., 2013; Stelling, 2012). The friction slope requirement across a model-resolved grid cell can cause a misrepresentation of energy loss by subgrid obstructions causing backwater (e.g., embankments), steering effects (e.g., narrow channels), or spatially-varying shear.

Despite its importance in shallow water dynamics (Yu and Lane, 2006b), the issue of subgrid bottom friction has not been addressed with the type of numerical experimentation previously applied to the issues of subgrid storage volume and subgrid-face flow area that were discussed above. Friction parameters have often been defined as a single value applied to the bulk flow that is set using either empirical data (Lane, 2005) or calibration (Wang et al., 2012). Some recent studies have included a dynamic friction model that depends on flow depth to incorporate nonlinear effects of subgrid topography (hereinafter, “subgrid friction parameterization”). A common approach in prior subgrid friction models is use of a local roughness height

derived from a representative (i.e., model-resolved) water depth and the mixing layer theory (e.g., [Casas et al., 2010](#)). A recent new avenue in the subgrid friction parameterization is the quadtree approach of [Volp et al. \(2013\)](#), which uses four subgrid momentum domains within a resolved grid cell. The integrated effect of local friction is distributed over a sub-domain (a quarter of a grid cell) with known subgrid topography, sub-domain volume, and resolved grid face velocities. The friction model of [Volp et al. \(2013\)](#) has an effect of considering variability of friction across each sub-domain, but variability is constrained to the four sub-domains.

To date, there are no subgrid models that comprehensively represent unresolved flow connectivity or blockages created by subgrid topographic features. Here a “feature” can be considered a coherent set of subgrid elevations forming obstructions, channels, or depressions that might steer or block the flow. For example, as illustrated in [Figure 1.5](#) there can be subgrid-scale passages whose bottom elevations (z_b) are lower than the resolved-scale bottom elevation ($z_b \leq Z_b$). Physically, flow is possible along contiguous subgrid channels, but cannot occur at the resolved grid scale when the resolved grid cell is “dry” (i.e., $\eta \leq Z_b$). Representing the effects of these features at the resolved flow scales is a challenge as their effects are due to the coherent relationships forming the feature rather than the statistical variability of the topography. One partially-effective approach addressing the effect of subgrid blockage in prior studies is sampling a representative subgrid topographic elevation of embankments, and assigning it as the resolved grid cell geometry (e.g., [Platzek et al., 2015](#)). In another approach, narrow embankments that are as long as (or longer than) a single resolved grid cell have been shown to be effectively represented

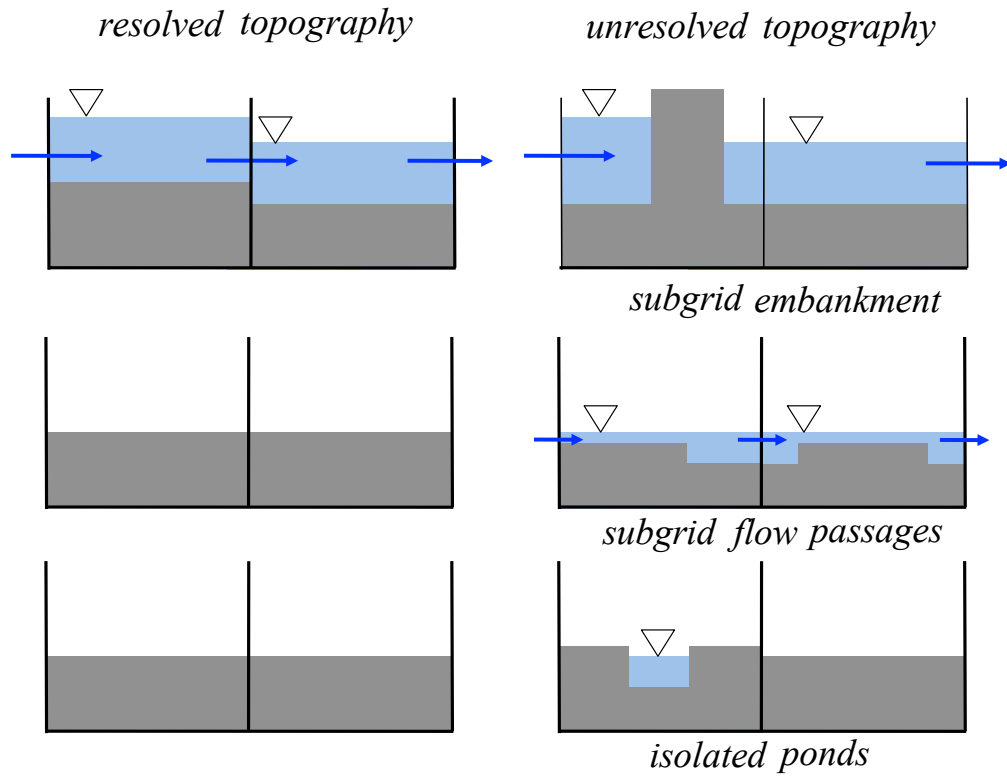


Figure 1.5: A cross-section of two neighboring grid cells with resolved topography (left) and unresolved topography (right). Unresolved subgrid topographic features: (top) subgrid embankments, (middle) subgrid flow passages, and (bottom) isolated ponds. Blue arrows indicate flow velocity.

as edges in a hydrodynamic model (Hodges, 2015). For subgrid storage, Jiang and Wai (2005) constructed a network of capillaries connecting resolved-scale “dry” grid cells to representing subgrid water storage. Another approach by Li (2015) prioritized connectivity over blockage, which was accomplished by using the minimum subgrid topographic elevation for a resolved grid scale elevation.

The present work builds on the prior studies (which are discussed more thoroughly in Chapter 2) by developing a subgrid model addressing the effect of frictional forcing on the subgrid scale in shallow water dynamics. Two different schemes are proposed to account for flow friction caused by emergent unresolved topography, building on the ideas of Casulli (2009) and Volp et al. (2013). The first scheme is a subgrid drag model (Chapter 4) derived by upscaling subgrid wetted areas into the resolved grid equation so that directional drag coefficients can represent the integrated effects of drag in the different coordinate directions. The advantage of this approach is that the major change to a 2D shallow water solution method is the addition of different drag coefficients on the x and y faces of the grid cells. The second scheme (Chapter 5) is a subgrid momentum model that is derived from subgrid forces and the integrated fluxes in/out the faces of a grid cell. This approach has the effect of considering the subgrid topography at the interface between two resolved grid cells in momentum conservation. The present work additionally applies a subgrid topography sampling method (Section 5.4) to address the effect of subgrid flow passages that are below a resolved grid cell bottom elevation; this work builds on the idea of (Li, 2015).

One of the complexities introduced by dynamic subgrid modeling (i.e., con-

sidering the time-varying geometry of emergent topography) in the present work is the need for nonlinear functions relating the water surface elevation (η) to geometric values (e.g., surface area, flow cross-section). To reduce computational costs, we apply a look-up table that stores subgrid geometric quantities at pre-defined intervals of $\Delta\eta$ for each grid cell. The approach taken herein is a modification of an algorithm proposed by [Li \(2015\)](#) (Appendix D).

Coupling the new subgrid drag model with the new subgrid momentum model and using an improved subgrid topography sampling approach is shown to provide good representation of subgrid topographic effects (Chapter 6). To verify the different model performances and constraints, the subgrid drag model and the subgrid momentum model are tested and compared both separately (Chapters 4, 5) and in a coupled approach (Chapter 6). The numerical tests validate the performance by comparing the coarse-grid solution using the subgrid models with the fine-grid solution for the same region.

The performance of any subgrid method will depend on the scale ratio between resolved and unresolved topographic features, the separation and distribution of unresolved features, as well as the parameterizations and limitations of the subgrid model itself. Ideally, a subgrid model in a dynamic simulation should capture exactly the correct net flows in/out of the resolved grid cell and a resolved water elevation that reflects the median local elevation obtained by an equivalent fine-grid model. However, it is unlikely that any subgrid model will achieve such performance, so there is a practical interest in evaluating unavoidable model errors in relation with multiple topographic features of the test terrain. Herein are new proposed indicators

that can be used for evaluating the performance and limitations of a subgrid model as simple and quantitative measures, which provide insight for a subgrid model selection depending on topography of a test region. Chapter 6 provides a description of new indicators and examines the use of the indicators in evaluating the performance of the new subgrid models.

The focus of the present research is on the subgrid methods needed for modeling tidal marshes where small channels, pools, and irregular embankments are combined with wetting/drying of the landscape. Such flows are mostly subcritical (Froude number less than unity), with supercritical regions typically being local and unresolvable at practical grid resolutions. Although tidal marshes can be the estuarine interface between fresh and salt water, the depths are typically shallow (often less than 1 m) and are readily mixed by the wind so vertical stratification typically does not affect the flow dynamics (Ji, 2008). It follows that modeling is reasonably approximated with the 2D depth-averaged hydrostatic Navier-Stokes equations (commonly known as the shallow water equations) (Dias et al., 2013; Knock and Ryrie, 1994).

Herein, the Fine Resolution Environmental Hydrodynamics Model (Frehd) has been modified to include new subgrid algorithms. Frehd is a numerical model written in Matlab by Prof. B.R. Hodges as a research tool for developing and testing new numerical schemes. Although Frehd is written with capabilities for full 3D, non-hydrostatic, and density stratification behavior, herein only the 2D, hydrostatic, uniform density attributes are applied. Frehd is an implementation of the semi-implicit, volume-conserving TRIM scheme originated by Casulli and Cheng (1992),

which was also adopted and modified in the ELCOM code (Hodges et al., 2000) and subsequent works of Casulli and Zanolli (2002); Casulli (1999) and Casulli and Cattani (1994). The new subgrid models are tested for simple theoretical domains and with 1×1 m high-resolution topography from marshes of the Nueces River Delta along the Texas (USA) coast of the Gulf of Mexico. This work follows on previous coarse-grid implementations of Frehd on this system (Ryan and Hodges, 2011). Chapter 3 provides a methodology of Frehd and its free-surface solution without a subgrid scheme which becomes a baseline for the verification test of the new subgrid models.

Tidal marshes such as the Nueces River Delta can be considered one of the most challenging topographies for hydrodynamic modeling due to the heterogeneous distribution of emergent and submerged topography over a range of scales, with feature as small as 3 to 4 m readily visible in 1×1 m lidar data (Figure 1.6). From recent experience, practical grid resolutions for engineering studies on such a system might range from 10×10 m to 30×30 m, depending on available computational resources. For example, in the Nueces River Delta study of Ryan and Hodges (2011), a 15×15 m grid was used in a computational domain of more than 600,000 grid cells with a model time step of 180 seconds. The computations were typically accomplished at 7 times real time on a desktop workstation with a 3 GHz Intel processor and 8 GB of memory. In contrast, a 1×1 m grid requires almost 150 million grid cells and a time step near 1 second, which presently cannot be handled without resorting to supercomputing. Appendix A provides an overview of the Nueces Delta region and the restoration efforts for the Delta.

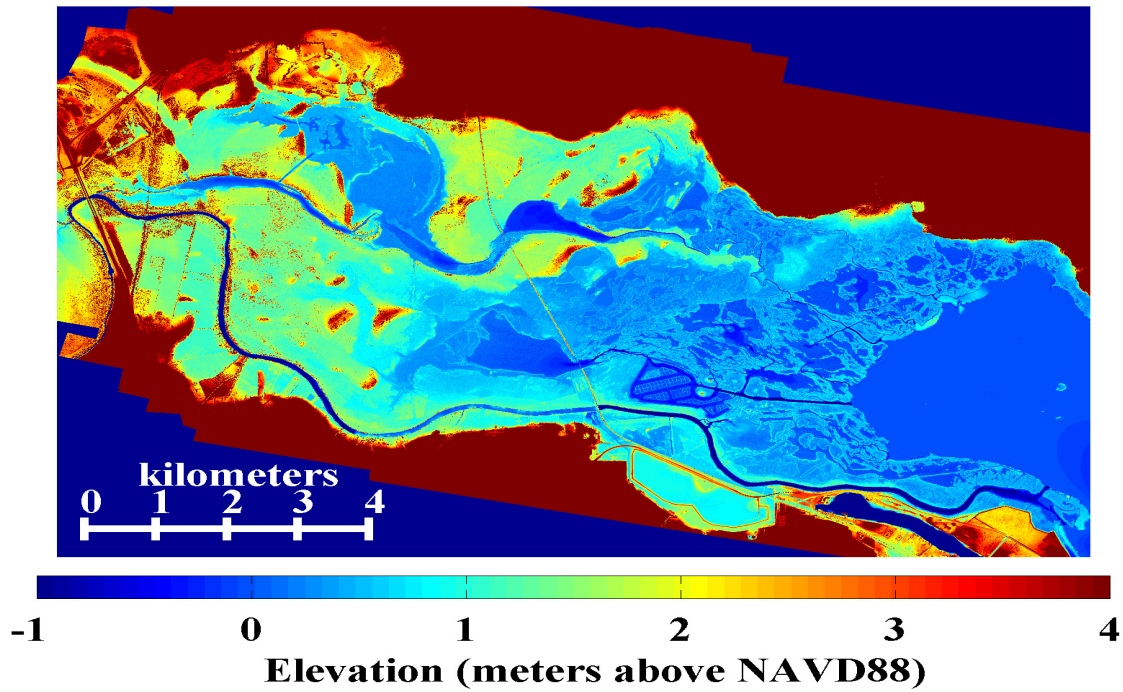
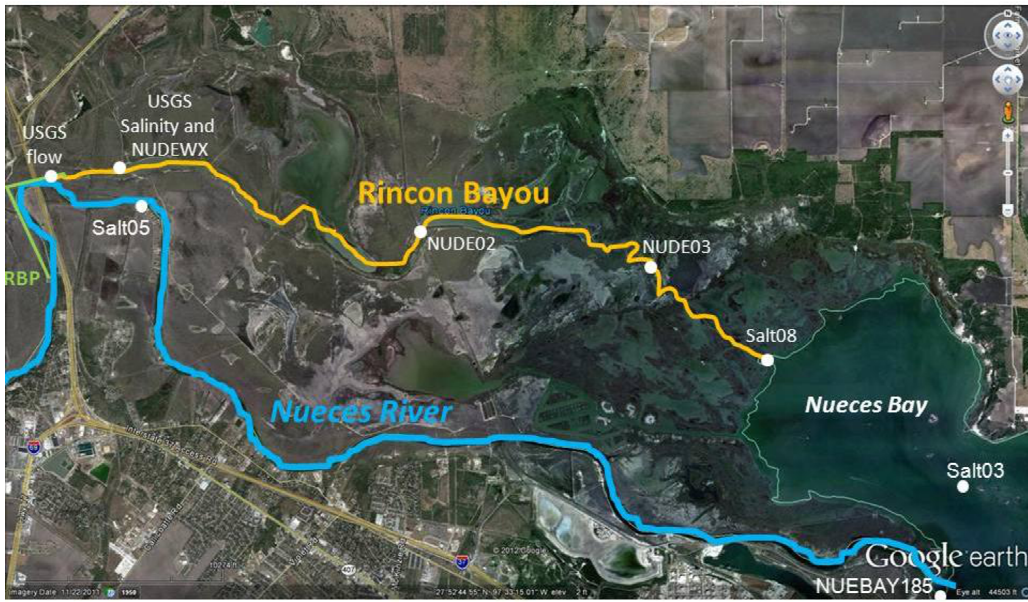


Figure 1.6: Nueces Delta. (top) Satellite image (image source: [Hill et al. \(2012\)](#)); (bottom) 1×1m grid scale bathymetry. The color scale is of the bottom elevation (m)

1.2 Research objectives and approach

The objectives of this research are:

1. Parameterize frictional resistance of subgrid topography based upon the relationships between the grid scale and the unresolved topography to create a *subgrid drag model* (Chapter 4).
2. Develop a *subgrid momentum model* that includes subgrid topographic effects on both mass and momentum conservation on cell faces (Chapter 5).
3. Evaluate the effectiveness of coupling the subgrid drag model, subgrid momentum model, and the subgrid topography sampling method as a *combined subgrid model* (Chapter 6).
4. Evaluate the performance of a look-up table method to reduce the computational cost of the new combined subgrid model (Chapter 6).
5. Devise new indicators for evaluating a subgrid model behavior across diverse topography (Chapter 6).

This study parameterizes the effects exerted by topographic features from local flow scale to the resolved flow scale. The first objective was achieved by deriving an analytical relationship between grid-scale and unresolved topography that provides upscaling of the distributed drag coefficients (at the subgrid scale) to an effective drag coefficient at the resolved grid scale. This approach creates a resolved scale drag coefficient is a function of the estimated distribution of subgrid water

depths as well as the distribution of emergent topography and distributed roughness. The resolved scale drag coefficient changes dynamically with the local flow conditions. The resulting subgrid drag model parameterizes the horizontal spatial distribution of subgrid topography. This approach is tested in the Frehd code, but can be readily adapted to other models as it simply requires a dynamic approach to computing the drag coefficient from subgrid data.

The second objective was achieved by deriving an extension of the mass conservative subgrid method of [Casulli \(2009\)](#) to include conservation of momentum with subgrid geometric effects across resolved grid faces on surface shear forces. In contrast to the subgrid drag model (above) that considers the effects of the horizontal distribution of subgrid topography *across* a grid cell, the subgrid momentum model developed to meet the second objective uses the subgrid topography *at the interface* between two resolved grid cells to parameterize the conservation of mass and momentum. The subgrid momentum model was implemented in the Frehd code and required significant revision of the fundamental numerical discretization. Although the method is adaptable to other hydrodynamic codes, it must be derived specifically to apply to the discretization method of the code.

The third objective was achieved by defining metrics for quantitative comparison of numerical simulations at fine-grid scale and coarse-grid scale, which allows analysis of subgrid model performance. The subgrid drag model, the subgrid momentum model, and the combined model were tested separately and compared using models simulations of sections from the 1×1 m topography of the Nueces River Delta (Texas, USA).

The fourth objective was achieved by adding the linear interpolation function to the prior look-up table algorithm of Li (2015). A linear interpolation provides an approximation of subgrid geometric values at a linear range of the water surface elevation with low computational cost. The effectiveness of the look-up table method was evaluated through the numerical simulations.

The fifth objective was achieved by devising new indicators for integrated effects of subgrid topographic feature over the test domain. Use of the indicators for evaluating the performance of a subgrid model was examined with the numerical test results of the new subgrid models in the current work.

1.3 Contributions to science and technology

This research specifically contributes new advances in science and technology by:

1. Deriving the new numerical scheme to analytically include the effects of heterogeneous subgrid topography and distributed roughness directly on the resolved scale drag coefficient in a manner that can be readily adapted to other models.
2. Deriving the new numerical scheme that includes subgrid topographic effects on surface shear forces in momentum conservation at the interface between grid cells,
3. Developing the new model that is coupled with the consideration of subgrid varied forcing on local flow scale, the geometric consideration of mass and

momentum at the boundaries of grid cells, and subgrid flow connectivity below the resolved grid-cell bottom elevation,

4. Providing insight for developing the look-up table method in order to improve computational cost efficiency of a subgrid model,
5. Proposing new indicators that can be used for evaluating the performance of a subgrid model in relation with topography of a test terrain.

The overall contribution of this research is in the creation of new numerical approaches for computationally-efficient models of the shallow flow over complex terrain at practical grid scales. As high-resolution lidar and 3D bathymetric data become more commonly available, practicing engineers will be faced with the challenge of how to quantitatively incorporate the high-resolution data into lower-resolution engineering hydrodynamic models. The methods developed herein are an answer to this challenge.

1.4 Dissertation outline

This dissertation consists of seven chapters. Chapter 2 provides a review about the key findings of prior subgrid model studies. Chapter 3 provides the methodology of the baseline hydrodynamic model without a subgrid scheme (Frehd). The new subgrid drag model is derived in Chapter 4. Chapter 5 describes a derivation of the new subgrid momentum model and the subgrid topography sampling method for reflecting the effect of flow connectivity at the surface elevation below the model-resolved grid bottom elevation. Validation and verification of the new

subgrid models, and development of new indicators as measures for evaluation of a subgrid model performance are provided in Chapter 6. Lastly, Chapter 7 summarizes the key findings and limitations of this research with associated recommendations for future work.

Chapter 2

Subgrid Methods

2.1 Prior work in subgrid geometric parameterization

Defina (2000) introduced an approach integrating the “wet-dry” phase-modified governing equations over depth and averaging it over a computational unit area in order to deal with the geometry problem (i.e., the partially wet area) created by unresolved topography. The wet-dry phase function (Ψ) in Defina (2000) represents local wet or dry conditions, which are defined as:

$$z_b(x) \leq \eta \rightarrow \Psi(x) = 1$$

$$z_b(x) > \eta \rightarrow \Psi(x) = 0$$

where x is the vector of the spatial coordinates at the subgrid scale, and z_b denotes subgrid topographic elevation. This approach provides a resolved-scale $0 \geq \Psi \geq 1$ that represents the effective fractional area that is wet for each resolved grid cell.

Other studies used the idea of a porosity parameter with both isotropy (e.g., Cea and Vázquez-Cendón, 2010; Guinot and Spares-Frazão, 2006) and anisotropy (e.g., Chen et al., 2012; Schubert and Sanders, 2012) to capture the volume-elevation relationship with emergent topography. The porosity type parameter was *a priori* specified for a bulk water mass in the early works, but in recent studies has a time-

space variability, being computed directly from subgrid bathymetry at each time-step as a function of the water level.

An approach presented by [Casulli \(2009\)](#) used a volume-conserving scheme for addressing the nonlinearity of wet-dry interfaces and ensuring a strict flow continuity. This scheme discretizes a solution for η at the center of a grid cell representing the average derivative over a grid cell with the velocities at the midpoint on the faces of each grid cell. [Casulli \(2009\)](#) constructed the flow continuity with the integrated fluxes (Q) in/out of a grid cell on the faces of a grid cell.

$$\frac{\Delta V}{\Delta t} + \int_f dQ^{n+1/2} = 0 \quad (2.1)$$

where V denotes the volume of a grid cell, \int_f denotes an integral of the fluxes on the faces (f) of a grid cell, and the time index $n + 1/2$ indicates the net flux between the n and $n + 1$ time step. The flow continuity for the integrated net fluxes on the faces of a grid cell modifies the discrete free-surface solution to ensure conservative relationships between the volume flux, the resolved velocity at the grid cell face, and the total subgrid area at the face. This approach has an effect of adding a friction slope between the faces of a grid cell. [Appendix B](#) provides the first-order upwind discretized solution applying the flow continuity model of [Casulli \(2009\)](#), which is coded in `Frehd` for the verification test of the new subgrid models in [Chapter 6](#). [Chapter 3](#) provides further description of the volume-conserving scheme, which is adapted and improved within the present work.

2.2 Prior work in subgrid friction parameterization

A key drawback of the subgrid geometric parameterizations discussed in Section 2.1 is their use of a single friction slope across the entire resolved grid cell to characterize energy losses (Platzek et al., 2015; Volp et al., 2013). This assumption is questionable for subgrid topography that includes obstructions causing backwater (e.g., embankments), steering effects (e.g., narrow channels), or spatially-varying shear. By misrepresenting the linkage between energy loss, velocity magnitude, and cross-sectional flow area, the subgrid geometry schemes described above can either overestimate or underestimate energy losses. As a result, modeled velocities and fluxes can be larger than physically plausible or smaller than reasonable for the forcing (Sehili et al., 2014; Volp et al., 2013).

With a highly irregular terrain or shallow flow, neglected local forcing can make a model unreliable (Cea and Vázquez-Cendón, 2010; D’Alpaos and Defina, 2007). Effectively estimating the resolved-scale effects of the heterogeneous subgrid energy loss appears to be a key issue in addressing the issues of subgrid spatial variation (Volp et al., 2013; Casas et al., 2010). Drag exerted by rigid topographic structures or vegetation was reported to be likely dominant over bottom shear in a free-surface flow (Cea and Vázquez-Cendón, 2010; Huthoff et al., 2007). This problem can arguably be addressed with subgrid friction parameterization.

Employing a friction or roughness parameter is a recognized way to account for energy loss due to unresolved topography and roughness in a numerical model (Smith and Liang, 2013; Lane, 2005). With the ease of integrating a friction parameter into existing models (McMillan and Brasington, 2007), it is widely used for

incorporating the unresolved forcings (e.g., turbulence, depth-integrated flow scales, numerical dissipation, etc.) (Morvan et al., 2008). A drag coefficient (C_D) is typically used to represent the relationship between the drag force developed by a boundary layer and the velocity of the free stream flow. Drag can be conceptually divided into surface drag (the effect of surface roughness smaller than the viscous boundary layer thickness) and form drag (the blocking and wake effects from larger objects). For simple flows the relationship between C_D and free-stream velocity can be obtained through experiment applied with scaling arguments (White, 2006). However, with complex topography it is difficult to clearly identify the free-stream velocity at any particular location, and the contributions from surface and form drag can be so intermingled as to be indistinguishable.

In a hydrodynamic model, the flows and geometry at the resolved grid scale are typically assumed to provide reasonable approximations of the free-stream velocity so that C_D (or some other friction parameter) implicitly incorporates both the surface and form drag effects of roughness and obstructions (Chisolm, 2011; Huthoff et al., 2007). The model friction parameter, or a heterogeneous spatial distribution of a friction parameter, is typically determined *a priori* through either (i) model calibration with observed data from the system (Hughes et al., 2011) or (ii) using land-cover classification for the topography and friction parameters previously reported in the literature (Abu-Aly et al., 2014; Hossain et al., 2009).

Neither approach is entirely satisfactory for topographically-complex flows such as tidal marshes. Calibration from observations would seem to be preferred, but observations are typically too coarse in either time and spatial distribution to

provide confidence that a calibration results in the correct fluxes at non-observed locations. Use of literature values for friction is also problematic as they do not consider the scale effects between the resolved grid and the subgrid features. That is, the friction parameter that is appropriate for a 30×30 m grid cell might not be the same value as that for a 10×10 m grid cell as the relationships between the resolved velocity, the subgrid geometry, and the frictional losses can be different. Further compounding this problem is that the model grid scale is closely linked to the development of numerical dissipation, which depends on the numerical scheme (Morvan et al., 2008; Horritt, 2005). For coarse-grid models with low-order numerical schemes the numerical dissipation can be larger than the physical dissipation represented by the friction parameter, which renders the latter irrelevant. While Schubert and Sanders (2012) and Lane et al. (2004) argued that a friction parameter is less important to a model solution than grid scale, a number of studies stressed its influence on model accuracy (e.g., Abu-Aly et al., 2014; Casas et al., 2010).

An advance over the traditional *a priori* constant friction parameters is the use of time-varying (dynamic) frictional parameters based on local roughness heights (vegetation or land-cover), mixing layer theory, and the resolved water depth (e.g., Casas et al., 2010). These approaches included an analytic study based on a balance of gravitational force, surface and form drag (e.g., Huthoff et al., 2007), or employed a scaling parameter for incorporating local friction (e.g., Özgen et al., 2015). Although these methods do not solve the problem of how to effectively use subgrid topographical data, they point the way towards using more complex parameterizations including known local topography and bed forms, along with the scales of

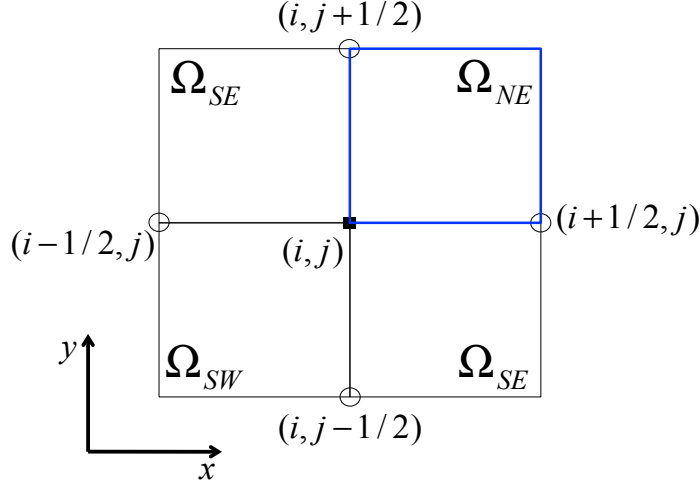


Figure 2.1: Quadtree grid

subgrid energy dissipation and flow processes.

The recent quadtree approach of [Volp et al. \(2013\)](#) introduced a new avenue for addressing the effect of local topography on the scales of subgrid energy dissipation and flow. In this method we let $F_{\Omega_{NE}}$ denote the friction (normalized by density) on the northeast sub-domain of a resolved-scale grid cell (Ω_{NE} , see [Figure 2.1](#)),

$$F_{\Omega_{NE}} = \int_{\Omega_{NE}} C_{Df} u_f \sqrt{(u_f^2 + v_f^2)} d\Omega_{NE}$$

where u_f and v_f are local velocity components in x and y -directions, respectively, and C_{Df} is local drag coefficient. By using an uniform friction slope over the subgrid region (i.e., $u_f^2/h_f \simeq \text{constant}$) and sub-domain volume-average velocities (i.e., $u \equiv$

$(1/V_{\Omega_{NE}}) \int_{\Omega_{NE}} u_f h_f d\Omega_{NE}$, where $V_{\Omega_{NE}}$ is the sub-domain volume), [Volp et al. \(2013\)](#) substituted a function of known topographic quantities, sub-domain volume, and resolved grid face velocities for unknown subgrid flow variables.

$$F_{\Omega_{NE}} = \frac{u_{i+1/2,j} \sqrt{(u_{i+1/2,j}^2 + v_{i,j+1/2}^2)} V_{\Omega_{NE}}}{H_{f\Omega_{NE}}} \quad (2.2)$$

Herein, $H_{f\Omega_{NE}}$ is a ‘‘friction depth’’: $H_{f\Omega_{NE}} \equiv \left[\int_{\Omega_{NE}} h_f \sqrt{h_f / C_{Df}} d\Omega_{NE} / V_{\Omega_{NE}} \right]^2$. The nomenclature, i and j are horizontal spatial indices for the Cartesian space (in x and y -direction, respectively); and u and v are the sub-domain-volume-averaged velocities. Note that the spatial indices $i + 1/2$ or $j + 1/2$ indicates the node at the center of a grid cell face boundary (Fig. 2.1). Summing frictions from each sub-domain provides the total friction on a resolved grid cell (i.e., $F_{\Omega} = F_{\Omega_{NE}} + F_{\Omega_{SE}} + F_{\Omega_{NW}} + F_{\Omega_{SW}}$). The friction model of [Volp et al. \(2013\)](#) was implemented into the mass and momentum model applying the ideas of [Defina \(2000\)](#) and [Casulli \(2009\)](#), and shown to reduce model sensitivity to grid scale (e.g., [Wu et al., 2016](#); [Volp et al., 2013](#)). The quadtree approach of [Volp et al. \(2013\)](#) has an effect of addressing horizontal and vertical shear effect caused by local obstructions distributed over each sub-domain, although the overall effect is limited by the use of only four sub-domains.

Chapter 3

Fine Resolution Environmental Hydrodynamics Model

3.1 Introduction

This chapter describes the numerical method of the Frehd model in Section 3.2, its governing equations in Section 3.3, and its bottom friction model in Section 3.4. The original approach of the Frehd model without a subgrid scheme in Section 3.5 becomes a baseline for the verification of the new subgrid models.

3.2 Numerical method

The Fine Resolution Environmental Hydrodynamics Model (herein, Frehd) is a numerical code for 2D and 3D hydrodynamic modeling, which is governed by the incompressible, hydrostatic, and free-surface Navier-Stoke equation (Hodges and Rueda, 2008; Rueda et al., 2007). The Frehd code solves the governing equations by the finite volume differencing, semi-implicit, and weighted predictor-corrector two time-level method (Hodges and Rueda, 2008; Rueda et al., 2007). Scalar transport (e.g., salinity) is solved with a mass-conserving scheme.

The numerical method of Frehd was built on the previous studies so as to facilitate a relatively large time-step; its predictor-corrector scheme is a family of

semi-implicit TRIM methods (Casulli and Cattani, 1994; Casulli and Cheng, 1992); The Frehd code adopts the advances of Hodges and Rueda (2008), which improved the semi-implicit θ method of Casulli and Cattani (1994) to the second order for barotropic and baroclinic terms; non-hydrostatic discretization of Frehd was founded on Wadzuk and Hodges (2004), which followed Casulli and Zanolli (2002). The Frehd code provides several turbulence models (e.g., mixing-length, 2D $\kappa - \epsilon$ model); however, for simplicity the present work uses only the 2D depth-integrated drag term and all the horizontal-shear turbulence models are disabled.

The Frehd code employs a uniform Cartesian grid with square or rectangular cells (square are used exclusively herein) with a hybrid of finite-difference and finite-volume techniques. The free-surface elevation at the center of a grid cell represents the average value over a grid cell. Face-normal velocities (and fluxes) are solved at the midpoint face of each grid cell in a standard staggered-grid finite difference formulation, as illustrated in Figure 3.1 for the (i, j) cell and its $(i + 1, j)$ and $(i, j + 1)$ neighbors. The solution of the depth-integrated incompressible conservation of mass and the kinematic boundary condition for a free surface is in an implicit (θ -weighted) approach that is effectively a finite-volume method ensuring conservation of volume to numerical precision. Explicit finite-difference discretizations are used for the velocity terms in momentum conservation, which are combined with the implicit free-surface gradients for a classic semi-implicit scheme. The nonlinear bottom drag term is discretized in a time-linearized approach so that the sign of the drag term is always consistent with the time $n + 1$ velocity direction and the drag magnitude incorporates the product of velocity from both time steps, e.g., $u^n u^{n+1}$.

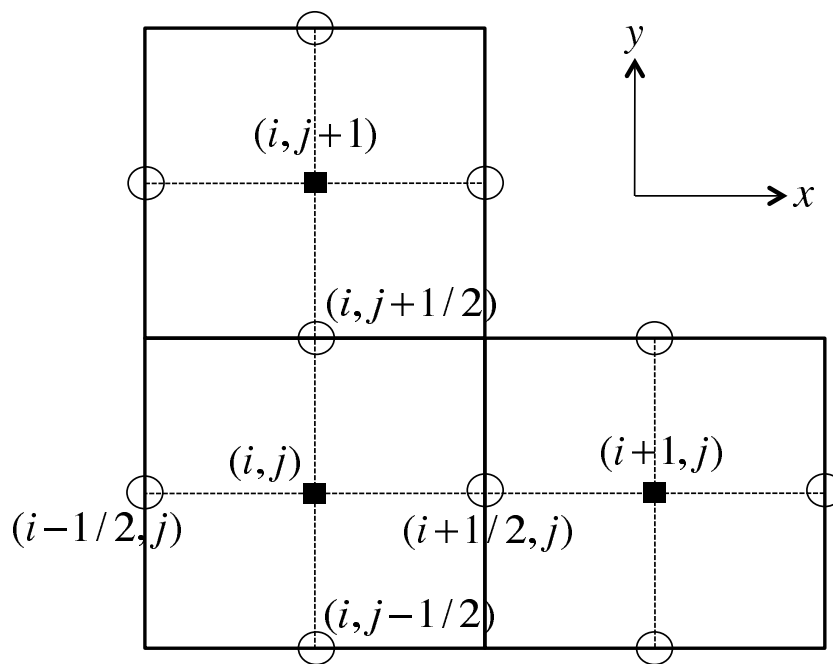


Figure 3.1: Computation nodes at a grid in Frehd. Squares: computational node for the free-surface elevation (η) and depth (h); Circles: computational nodes for velocities (u, v)

In the Frehd code, the boundary forcing can be driven by: (i) inflows, (ii) tidal elevations, (iii) precipitation, (iv) wind, and (v) thermal exchange with the atmosphere. In the present modeling, only the inflows and tidal elevation boundary conditions are used.

The Frehd code is suitable for 2D and 3D hydrodynamics of small to moderate-size water bodies, including river channels, estuaries, lagoons, lakes, and urban flooding. The code is implemented in Matlab, which effectively limits the efficiency of the algorithms and requires longer computational time than an equivalent code written in Fortran or C. However, Matlab provides a logical coding structure that is simpler to follow and is beneficial for efficient writing, debugging, and testing new algorithms. In this research, Frehd is used for the verification test of the subgrid methods along with the bathymetric data of the Nueces Delta, solving the depth-averaged, hydrostatic, uniform density, Navier-Stokes equation (commonly known as the 2D shallow water equations). The Frehd algorithms can be used with first or second-order discretizations in both time and/or space. For simplicity in code development and testing, the first-order discretizations are used for the present work.

3.3 2D shallow water equations

The 2D shallow water equations can be written as momentum and depth-integrated continuity combined with the kinematic boundary condition, providing:

$$\frac{\partial u_i}{\partial t} + u_j \frac{\partial u_i}{\partial x_j} + g \frac{\partial \eta}{\partial x_i} - \nu \frac{\partial^2 u_i}{\partial x_j \partial x_j} - \frac{\tau_{B_i}}{\rho h} - \frac{\tau_{S_i}}{\rho h} = 0 \quad : \quad i = \{1, 2\} \quad (3.1)$$

$$\frac{\partial \eta}{\partial t} + \frac{\partial}{\partial x_j} (hu_j) = 0 \quad (3.2)$$

where x_i denotes the Cartesian space; u_i are the depth-averaged velocity components in the horizontal Cartesian directions; η is the free surface elevation; ν is the horizontal turbulent eddy viscosity; τ_B is the bottom shear stress; τ_S is the surface shear stress; g is the gravitational acceleration; h is the flow depth; ρ is fluid density; and the Einstein summation convention is applied (unconventionally) over the set $j = \{1, 2\}$ for repeated subscripts; that is, the $j = 3$ advection and diffusion terms of the 3D momentum equations are wrapped into τ_B and τ_S . Note that wind forcing (τ_S) is neglected in this study.

3.4 Bottom friction model

The present study uses the drag model for the bottom shear stress τ_B in Eq. (3.1), which is a quadratic function of depth-averaged velocities and a drag coefficient C_D (Hervouet, 2007; Lightbody and Nepf, 2006).

$$\frac{\tau_{Bi}}{\rho h} = \frac{1}{2h} C_D u_i \sqrt{u_j u_j} : i, j = \{1, 2\} \quad (3.3)$$

The friction parameters are typically determined empirically or by using the prior experiment values (Hervouet, 2007). In Frehd, the user can choose either Manning's coefficient n or a drag coefficient C_D . where the conversion is the relationship used by Pasternack et al. (2006) and Ding et al. (2004), which provides the bottom shear stress term as

$$\frac{\tau_{Bi}}{\rho h} \equiv -\frac{g n^2}{\cos(\alpha) h^{4/3}} \vec{U} |U|$$

Where the bed slope is negligible, $\cos(\alpha) \approx 1$. Then, it follows:

$$C_D = \frac{2g n^2}{h^{1/3}}$$

An appropriate Manning's n can be estimated from land-cover data (e.g., 2001 National Land Cover Dataset), which has been linked to approximate values for Manning's n (Hossain et al., 2009).

3.5 Discrete free-surface solution

Herein we will only discuss the simplest forms of the Frehd discretization, specifically the first-order upwind approach. Discretization of momentum, Eq. (3.1) for the x direction in Frehd is:

$$\frac{(u_{i+1/2,j}^{n+1} - u_{i+1/2,j}^n)}{\Delta t} + N_{x\ i+1/2,j}^n + g \frac{(\eta_{i+1,j}^{n+1} - \eta_{i,j}^{n+1})}{\Delta x} - D_{xx\ i+1/2,j}^n - D_{yy\ i+1/2,j}^n - \frac{1}{(h_{i,j}^n + h_{i+1,j}^n)} C_D u_{i+1/2,j}^{n+1} \sqrt{[(u_{i+1/2,j}^n)^2 + (v_{i+1/2,j}^n)^2]} = 0$$

where n is the time index; i and j are horizontal spatial indices for the Cartesian space (in x and y -direction, respectively); x and y denote the Cartesian space; u and v are the depth-averaged velocity components in the Cartesian coordinates; h is the flow depth; C_D is the drag coefficient, and the N and D terms represent explicit nonlinear advection and turbulent diffusion discretization that are explicitly discretized as:

$$N_{x\ i+1/2,j}^n = u_{i+1/2,j}^n \frac{(u_{i+1/2,j}^n - u_{i-1/2,j}^n)}{\Delta x} + v_{i+1/2,j}^n \frac{(u_{i+1/2,j+1/2}^n - u_{i+1/2,j-1/2}^n)}{\Delta y}$$

$$D_{xx\ i+1/2,j}^n = \frac{1}{\Delta x} \left[(\nu_x)_{i+3/2,j} \frac{(u_{i+3/2,j}^n - u_{i+1/2,j}^n)}{\Delta x} - (\nu_x)_{i+1/2,j} \frac{(u_{i+1/2,j}^n - u_{i-1/2,j}^n)}{\Delta x} \right]$$

$$D_{yy\ i+1/2,j}^n = \frac{1}{\Delta y} \left[(\nu_y)_{i+1/2,j+1/2} \frac{(u_{i+1/2,j+1}^n - u_{i+1/2,j}^n)}{\Delta y} - (\nu_y)_{i+1/2,j-1/2} \frac{(u_{i+1/2,j}^n - u_{i+1/2,j-1}^n)}{\Delta y} \right]$$

where ν is horizontal turbulence eddy viscosity and the corner values (e.g., $u_{i+1/2,j+1/2}^n$) are obtained by interpolation from faces. The discrete time advance for x -momentum

is therefore

$$\begin{aligned}
u_{i+1/2,j}^{n+1} &= u_{i+1/2,j}^n - \Delta t N_{x\ i+1/2,j}^n - g \frac{\Delta t}{\Delta x} (\eta_{i+1,j}^{n+1} - \eta_{i,j}^{n+1}) \\
&\quad + \Delta t D_{xx\ i+1/2,j}^n + \Delta t D_{yy\ i+1/2,j}^n + \Delta t \frac{1}{2h_{i,j}^n} C_D u_{i+1/2,j}^{n+1} \sqrt{\left[\left(u_{i+1/2,j}^n \right)^2 + \left(v_{i+1/2,j}^n \right)^2 \right]}
\end{aligned} \tag{3.4}$$

and a similar equation for $v_{i,j+1/2}^{n+1}$ can be inferred.

For simplicity in exposition, let

$$\begin{aligned}
B_{x\ i+1/2,j}^n &\equiv \frac{1}{2h_{i,j}^n} C_D \sqrt{\left[\left(u_{i+1/2,j}^n \right)^2 + \left(v_{i+1/2,j}^n \right)^2 \right]} \\
I_{i+1/2,j}^n &\equiv \frac{1}{1 - \Delta t B_{x\ i+1/2,j}^n}
\end{aligned}$$

Then, Eq. (3.4) is:

$$\begin{aligned}
u_{i+1/2,j}^{n+1} &= I_{i+1/2,j}^n u_{i+1/2,j}^n - I_{i+1/2,j}^n \Delta t N_{x\ i+1/2,j}^n - I_{i+1/2,j}^n \frac{g\Delta t}{\Delta x} (\eta_{i+1,j}^{n+1} - \eta_{i,j}^{n+1}) \\
&\quad + I_{i+1/2,j}^n \Delta t D_{xx\ i+1/2,j}^n + I_{i+1/2,j}^n \Delta t D_{yy\ i+1/2,j}^n
\end{aligned} \tag{3.5}$$

Let an explicit source term, E_x , be defined as:

$$E_{x\ i+1/2,j}^n \equiv I_{i+1/2,j}^n (u_{i+1/2,j}^n - \Delta t N_{x\ i+1/2,j}^n + \Delta t D_{xx\ i+1/2,j}^n + \Delta t D_{yy\ i+1/2,j}^n)$$

Equation (3.5) is thus reduced to:

$$u_{i+1/2,j}^{n+1} = E_{x\ i+1/2,j}^n - I_{i+1/2,j}^n \frac{g\Delta t}{\Delta x} (\eta_{i+1,j}^{n+1} - \eta_{i,j}^{n+1}) \tag{3.6}$$

The flow continuity equation, Eq. (3.2), is implicitly discretized for the x -direction as:

$$\begin{aligned}
\eta_{i,j}^{n+1} - \eta_{i,j}^n &+ \frac{\Delta t}{\Delta x} h_{i,j}^n (u_{i+1/2,j}^{n+1} - u_{i-1/2,j}^{n+1}) \\
&+ \frac{\Delta t}{\Delta y} h_{i,j}^n (v_{i,j+1/2}^{n+1} - v_{i,j-1/2}^{n+1}) = \Delta t \frac{S_{i,j}^{n+1}}{\Delta x \Delta y}
\end{aligned} \tag{3.7}$$

where S includes all the external volume sources (e.g., inflows, precipitation). Substituting Eq. (3.6) for $u_{i+1/2,j}^{n+1}$ into Eq. (3.7) provides

$$\begin{aligned} \eta_{i,j}^{n+1} + \frac{\Delta t}{\Delta x} h_{i,j}^n \left[E_{x \ i+1/2,j}^n - I_{i+1/2,j}^n \frac{g\Delta t}{\Delta x} (\eta_{i+1,j}^{n+1} - \eta_{i,j}^{n+1}) \right] \\ - \frac{\Delta t}{\Delta x} h_{i,j}^n u_{i-1/2,j}^{n+1} + \frac{\Delta t}{\Delta y} h_{i,j}^n v_{i,j+1/2}^{n+1} - \frac{\Delta t}{\Delta y} h_{i,j}^n v_{i,j-1/2}^{n+1} = \eta_{i,j}^n + \Delta t \frac{S_{i,j}^{n+1}}{\Delta x \Delta y} \end{aligned}$$

Similar substitutions can be made for $u_{i-1/2,j}^{n+1}$, $v_{i,j+1/2}^{n+1}$, and $v_{i,j-1/2}^{n+1}$. The resulting discrete free surface equation is

$$\begin{aligned} \eta_{i,j}^{n+1} + \frac{\Delta t}{\Delta x} h_{i,j}^n E_{x \ i+1/2,j}^n - \frac{g(\Delta t)^2}{(\Delta x)^2} h_{i,j}^n I_{i+1/2,j}^n (\eta_{i+1,j}^{n+1} - \eta_{i,j}^{n+1}) \\ - \frac{\Delta t}{\Delta x} h_{i,j}^n E_{x \ i-1/2,j}^n + \frac{g(\Delta t)^2}{(\Delta x)^2} h_{i,j}^n I_{i-1/2,j}^n (\eta_{i,j}^{n+1} - \eta_{i-1,j}^{n+1}) \\ + \frac{\Delta t}{\Delta y} h_{i,j}^n E_{y \ i,j+1/2}^n - \frac{g(\Delta t)^2}{(\Delta y)^2} h_{i,j}^n I_{i,j+1/2}^n (\eta_{i,j+1}^{n+1} - \eta_{i,j}^{n+1}) \\ - \frac{\Delta t}{\Delta y} h_{i,j}^n E_{y \ i,j-1/2}^n + \frac{g(\Delta t)^2}{(\Delta y)^2} h_{i,j}^n I_{i,j-1/2}^n (\eta_{i,j}^{n+1} - \eta_{i,j-1}^{n+1}) \\ = \eta_{i,j}^n + \Delta t \frac{S_{i,j}^{n+1}}{\Delta x \Delta y} \end{aligned} \quad (3.8)$$

The discrete form can be compressed by defining explicit face coefficients as:

$$\begin{aligned} C_{i+1/2,j}^n &\equiv \frac{g(\Delta t)^2}{(\Delta x)^2} h_{i,j}^n I_{i+1/2,j}^n \\ C_{i-1/2,j}^n &\equiv \frac{g(\Delta t)^2}{(\Delta x)^2} h_{i,j}^n I_{i-1/2,j}^n \\ C_{i,j+1/2}^n &\equiv \frac{g(\Delta t)^2}{(\Delta y)^2} h_{i,j}^n I_{i,j+1/2}^n \\ C_{i,j-1/2}^n &\equiv \frac{g(\Delta t)^2}{(\Delta y)^2} h_{i,j}^n I_{i,j-1/2}^n \end{aligned}$$

and the cell-center coefficients as:

$$G_{i,j}^n \equiv \Delta t h_{i,j}^n \left(\frac{E_{x \ i+1/2,j}^n - E_{x \ i-1/2,j}^n}{\Delta x} + \frac{E_{y \ i,j+1/2}^n - E_{y \ i,j-1/2}^n}{\Delta y} \right)$$

Substituting C and G into Eq. (3.8) provides

$$\begin{aligned}
& \eta_{i,j}^{n+1} - C_{i+1/2,j}^m (\eta_{i+1,j}^{n+1} - \eta_{i,j}^{n+1}) + C_{i-1/2,j}^m (\eta_{i,j}^{n+1} - \eta_{i-1,j}^{n+1}) \\
& \quad - C_{i,j+1/2}^m (\eta_{i,j+1}^{n+1} - \eta_{i,j}^{n+1}) + C_{i,j-1/2}^m (\eta_{i,j}^{n+1} - \eta_{i,j-1}^{n+1}) + G_{i,j}^m \\
& = \eta_{i,j}^n + \Delta t \frac{S_{i,j}^{n+1}}{\Delta x \Delta y}
\end{aligned}$$

The above can be written as a linear matrix equation for implicit solution of η^{n+1} :

$$\begin{aligned}
& \eta_{i,j}^{n+1} (1 + C_{i+1/2,j}^m + C_{i-1/2,j}^m + C_{i,j+1/2}^m + C_{i,j-1/2}^m) & (3.9) \\
& \quad - \eta_{i+1,j}^{n+1} C_{i+1/2,j}^m - \eta_{i-1,j}^{n+1} C_{i-1/2,j}^m - \eta_{i,j+1}^{n+1} C_{i,j+1/2}^m - \eta_{i,j-1}^{n+1} C_{i,j-1/2}^m \\
& = \eta_{i,j}^n + \Delta t \frac{S_{i,j}^{n+1}}{\Delta x \Delta y} - G_{i,j}^m
\end{aligned}$$

Once the solution for η^{n+1} is obtained, the velocities $u_{i+1/2,j}^{n+1}$ and $v_{i,j+1/2}^{n+1}$ can be found as an explicit solution from Eq. (3.4), and from a similar equation inferred for the y -momentum. This completes the classic semi-implicit solution for a single time step.

Chapter 4

Subgrid Drag Model

4.1 Introduction

The need for a subgrid drag model can be motivated quite simply: the drag term in a momentum equation typically has a functional form of $C_D u^2$, where C_D is an empirical drag coefficient or a friction parameter, and u^2 is the square of the flow speed. If \bar{u} is the average flow speed in a model grid cell, and u_i for $i = \{1 \dots N\}$ are a set of subgrid flow speeds such that if $\bar{u} = \sum_i u_i / N$, then $C_D \bar{u}^2 \neq C_D \sum_i u_i^2 / N$. Thus, a modified C_D is required to account for the influence of subgrid topographic variability on local velocities. Furthermore, it follows that any C_D that correctly accounts for subgrid features is inherently grid-dependent rather than a simple physical parameter, so a calibration of C_D for a particular model grid might not be informative of the correct C_D for any other grid.

The sensitivity of hydrodynamic model results to a friction parameter is generally accepted (Néelz and Pender, 2007; Lane, 2005), although Hardy et al. (1999) noted results were more dependent on the model grid scale. Subgrid topography is known to generate a drag force on a flow, thereby affecting the flow route, flow rate, spatial coverage, and temporal behavior. Moreover, a number of studies (e.g., Chisolm, 2011; Casas et al., 2010) showed that a friction or roughness parameter

required modification as a model grid was coarsened, implying a fundamental grid dependence.

Model friction parameters are sometimes set using values from the literature (Hicks and Mason, 1991) or, more commonly, by calibration (e.g., Sahoo et al., 2006; Horritt and Bates, 2001). Using literature values can be problematic because of grid dependence when the topographic features are not fully resolved and the relationship between numerical dissipation and the energy dissipation implied by the friction parameter is not known. Because of nonlinearity, locally-higher velocities within limited subgrid areas have a greater effect on the resolved-scale energy losses than the resolved-scale velocity (Volp et al., 2013). This idea is readily illustrated by considering a resolved grid cell of area A where a subgrid region of $A/3$ has a velocity of 0.5 m/s and the complementary region of $2A/3$ has a velocity of only 0.1 m/s. The area integrated frictional losses would be roughly $(0.08C_{D(f)} + 0.007C_{D(s)})A$ where $C_{D(f)}$ and $C_{D(s)}$ are drag coefficients of the fast and slow velocity regions, respectively. Clearly, if the C_D are of similar magnitudes then the integrated frictional losses are dominated by the losses in the high speed region. Ideally, a model friction parameter should be set from known topography, bed forms, and other roughness elements by applying an understanding of how the scales of resolved flow processes relate to the scales of subgrid energy dissipation; calibration should be, at most, a small perturbation that reflects the uncertainties associated with estimates of the friction parameter. Unfortunately, this is only possible if we can understand and relate the effects of subgrid topography over a range of flow conditions to the modeled drag.

The problem of handling subgrid friction or roughness has been previously

noted (Lane, 2005; Defina, 2000) and there is a wide literature on the similar problem of flow-through roughness of vegetation, but there are few quantitative works on methods for estimating drag effect exerted by subgrid topographic solid elements. Early studies have addressed local frictional properties in various ways: Carney et al. (2006) assumed a known statistical probability function; in classic papers, Horton (1933, (recited from Woo (2001))) and Lotter (1933, (recited from Yang et al. (2005))) assumed the subgrid scale flow quantities were equally distributed so as to apply a continuity law. Time and space-varying friction parameters were introduced by Casas et al. (2010), using local roughness heights and mixing layer theory. Stem drag exerted by solid submerged objects or vegetation has been scaled with depth-averaged flow quantities through the analytic studies based on a steady force balance between the shear frictional force and the gravitational force (Buckman, 2013; Huthoff et al., 2007). Volp et al. (2013) recently presented a quadtree grid approach representing local frictional effects created by subgrid topography over a quarter of a grid cell, however it is not clear the method can be practically generalized to a larger number of subgrid domains.

Building on prior work, the present study develops a systematic method for determining drag coefficients to represent energy dissipation effects of subgrid-scale topography. The advantage of the new subgrid drag model is that it dynamically approximates the resolved-grid scale effects of the subgrid flow area including effects of time-varying water surface elevation and emergent topography. For model formulation, we consider a “fine grid” system which consists of uniform raster whose outer cells share a boundary with the model-resolved grid (see Section 4.2.2). A resolved

grid-wise momentum solution is approximated with the spatially-averaged fine-grid momentum solutions over the resolved grid area (see Section 4.2.3). The integrated fine-grid momentum over the coarse-grid area is represented as a function of subgrid topographic quantities, the resolved grid scale, and the resolved flow variables (see Section 4.2.4). This new approach provides dynamic drag coefficients incorporating the effect of local forcing distributed over the resolved grid cell into a coarse-grid momentum model; however, flow processes caused by subgrid horizontal shear (e.g., circulation, backwater) within a resolved grid cell are excluded in the model and remain a subject for future study.

The new model is tested in Chapter 6 using the Frehd code (Chapter 3) with a fine-grid scale grid of 1×1 m and a coarse-grid scale grid of 15×15 m derived from lidar and survey topography of the Nueces River Delta (Appendix A). The new subgrid drag model will be implemented into the new subgrid model developed in Chapter 5 as the combined subgrid model to examine the effectiveness of a coupled approach.

4.2 Model formulation

4.2.1 Momentum equation

The 2D shallow water momentum equation, Eq. (3.1), where the free surface shear stress (τ_S) is neglected and the bottom shear stress (τ_B) is parameterized by a drag coefficient (C_D) can be written as

$$\frac{\partial u_i}{\partial t} + u_j \frac{\partial u_i}{\partial x_j} + g \frac{\partial \eta}{\partial x_i} - \nu \frac{\partial^2 u_i}{\partial x_j \partial x_j} - \frac{1}{2h} C_D u_i \sqrt{u_j u_j} = 0 \quad : \quad i = \{1, 2\} \quad (4.1)$$

where x_i denotes the Cartesian space; u_i are the velocity components in Cartesian directions, η is the free surface elevation; g is the gravitational acceleration; ν is horizontal turbulent eddy viscosity; h is the flow depth, and the Einstein summation convention is applied over the set $j = \{1, 2\}$ for repeated subscripts.

4.2.2 Fine-grid system

For the subgrid drag method, we consider a single topographical elevation for each model-resolved grid cell (i.e., over which the hydrodynamic equations are solved) with known local subgrid topographical perturbations from this elevation. It will be convenient to use “coarse grid” to refer to the model-resolved grid scales and “fine grid” to refer to the subgrid bathymetry. For simplicity, we will restrict our derivation to a system wherein the fine grid can be described by a uniform raster whose outer cells share a common boundary with the coarse grid, as illustrated in Figure 4.1.

4.2.3 Integration of fine-grid momentum

Equation (4.1) can be used to obtain a fine-grid momentum equation for the coordinate system (r, s) in the r direction, which is parallel to the x -direction in the Cartesian space as:

$$\frac{\partial u_f}{\partial t} + u_f \frac{\partial u_f}{\partial r} + v_f \frac{\partial u_f}{\partial s} + g \frac{\partial \eta_f}{\partial r} - \frac{1}{2h_f \cos \alpha_f} C_{Df} (u_f)^2 = 0 \quad (4.2)$$

where the f subscripts indicate fine-grid values, u and v are velocities in r and s directions, C_{Df} is a subgrid drag coefficient, and α is an angle of flow direction.

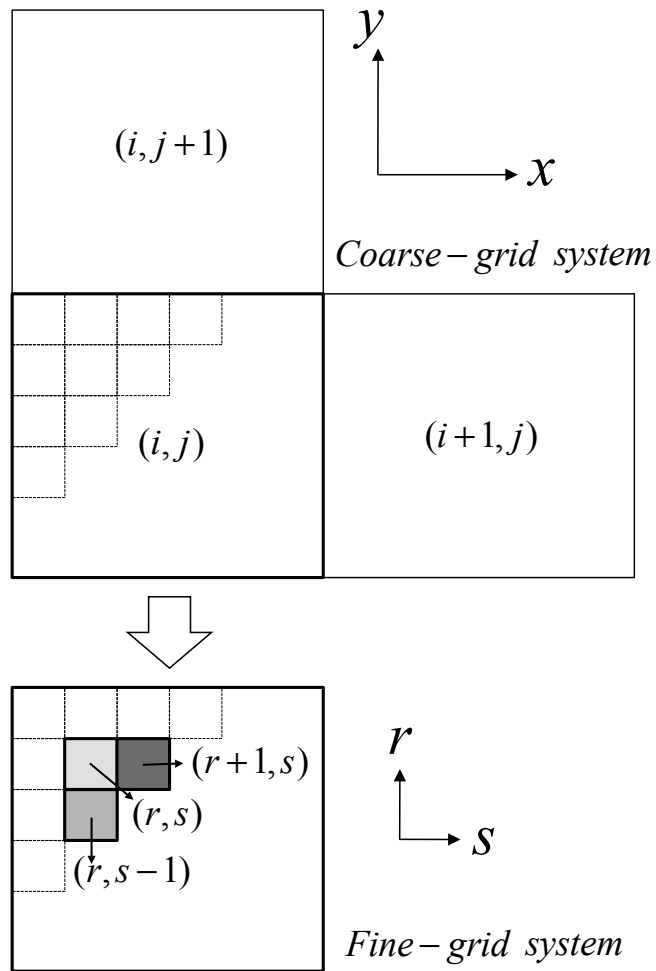


Figure 4.1: Coarse-grid (i, j) and fine-grid (r, s) coordinate systems

Noting that from geometry, an angle of flow direction can be defined that

$$\cos \alpha = \frac{u}{\sqrt{u^2 + v^2}}$$

For $u = v = 0$, $\cos \alpha$ is set to be unity in order to prevent flow in immobile zones which is an unphysical result.

It may be noted that Eq. (4.2) does not include the horizontal eddy-viscosity term of Eq. (4.1). Neglecting this term is effectively an assumption that the fine-grid bottom shear dominates the fine-grid horizontal shear, which is likely the case for shallow flows but might be problematic for narrow channels in complex topography. The subject of subgrid turbulence modeling for horizontal shear is an additional layer of complexity that is not attempted in the present research.

A coarse-grid momentum equation in the x direction can be written similar to Eq. (4.2), but where the lack of subscripts implies coarse-grid values. The result is:

$$\frac{\partial u}{\partial t} + u \frac{\partial u}{\partial x} + v \frac{\partial u}{\partial y} + g \frac{\partial \eta}{\partial x} - \frac{1}{2h \cos \alpha} C_{Dx} u^2 = 0 \quad (4.3)$$

where C_{Dx} represents a coarse-grid drag coefficient for the x direction that may be different from C_{Dy} that is used in a similar y direction momentum equation.

Non-dimensionalized fine-grid variables can be defined as

$$\begin{aligned}
 t^* &\equiv \frac{t\sqrt{u^2 + v^2}}{h} \\
 r^* &\equiv \frac{r}{h} \\
 u_f^* &\equiv \frac{u_f}{\sqrt{(u^2 + v^2)}} \\
 h_f^* &\equiv \frac{h_f}{h} \\
 \eta_f^* &\equiv \frac{\eta_f}{h}
 \end{aligned}$$

where non-dimensional coarse-grid variables follow similarly as x^*, u^*, h^*, η^* and a non-dimensional grid-cell surface area A^* where dimensional coarse-grid $A = \Delta x \Delta y$.

$$\begin{aligned}
 x^* &\equiv \frac{x}{h} \\
 u^* &\equiv \frac{u}{\sqrt{(u^2 + v^2)}} \\
 h^* &\equiv \frac{h}{h} \\
 \eta^* &\equiv \frac{\eta}{h} \\
 \Delta x^* &\equiv \frac{\Delta x}{h} \\
 \Delta y^* &\equiv \frac{\Delta y}{h} \\
 A^* &\equiv \Delta x^* \Delta y^*
 \end{aligned}$$

The Froude number is defined with coarse-grid variables as:

$$F^2 \equiv \frac{(u^2 + v^2)}{gh}$$

To non-dimensionalize Eq. (4.2), we first multiply through by $\sqrt{u^2 + v^2}/h$,

which provides

$$\begin{aligned} \frac{(u^2 + v^2)}{h} \frac{\partial u_f}{\partial t} + \frac{(u^2 + v^2)}{h} u_f \frac{\partial u_f}{\partial r} + \frac{(u^2 + v^2)}{h} v_f \frac{\partial u_f}{\partial s} + \frac{(u^2 + v^2)}{h} g \frac{\partial \eta_f}{\partial r} \\ - \frac{(u^2 + v^2)}{h} \frac{1}{2h_f \cos \alpha_f} C_{Df}(u_f)^2 = 0 \end{aligned}$$

Substituting the non-dimensional relationships provides the non-dimensional fine-grid equation as

$$\frac{\partial u_f^*}{\partial t^*} + u_f^* \frac{\partial u_f^*}{\partial r^*} + v_f^* \frac{\partial u_f^*}{\partial s^*} + \frac{1}{F^2} \frac{\partial \eta_f^*}{\partial r^*} - \frac{1}{2h_f^* \cos \alpha_f} C_{Df}(u_f^*)^2 = 0 \quad (4.4)$$

Similarly, the coarse-grid non-dimensional form of Eq. (4.3) is:

$$\frac{\partial u^*}{\partial t^*} + u^* \frac{\partial u^*}{\partial x^*} + v^* \frac{\partial u^*}{\partial y^*} + \frac{1}{F^2} \frac{\partial \eta^*}{\partial x^*} - \frac{1}{2h^* \cos \alpha} C_{Dx}(u^*)^2 = 0 \quad (4.5)$$

To develop an upscaled version of the non-dimensional fine-grid equation, we define a spatial averaging operator ($\overline{\theta_f^*}$) for any variable θ_f^* over a coarse-grid area as

$$\overline{\theta_f^*} \equiv \frac{1}{A^*} \int \theta_f^* dA^*$$

We further define a coarse-grid variable θ^* as the coarse-grid average of fine-grid variables $\overline{\theta_f^*}$.

$$\theta^* \equiv \overline{\theta_f^*} \quad (4.6)$$

Applying the spatial averaging operator to the non-dimensional fine-grid Eq. (4.4),

we get

$$\frac{\partial \overline{u_f^*}}{\partial t^*} + \overline{u_f^*} \frac{\partial \overline{u_f^*}}{\partial r^*} + \overline{v_f^*} \frac{\partial \overline{u_f^*}}{\partial s^*} + \frac{1}{F^2} \frac{\partial \overline{\eta_f^*}}{\partial r^*} - \frac{1}{2h_f^* \cos \alpha_f} C_{Df}(u_f^*)^2 = 0 \quad (4.7)$$

If we use Eq. (4.6) to replace the coarse grid variables (except the drag term) with the equivalent spatially-averaged fine-grid variables in Eq. (4.5), we obtain

$$\frac{\partial \overline{u_f^*}}{\partial t^*} + \overline{u_f^*} \frac{\partial \overline{u_f^*}}{\partial x^*} + \overline{v_f^*} \frac{\partial \overline{u_f^*}}{\partial y^*} + \frac{1}{F^2} \frac{\partial \overline{\eta_f^*}}{\partial x^*} - \frac{1}{2h^* \cos \alpha} C_{Dx}(u^*)^2 = 0 \quad (4.8)$$

Subtracting Eq. (4.7) from Eq. (4.8) provides the relationship between the integrated fine-grid drag coefficient, the coarse-grid drag coefficient, and the nonlinear advection terms as:

$$\overline{u_f^* \frac{\partial u_f^*}{\partial x^*}} - \overline{u_f^*} \frac{\partial \overline{u_f^*}}{\partial x^*} + \overline{v_f^* \frac{\partial u_f^*}{\partial y^*}} - \overline{v_f^*} \frac{\partial \overline{u_f^*}}{\partial y^*} - \frac{1}{2h^* \cos \alpha} C_{Dx}(u^*)^2 + \overline{\frac{1}{2h_f^* \cos \alpha_f} C_{Df}(u_f^*)^2} = 0 \quad (4.9)$$

The first four terms of Eq. (4.9) represent the subgrid contributions of advection in a form similar to the Leonard terms derived in Large Eddy Simulation (LES) models. Arguably, these terms could be used to represent channelization, obstructions, and horizontal shear effects from subgrid topology. However, the present study focuses on the subgrid contributions of drag and we have already neglected the turbulent eddy viscosity term in Eq. (4.2), so we make the consistent assumption that these subgrid advection contributions can be also neglected, i.e.,

$$\overline{u_f^* \frac{\partial u_f^*}{\partial x^*}} \approx \overline{u_f^*} \frac{\partial \overline{u_f^*}}{\partial x^*}$$

$$\overline{v_f^* \frac{\partial u_f^*}{\partial y^*}} \approx \overline{v_f^*} \frac{\partial \overline{u_f^*}}{\partial y^*}$$

From the above it follows that a relationship between the C_{Dx} and C_{Df} is

$$C_{Dx} = \frac{h^* \cos \alpha}{(u^*)^2} \overline{\frac{1}{h_f^* \cos \alpha_f} C_{Df}(u_f^*)^2}$$

As the coarse-grid variables are uniform over the averaging space, the above can be written more simply as

$$C_{Dx} = \frac{\overline{h^* \cos \alpha (u_f^*)^2}}{h_f^* \cos \alpha_f (u^*)^2} C_{Df} \quad (4.10)$$

The above provides the fundamental equation for a representing fine-grid space-time varying velocities and water depths along with spatially-varying drag coefficients within a directional drag coefficient C_{Dx} , with a similar equation implied for the y direction using C_{Dy} .

4.2.4 Approximation of subgrid flow velocities

Consistent with neglecting horizontal shear effects, we assume the flux across a coarse-grid face can be approximated as uniformly distributed across all the fine-grid cells coincident with the face, i.e., there is only a single value of u_f^* for multiple fine grid cell faces along a coarse-grid cell face characterized by u^* . It follows that

$$A_{fx}^* u_f^* \approx \Delta y^* h^* u^*$$

where for some position r along the fine-grid axes (r, s) we can define the total fine grid area normal to the x axis as

$$A_{fx}^*|_r \equiv \int_{\Delta y^*} h_f^*|_{(r,s)} ds^*$$

Thus, the fine grid velocity accounts for the difference between the coarse-grid flow area and the fine grid flow area as:

$$u_f^* = \frac{\Delta y^* h^*}{A_{fx}^*} u^*$$

Consistent with neglecting subgrid horizontal shear, we assume that the directional angle of the subgrid velocities is similar to the coarse-grid velocities, i.e.,

$$\frac{\cos \alpha}{\cos \alpha_f} \approx 1$$

It is convenient to write the spatial averaging operator as a double integration over the (r, s) axes, such that

$$C_{Dx} = \frac{1}{A^*} \int_{\Delta x^*} \int_{\Delta y^*} \frac{(h^*)^3 (\Delta y^*)^2}{h_f^* (A_{fx}^*)^2} C_{Df} ds^* dr^*$$

The above equation can be written as

$$\begin{aligned} C_{Dx} &= \frac{(h^*)^3 (\Delta y^*)^2}{A^*} \int_{\Delta x^*} \left(\frac{1}{A_{fx}^*} \right)^2 \int_{\Delta y^*} \frac{1}{h_f^*} C_{Df} ds^* dr^* \\ &= (h^*)^3 \frac{\Delta y^*}{\Delta x^*} \int_{\Delta x^*} \left(\frac{1}{A_{fx}^*} \right)^2 \int_{\Delta y^*} \frac{1}{h_f^*} C_{Df} ds^* dr^* \end{aligned}$$

Noting that $h^* \equiv 1$, it follows that separate time-dependent drag coefficients for x and y directions are

$$C_{Dx}(t) = \left(\frac{\Delta y^*}{\Delta x^*} \right) \int_{\Delta x^*} \left(\frac{1}{A_{fx}^*} \right)^2 \int_{\Delta y^*} \frac{1}{h_f^*} C_{Df} ds^* dr^* \quad (4.11)$$

$$C_{Dy}(t) = \left(\frac{\Delta x^*}{\Delta y^*} \right) \int_{\Delta y^*} \left(\frac{1}{A_{fy}^*} \right)^2 \int_{\Delta x^*} \frac{1}{h_f^*} C_{Df} dr^* ds^* \quad (4.12)$$

where all terms on the right-hand side are functions of t except for Δx^* , Δy^* , and C_{Df} .

To prevent an infinite values for coarse-grid drag coefficient in Eqs. (4.11) and (4.12), we require non-dimensional lower cutoff bounds (β) such that

$$\begin{aligned} \frac{1}{h_f^*} < \beta_h &\rightarrow \frac{1}{h_f^*} = \beta_h \\ \left(\frac{1}{A_{fx}^*}\right)^2 < \beta_f &\rightarrow \left(\frac{1}{A_{fx}^*}\right)^2 = \beta_f \\ \left(\frac{1}{A_{fy}^*}\right)^2 < \beta_f &\rightarrow \left(\frac{1}{A_{fy}^*}\right)^2 = \beta_f \end{aligned}$$

The above can be written as minimum requirements:

$$\begin{aligned} h_f^*(r, s) &= \min \left[h_f^*, \frac{1}{\beta_h} \right] \\ A_{fx}^*(r) &= \min \left[A_{fx}^*(r), \frac{1}{\beta_f^{1/2}} \right] \\ A_{fy}^*(s) &= \min \left[A_{fy}^*(s), \frac{1}{\beta_f^{1/2}} \right] \end{aligned}$$

To prevent unphysical damping that is greater than the kinetic energy available in the flow, the β_f and β_h should be selected for the range of expected h_f^* , A_{fx}^* and A_{fy}^* values such that $C_{Dx} \leq 1$ and $C_{Dy} \leq 1$.

The above formulations for C_{Dx} and C_{Dy} require subgrid depths h_f and sub-grid cross-sectional areas A_{fx} , A_{fy} to be known. The time-varying difference between the fine-grid bottom and coarse-grid bottom can be denoted as $\delta z(r, s, t)$, which is defined with a fine-grid topographic elevation $z_b(r, s)$, a coarse-grid bottom elevation Z_b that is uniform over subgrid space, and time-varying model-resolved water depth h .

$$\delta z(r, s, t) \equiv \min [z_b(r, s) - Z_b, h(t)] \quad (4.13)$$

Thus, $\delta z(r, s)$ is constant with time only if the coarse-grid depth is greater than the difference between the fine and coarse topography. The non-dimensional form for Eq. (4.13) is

$$\delta z^* \equiv \frac{\delta z}{h}$$

The subgrid depths h_f at the time t are estimated by subtracting δz from the model-resolved water depth h at the time t .

$$h_f(r, s, t) = h(t) - \delta z(r, s, t) \quad (4.14)$$

The above approach ensures that $h_f(r, s) = 0$ when the coarse-grid free-surface elevation is less than the $z_b(r, s)$ subgrid topographic elevation.

As a control case, we can consider the simple spatial average of the drag coefficient (without any depth weighting) as a simple upscaling model. Note that this approach produces a single coarse-grid drag coefficient, C_{Da} that is identical in both x and y directions and constant through time.

$$C_{Da} \equiv \frac{1}{A^*} \int_{\Delta x^*} \int_{\Delta y^*} C_{Df}(r, s) ds^* dr^* \quad (4.15)$$

Comparison of the control case with directional drag coefficients of Eqs. (4.11) and (4.12) provides a method of quantifying the behavior of the dynamic algorithm. The capabilities and limitations of the time-varying C_{Dx} and C_{Dy} for representing subgrid effects are analyzed in Chapter 6.

Chapter 5

Subgrid Momentum Model and Solution

5.1 Introduction

This portion of the study develops a subgrid method accounting for subgrid topographic effects on surface stresses, pressure gradients, and flow continuity for the integrated fluxes at grid cell faces, which are needed obtain mass and momentum conservation at the resolved-grid scale. The new ideas are built on foundations pioneered by [Casulli \(2009\)](#) and [Volp et al. \(2013\)](#) (see Chapter 2). This new momentum-based subgrid method addresses the effect of frictional forcing on the subgrid scale by approximating the integrated subgrid shear from the resolved velocity and topography (see Section 5.2). The new subgrid formulation is completed by substituting discrete versions of momentum for velocities at the cell faces into discrete continuity (see Section 5.3). The incompressible flow continuity is constructed by applying the approach of the [Casulli \(2009\)](#) to flux integration at the faces of a grid cell. In addition, this study applies a subgrid topography sampling method, building on the idea of [Li \(2015\)](#). The sampling method is implemented within the subgrid momentum method so as to capture the effect of minor flow channels below a resolved grid cell bottom elevation (see Section 5.4).

5.2 Subgrid momentum model

Newton's second law defines a force on a particle of mass M and x velocity component u as

$$\sum F_x = M \frac{Du}{Dt} \quad (5.1)$$

where D/Dt is the material derivative following a particle. A balance of forces on the moving water element can be constructed using surface forces F_s (e.g., pressure forces, surface frictional forces) and body forces F_b (e.g., gravitational forces). A surface force along the face of a grid cell can be obtained by integrating a stress or pressure around the face. For example, an xz plane has a τ_{xy} shear stress that exerts a force in the x direction due to velocity shear in the y direction, so that the contribution to the force is

$$F_{s(x)} = \int_{A_{xz}} \tau_{xy} dA$$

Figure 5.1 is a schematic sketch that illustrates surface forces summed along the *net flow areas* for the x direction. It is convenient to denote the vertical faces of a resolved grid cell as \overline{abcd} , \overline{efgh} , \overline{abfe} , and \overline{cdhg} . Summing the forces in the x direction along the *net flow areas* on vertical faces of a grid cell and including the bottom shear stress (τ_{Bx}) provides

$$\begin{aligned} \sum F_x = & - \left[(pA_{yz})_{\overline{abcd}} - (pA_{yz})_{\overline{efgh}} \right] + \left[(\tau_{xx}A_{yz})_{\overline{abcd}} - (\tau_{xx}A_{yz})_{\overline{efgh}} \right] \\ & + \left[(\tau_{yx}A_{xz})_{\overline{abfe}} - (\tau_{yx}A_{xz})_{\overline{cdhg}} \right] + (\tau_{Bx}A_{xy}) \end{aligned} \quad (5.2)$$

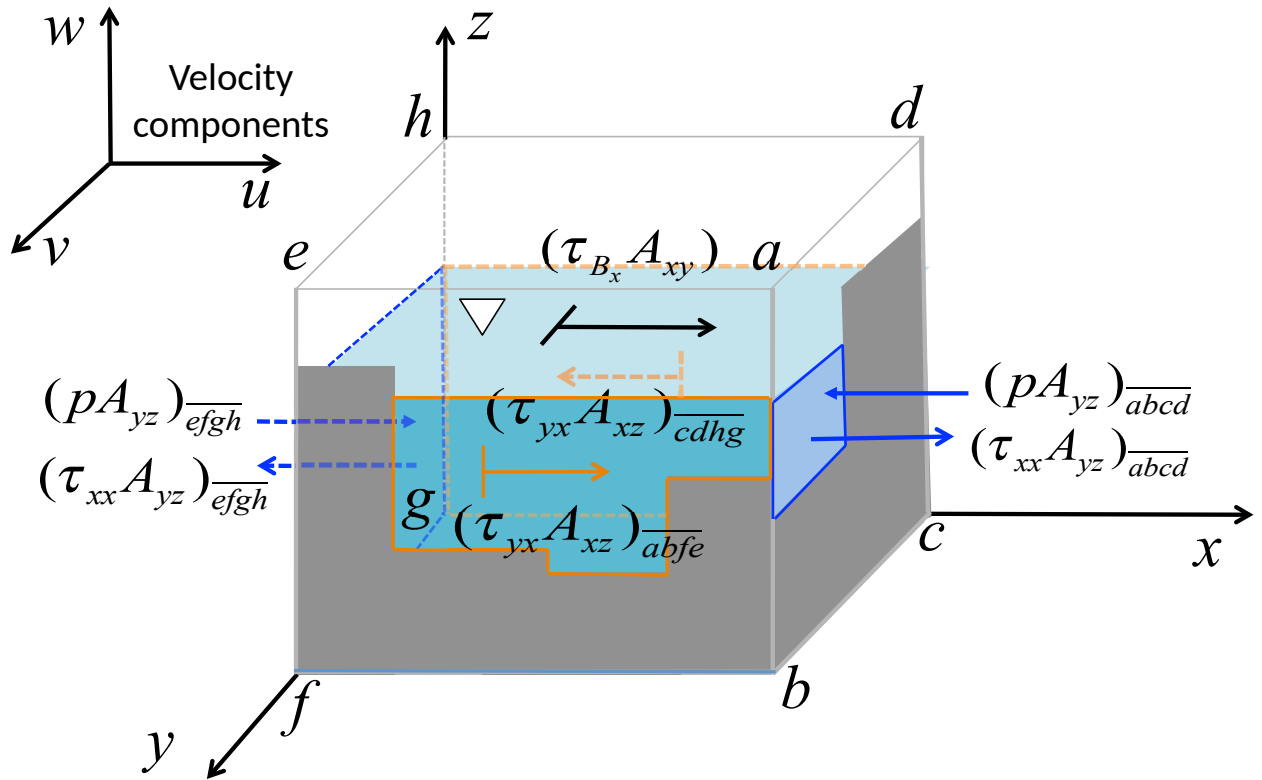


Figure 5.1: Surface forces exerting on the net face flow areas of a resolved grid cell

where p is the pressure, τ_{xx} , τ_{yx} , and τ_{Bx} are the normal, shear, and bottom shear stress for the x -direction. The variable τ_{yx} indicates a stress in the x -direction exerted on a plane perpendicular to the y -direction.

5.2.1 Inertia and advection

Using $M = \rho V$, where ρ is the fluid density and V is a volume, the momentum in terms of the material derivative in the x direction in Eq. (5.1) can be converted using the Reynolds Transport Theorem applied to a finite volume,

$$\frac{D}{Dt} \int_{\Omega} \rho u dV = \int_{\Omega(t)} \frac{\partial(\rho u)}{\partial t} dV + \int_{\partial\Omega(t)} \rho (\bar{U} \cdot \hat{n}) u dA \quad (5.3)$$

where \bar{U} is a vector velocity and \hat{n} is a normal vector that is positive pointing outward from Ω . Approximating $\partial u/\partial t$ as uniform over a finite volume and requiring $\partial V/\partial t$ to be sufficiently small (i.e., in a numerical time step of Δt we require $\Delta t \partial V/\partial t \ll V$), then

$$\int_{\Omega(t)} \frac{\partial(\rho u)}{\partial t} dV \approx \rho V \frac{\partial u}{\partial t} \quad (5.4)$$

Approximating u on a face as uniform, and requiring $\partial A/\partial t$ to be sufficiently small, we obtain

$$\int_{\partial\Omega(t)} \rho (\bar{U} \cdot \hat{n}) u dA \approx \sum_{f \in \partial\Omega} \rho u_f Q_f \quad (5.5)$$

where Q_f is a volume flux given a sign that is negative for an inflow and positive for an outflow. Substituting Eqs. (5.4) and (5.5) into Eq. (5.3) and then putting the result back into Eq. (5.1) provides

$$\sum F_x = \rho V \frac{\partial u}{\partial t} + \sum_{f \in \partial\Omega} \rho u_f Q_f$$

Noting that $Q = uA$ for uniform velocities over a cross-sectional area, a discrete form of inertia and advection at the edge of a grid cell can be defined from the above using a first-order upwind scheme as:

$$\begin{aligned} \sum F_x = \rho V \frac{(u_{i+1/2,j}^{n+1} - u_{i+1/2,j}^n)}{\Delta t} + \rho u_{i+1/2,j}^n (A_{yz}^n)_{i+1/2,j} (u_{i+1/2,j}^n - u_{i-1/2,j}^n) \\ + \rho v_{i+1/2,j}^n (A_{xz}^n)_{i+1/2,j} (u_{i+1/2,j}^n - u_{i+1/2,j-1}^n) \end{aligned} \quad (5.6)$$

where n is the time index; i and j is horizontal spatial indices for the Cartesian space (in x and y -direction, respectively); and u and v are the depth-averaged velocity components in the Cartesian directions, respectively.

5.2.2 Frictional forces

The friction forces are obtained by integrating the surface stresses over the edges of a grid cell.

$$F_{x(friction)} = \int_{A_{yz}} \tau_{xx} dA + \int_{A_{xz}} \tau_{yx} dA + \int_{A_{xy}} \tau_{B_x} dA$$

Expressing the surface stresses with velocity gradients (Stokes, 1845),

$$\tau_{xx} = \lambda \nabla \cdot \bar{U} + 2\mu \frac{\partial u}{\partial x} \quad (5.7)$$

$$\tau_{yx} = \tau_{xy} = \mu \left(\frac{\partial v}{\partial x} + \frac{\partial u}{\partial y} \right) \quad (5.8)$$

where μ is the molecular viscosity coefficient and λ is the bulk viscosity coefficient. Based on the incompressible mass conservation relationship,

$$\nabla \cdot \bar{U} = 0, \text{ thus, } \tau_{xx} = 2\mu \frac{\partial u}{\partial x}$$

The bottom shear stress can be modeled as a quadratic function with depth-averaged velocities and a drag coefficient C_D (Hervouet, 2007; Lightbody and Nepf, 2006).

$$\tau_{B_x} = \frac{1}{2} \rho C_{D_x} u \sqrt{u^2 + v^2}$$

The discrete form of frictional forces can be approximated with the first-order upwind scheme as:

$$\begin{aligned} F_{x(friction)} = & \left[(\tau_{xx}^n)_{i+3/2,j} (A_{yz}^n)_{i+3/2,j} - (\tau_{xx}^n)_{i+1/2,j} (A_{yz}^n)_{i+1/2,j} \right] \\ & + \left[(\tau_{yx}^n)_{i+1/2,j} (A_{xz}^n)_{i+1/2,j} - (\tau_{yx}^n)_{i-1/2,j} (A_{xz}^n)_{i-1/2,j} \right] + (\tau_{B_x}^{n+1})_{i+1/2,j} (A_{xy}^n)_{i,j} \end{aligned} \quad (5.9)$$

where τ_{B_x} term is discretized with the implicit velocity $u_{i+1/2,j}^{n+1}$; the surface stresses τ_{xx} and τ_{yx} , and the face areas A_{yz} , A_{xz} , and A_{xy} at the edges and the bottom of a grid cell are explicitly discretized. Substituting Eqs. 5.7 and 5.8 into Eq. 5.9 provides

$$\begin{aligned} F_{x(friction)} = & 2(\nu_x)_{i+1/2,j} \rho (A_{yz}^n)_{i+1/2,j} \frac{(u_{i+3/2,j}^n - u_{i+1/2,j}^n)}{\Delta x} \\ & - 2(\nu_x)_{i-1/2,j} \rho (A_{yz}^n)_{i-1/2,j} \frac{(u_{i+1/2,j}^n - u_{i-1/2,j}^n)}{\Delta x} \\ & + (\nu_y)_{i+1/2,j} \rho (A_{xz}^n)_{i+1/2,j} \left[\frac{(v_{i+3/2,j}^n - v_{i+1/2,j}^n)}{\Delta x} + \frac{(u_{i+1/2,j+1}^n - u_{i+1/2,j}^n)}{\Delta y} \right] \\ & - (\nu_y)_{i-1/2,j} \rho (A_{xz}^n)_{i-1/2,j} \left[\frac{(v_{i+1/2,j}^n - v_{i-1/2,j}^n)}{\Delta x} + \frac{(u_{i-1/2,j+1}^n - u_{i-1/2,j}^n)}{\Delta y} \right] \\ & + \frac{1}{2} \rho (A_{xy}^n)_{i,j} C_{D_x} u_{i+1/2,j}^{n+1} \sqrt{(u_{i+1/2,j}^n)^2 + (v_{i+1/2,j}^n)^2} \end{aligned} \quad (5.10)$$

where ν is horizontal turbulence eddy viscosity [L^2/s].

5.2.3 Pressure force

The net force due to hydrostatic pressure in the x direction over a small element of length Δx is given by

$$F_{x(\text{pressure})} = \int_{A_{yz}(x)} \rho g (\eta - z) dA - \int_{A_{yz}(x+\Delta x)} \rho g (\eta - z) dA$$

Writing the above for a uniform density fluid, we obtain

$$F_{x(\text{pressure})} = \rho g \left\{ \int_{A_{yz}(x)} \eta dA - \int_{A_{yz}(x+\Delta x)} \eta dA - \int_{A_{yz}(x)} z dA + \int_{A_{yz}(x+\Delta x)} z dA \right\}$$

As $\Delta x \rightarrow 0$, the above can be approximated as

$$F_{x(\text{pressure})} \approx -\Delta x \rho g A_{yz} \left\{ \frac{\partial \eta}{\partial x} - \frac{\partial z_c}{\partial x} \right\}$$

where z_c is the elevation of the centroid of the face A_{yz} (i.e., the elevation of the center of area). For the present purposes, we will confine ourselves to conditions where the free surface gradient dominates the centroid gradient so that, for the $i + 1/2$ face of a grid cell, a discrete form is

$$F_{x(\text{pressure})} \approx -\rho g A_{yz} (\eta_{i+1} - \eta_i)$$

Future studies should perhaps consider the effect of the centroid gradient on the hydrostatic pressure term. It is neglected herein as the centroid gradient can have reversals and discontinuities within the subgrid scale from the i to $i + 1$ cell centers, which is significantly more complex to discretize than the typically smooth free surface gradient.

An implicit linear discretization of the pressure term that is valid for $\Delta t \partial A_{yz} / \partial t \ll A_{yz}$ is

$$F_{x(\text{pressure})} = - \left[\rho g \eta_{i+1,j}^{n+1} (A_{yz}^n)_{i+1/2,j} - \rho g \eta_{i,j}^{n+1} (A_{yz}^n)_{i+1/2,j} \right] \quad (5.11)$$

The above follows the linearization introduced in [Casulli \(1999\)](#) whose second-order effects are discussed in [Hodges \(2004\)](#).

5.2.4 Momentum equation

Substituting Eqs/ (5.6), (5.10), and (5.11) into Eq. (5.2), the first-order up-wind discretization of the incompressible momentum equation is:

$$\begin{aligned}
& \rho V \frac{(u_{i+1/2,j}^{n+1} - u_{i+1/2,j}^n)}{\Delta t} \\
& + \rho u_{i+1/2,j}^n (A_{yz}^n)_{i+1/2,j} (u_{i+1/2,j}^n - u_{i-1/2,j}^n) \\
& + \rho v_{i+1/2,j}^n (A_{xz}^n)_{i+1/2,j} (u_{i+1/2,j}^n - u_{i+1/2,j-1}^n) \\
= & \\
& - [\rho g \eta_{i+1,j}^{n+1} (A_{yz}^n)_{i+1/2,j} - \rho g \eta_{i,j}^{n+1} (A_{yz}^n)_{i+1/2,j}] \\
& + 2 (\nu_x)_{i+1/2,j} \rho (A_{yz}^n)_{i+1/2,j} \frac{(u_{i+3/2,j}^n - u_{i+1/2,j}^n)}{\Delta x} \\
& - 2 (\nu_x)_{i-1/2,j} \rho (A_{yz}^n)_{i-1/2,j} \frac{(u_{i+1/2,j}^n - u_{i-1/2,j}^n)}{\Delta x} \\
& + (\nu_y)_{i+1/2,j} \rho (A_{xz}^n)_{i+1/2,j} \left[\frac{(v_{i+3/2,j}^n - v_{i+1/2,j}^n)}{\Delta x} + \frac{(u_{i+1/2,j+1}^n - u_{i+1/2,j}^n)}{\Delta y} \right] \\
& - (\nu_y)_{i-1/2,j} \rho (A_{xz}^n)_{i-1/2,j} \left[\frac{(v_{i+1/2,j}^n - v_{i-1/2,j}^n)}{\Delta x} + \frac{(u_{i-1/2,j+1}^n - u_{i-1/2,j}^n)}{\Delta y} \right] \\
& + \frac{1}{2} \rho (A_{xy}^n)_{i,j} C_{Dx} u_{i+1/2,j}^{n+1} \sqrt{(u_{i+1/2,j}^n)^2 + (v_{i+1/2,j}^n)^2}
\end{aligned}$$

Rearranging the equation above provides

$$\begin{aligned}
\frac{\rho V}{\Delta t} u_{i+1/2,j}^{n+1} &= \frac{\rho V}{\Delta t} u_{i+1/2,j}^n \\
&- \rho u_{i+1/2,j}^n (A_{yz}^n)_{i+1/2,j} (u_{i+1/2,j}^n - u_{i-1/2,j}^n) \\
&+ \rho v_{i+1/2,j}^n (A_{xz}^n)_{i+1/2,j} (u_{i+1/2,j}^n - u_{i+1/2,j-1}^n) \\
&- [\rho g \eta_{i+1,j}^{n+1} (A_{yz}^n)_{i+1/2,j} - \rho g \eta_{i,j}^{n+1} (A_{yz}^n)_{i+1/2,j}] \\
&+ 2 (\nu_x)_{i+1/2,j} \rho (A_{yz}^n)_{i+1/2,j} \frac{(u_{i+3/2,j}^n - u_{i+1/2,j}^n)}{\Delta x} \\
&- 2 (\nu_x)_{i-1/2,j} \rho (A_{yz}^n)_{i-1/2,j} \frac{(u_{i+1/2,j}^n - u_{i-1/2,j}^n)}{\Delta x} \\
&+ (\nu_y)_{i+1/2,j} \rho (A_{xz}^n)_{i+1/2,j} \left[\frac{(v_{i+3/2,j}^n - v_{i+1/2,j}^n)}{\Delta x} + \frac{(u_{i+1/2,j+1}^n - u_{i+1/2,j}^n)}{\Delta y} \right] \\
&- (\nu_y)_{i-1/2,j} \rho (A_{xz}^n)_{i-1/2,j} \left[\frac{(v_{i+1/2,j}^n - v_{i-1/2,j}^n)}{\Delta x} + \frac{(u_{i-1/2,j+1}^n - u_{i-1/2,j}^n)}{\Delta y} \right] \\
&+ \frac{1}{2} \rho (A_{xy}^n)_{i,j} C_{Dx} u_{i+1/2,j}^{n+1} \sqrt{(u_{i+1/2,j}^n)^2 + (v_{i+1/2,j}^n)^2}
\end{aligned}$$

For clarity, we define a nonlinear advection (N_x) term as

$$\begin{aligned}
N_x^n_{i+1/2,j} &= - u_{i+1/2,j}^n (A_{yz}^n)_{i+1/2,j} (u_{i+1/2,j}^n - u_{i-1/2,j}^n) \\
&+ v_{i+1/2,j}^n (A_{xz}^n)_{i+1/2,j} (u_{i+1/2,j}^n - u_{i+1/2,j-1}^n)
\end{aligned}$$

Similarly, the diffusive stress (e.g., D_{yx}) terms are

$$\begin{aligned}
D_{xx\ i+1/2,j}^n &= 2(\nu_x)_{i+1/2,j}(A_{yz}^n)_{i+1/2,j} \frac{(u_{i+3/2,j}^n - u_{i+1/2,j}^n)}{\Delta x} \\
&\quad - 2(\nu_x)_{i-1/2,j}(A_{yz}^n)_{i-1/2,j} \frac{(u_{i+1/2,j}^n - u_{i-1/2,j}^n)}{\Delta x} \\
D_{yx\ i+1/2,j}^n &= (\nu_y)_{i+1/2,j}(A_{xz}^n)_{i+1/2,j} \left[\frac{(v_{i+3/2,j}^n - v_{i+1/2,j}^n)}{\Delta x} + \frac{(u_{i+1/2,j+1}^n - u_{i+1/2,j}^n)}{\Delta y} \right] \\
&\quad - (\nu_y)_{i-1/2,j}(A_{xz}^n)_{i-1/2,j} \left[\frac{(v_{i+1/2,j}^n - v_{i-1/2,j}^n)}{\Delta x} + \frac{(u_{i-1/2,j+1}^n - u_{i-1/2,j}^n)}{\Delta y} \right]
\end{aligned}$$

and a bottom drag (B_x) term is

$$B_{x\ i+1/2,j}^n = \frac{(A_{xy}^n)_{i,j}}{2V_{i,j}^n} C_D \sqrt{(u_{i+1/2,j}^n)^2 + (v_{i+1/2,j}^n)^2}$$

Dividing both sides of the discrete momentum equation by $\rho V/\Delta t$ and using the above notation, the x momentum equation can be written as

$$\begin{aligned}
u_{i+1/2,j}^{n+1} - \Delta t B_{x\ i+1/2,j}^n u_{i+1/2,j}^{n+1} &= u_{i+1/2,j}^n - \frac{\Delta t}{V_{i,j}^n} N_{x\ i+1/2,j}^n \\
&\quad - \frac{g\Delta t}{V_{i,j}^n} [\eta_{i+1,j}^{n+1}(A_{yz}^n)_{i+1/2,j} - \eta_{i,j}^{n+1}(A_{yz}^n)_{i+1/2,j}] \\
&\quad + \frac{\Delta t}{V_{i,j}^n} D_{xx\ i+1/2,j}^n + \frac{\Delta t}{V_{i,j}^n} D_{yx\ i+1/2,j}^n \tag{5.12}
\end{aligned}$$

Further define

$$\begin{aligned}
I_{i+1/2,j}^n &\equiv \frac{1}{1 - \Delta t B_{x\ i+1/2,j}^n} \\
E_{x\ i+1/2,j}^n &\equiv I_{i+1/2,j}^n \left[u_{i+1/2,j}^n - \frac{\Delta t}{V_{i,j}^n} N_{x\ i+1/2,j}^n + \frac{\Delta t}{V_{i,j}^n} D_{xx\ i+1/2,j}^n + \frac{\Delta t}{V_{i,j}^n} D_{xy\ i+1/2,j}^n \right]
\end{aligned}$$

Then Eq. (5.12) is

$$u_{i+1/2,j}^{n+1} = E_{x\ i+1/2,j}^n - g\Delta t \frac{I_{i+1/2,j}^n}{V_{i,j}^n} (A_{yz}^n)_{i+1/2,j} (\eta_{i+1,j}^{n+1} - \eta_{i,j}^{n+1}) \tag{5.13}$$

5.2.5 Comparison with the prior momentum models

The new approach (as proposed above) directly considers subgrid geometry surface areas (e.g., A_{yz}) in discretizing resolved effects of subgrid surface forces. This approach can be contrasted with the methods of [Casulli \(2009\)](#) (developed in the context of wetting/drying algorithms) that used only the mean water depth on a face (i.e., the average of the subgrid contributed depths). For comparison purposes, [Appendix B](#) provides the first-order upwind discrete solution of a subgrid model applying the idea of [Casulli \(2009\)](#).

Another approach in the literature is that of [Volp et al. \(2013\)](#), who approximated the subgrid momentum using a quadtree approach ([Chapter 2](#)). The subgrid force model is discretized on a $\Delta x/2$ scale (i.e., the flow variability is limited to four subgrid domains in a resolved grid cell no matter how many fine grid cells are actually available within a resolved grid cell). The key difference between the [Volp et al. \(2013\)](#) approach and the present work is that they emphasized the variability of forces within a resolved grid cell (i.e., at the $\Delta x/2$ scale), whereas we emphasize the integrated subgrid forces around the resolved grid cell. That is, the [Volp et al. \(2013\)](#) approach uses the fine-grid data to improve the effective grid scale by a factor of 2, whereas our method adapts the traditional finite-volume approach using integrated surface values around the resolved cell but directly applies the subgrid approximations at whatever scale the subgrid data are available. It seems likely that combining the approaches could be useful, but such efforts are not within the scope of the present work.

In [Chapter 6](#), a free-surface solution of the subgrid model applying the idea

of Casulli (2009) is compared with the solution of the new subgrid momentum model evaluate the performance of the new momentum model. The approach of Volp et al. (2013) was not added to the existing Frehd code and remains an open issue for future consideration.

5.3 Model solution

5.3.1 Flow continuity with the edge fluxes

The flow continuity is constructed by applying the idea of Casulli (2009) (Chapter 2). Integrating fine-grid fluxes at the edges of a grid cell provides a strict flow continuity of the volume flux over the subgrid area at the faces of a grid cell. The incompressible flow continuity with the integrated net flux (Q) at the faces of a grid cell, Eq. (2.1) is discretized as:

$$\frac{(V_{i,j}^{n+1} - V_{i,j}^n)}{\Delta t} + \int_f dQ_{i,j}^{n+1/2} = 0 \quad (5.14)$$

With an algebraic approximation (see figures in upper panel of Figure 5.2), the volume change in the resolved grid cell i, j is a function of the changing surface elevation and surface area:

$$V_{i,j}^{n+1} - V_{i,j}^n \simeq (A_{xy}^{n+1})_{i,j} \eta_{i,j}^{n+1} - (A_{xy}^n)_{i,j} \eta_{i,j}^n \quad (5.15)$$

where $(A_{xy})_{i,j}$ is the surface flow area on the xy plane that does not include the emergent (dry) subgrid areas (see lower panel of Fig. 5.2).

With the net flow areas A_{yz} and A_{xz} at the xz and yz -planar faces of a grid

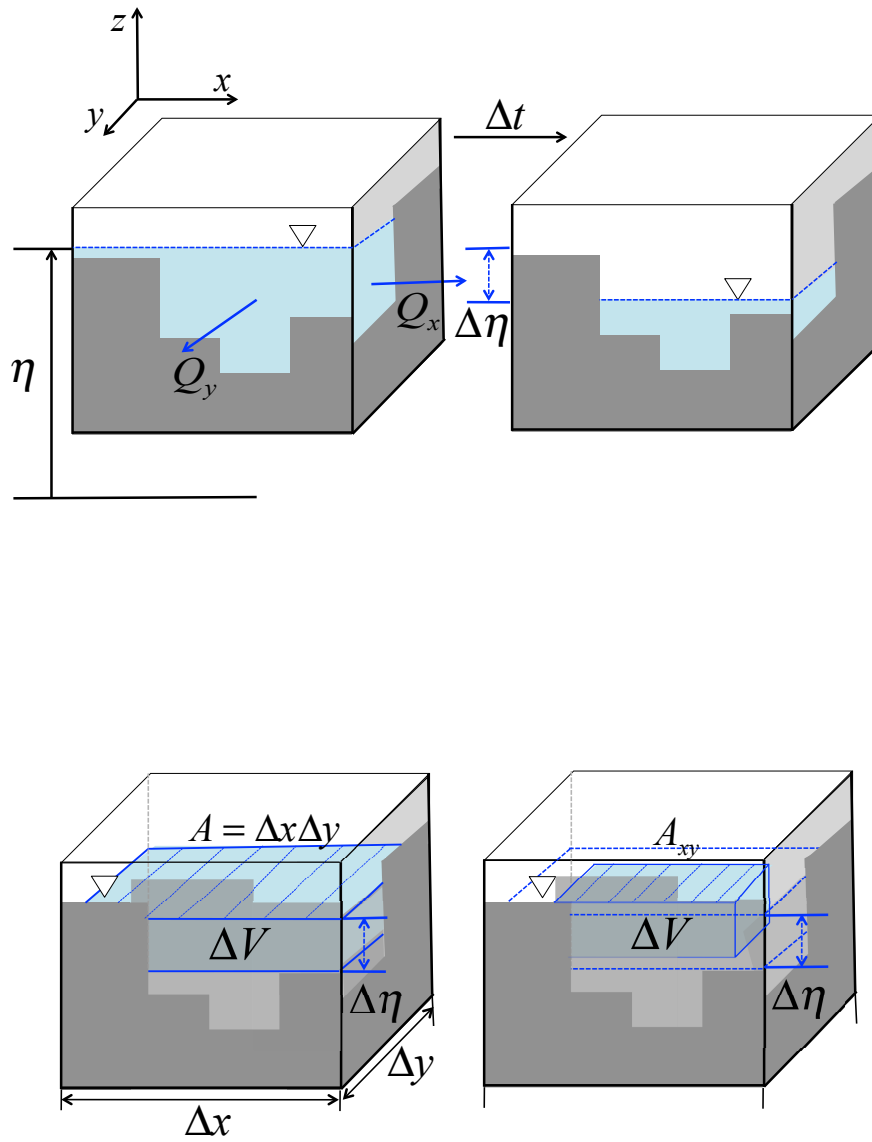


Figure 5.2: (top) Flow continuity with the net fluxes at the faces of a grid cell (Q_x , Q_y) and a difference of the surface elevation $\Delta\eta$ over Δt . (bottom) Volume change (ΔV) scaled with the surface area A (left) and with the effective surface area A_{xy} (right).

cell (see Figure 5.3), the net flux (dQ) is discretized as:

$$\int_f dQ_{i,j}^{n+1/2} = \left[u_{i+1/2,j}^{n+1/2} (A_{yz}^{n+1/2})_{i+1/2,j} - u_{i-1/2,j}^{n+1/2} (A_{yz}^{n+1/2})_{i-1/2,j} \right] \\ + \left[v_{i,j+1/2}^{n+1/2} (A_{xz}^{n+1/2})_{i,j+1/2} - v_{i,j-1/2}^{n+1/2} (A_{xz}^{n+1/2})_{i,j-1/2} \right] \quad (5.16)$$

In the above, the net flow areas A_{yz} and A_{xz} are unresolved topography areas with dashed borders in lower panel of Figure 5.3. Substituting Eqs. (5.16) and (5.15) into Eq. (5.14) provides

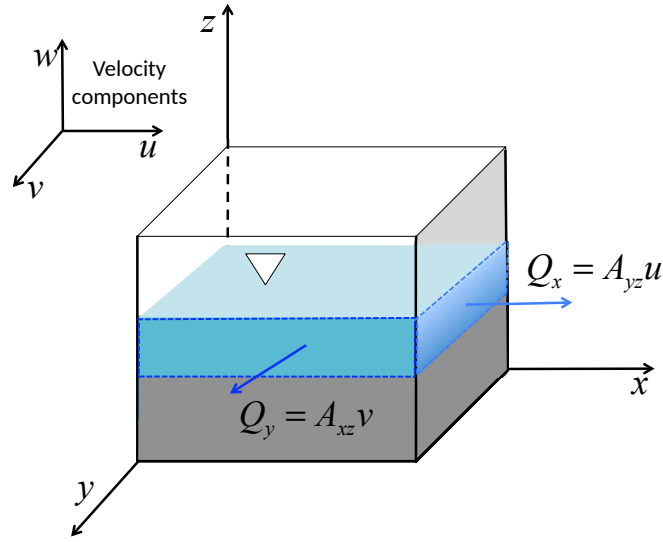
$$\frac{[(A_{xy}^{n+1})_{i,j} \eta_{i,j}^{n+1} - (A_{xy}^n)_{i,j} \eta_{i,j}^n]}{\Delta t} \\ + \left[u_{i+1/2,j}^{n+1/2} (A_{yz}^{n+1/2})_{i+1/2,j} - u_{i-1/2,j}^{n+1/2} (A_{yz}^{n+1/2})_{i-1/2,j} \right] \\ + \left[v_{i,j+1/2}^{n+1/2} (A_{xz}^{n+1/2})_{i,j+1/2} - v_{i,j-1/2}^{n+1/2} (A_{xz}^{n+1/2})_{i,j-1/2} \right] = 0 \quad (5.17)$$

In Appendix B, it is shown that the above can be represented as a standard θ -method for an semi-implicit free surface solution as:

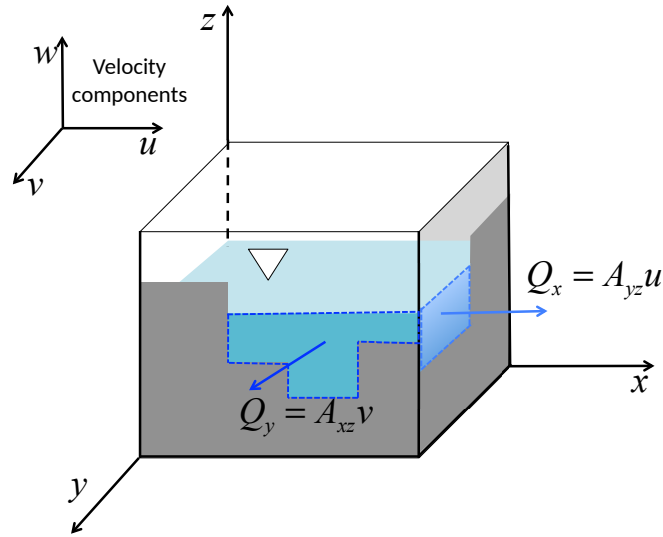
$$\eta_{i,j}^{n+1} + \theta_c \frac{\Delta t}{(A_{xy}^n)_{i,j}} \left[u_{i+1/2,j}^{n+1} (A_{yz}^n)_{i+1/2,j} - u_{i-1/2,j}^{n+1} (A_{yz}^n)_{i-1/2,j} \right] \\ + \theta_c \frac{\Delta t}{(A_{xy}^n)_{i,j}} \left[v_{i,j+1/2}^{n+1} (A_{xz}^n)_{i,j+1/2} - v_{i,j-1/2}^{n+1} (A_{xz}^n)_{i,j-1/2} \right] \\ = \eta_{i,j}^n - (1 - \theta_c) \frac{S_{i,j}^n}{(A_{xy}^n)_{i,j}} + \frac{\Delta t}{(A_{xy}^n)_{i,j}} T_{i,j}^{n+1/2} \quad (5.18)$$

where T represents external volume sources (inflows, precipitation), and the explicit source term (S) is defined as:

$$S_{i,j}^n \equiv \Delta t \left[u_{i+1/2,j}^n (A_{yz}^n)_{i+1/2,j} - u_{i-1/2,j}^n (A_{yz}^n)_{i-1/2,j} \right] \\ + \Delta t \left[v_{i,j+1/2}^n (A_{xz}^n)_{i,j+1/2} - v_{i,j-1/2}^n (A_{xz}^n)_{i,j-1/2} \right]$$



(a) Resolved topography



(b) Unresolved topography

Figure 5.3: Schematic diagram of a grid cell with resolved topography (top) and unresolved topography (bottom). The nomenclature, Q_x and Q_y denote x and y -directional fluxes on the faces of the cell (displayed with arrows); A_{xz} and A_{yz} denote the flow areas of the faces of the cell.

5.3.2 Free-surface elevation solution

The overall algorithm is completed by substituting discrete versions of momentum, Eq. (5.13) for u^{n+1} and v^{n+1} at the cell faces $i + 1/2$, $i - 1/2$, $j + 1/2$ and $j - 1/2$ into discrete continuity Eq. (5.18), which provides

$$\begin{aligned}
& \eta_{i,j}^{n+1} + \theta_c \frac{\Delta t}{(A_{xy}^n)_{i,j}} \left[E_{x \ i+1/2,j}^n (A_{yz}^n)_{i+1/2,j} - I_{i+1/2,j}^n \frac{g\Delta t}{V_{i,j}^n} (A_{yz}^n)_{i+1/2,j}^2 (\eta_{i+1,j}^{n+1} - \eta_{i,j}^{n+1}) \right] \\
& - \theta_c \frac{\Delta t}{(A_{xy}^n)_{i,j}} \left[E_{x \ i-1/2,j}^n (A_{yz}^n)_{i-1/2,j} - I_{i-1/2,j}^n \frac{g\Delta t}{V_{i,j}^n} (A_{yz}^n)_{i-1/2,j}^2 (\eta_{i,j}^{n+1} - \eta_{i-1,j}^{n+1}) \right] \\
& + \theta_c \frac{\Delta t}{(A_{xy}^n)_{i,j}} \left[E_{y \ i,j+1/2}^n (A_{xz}^n)_{i,j+1/2} - I_{i,j+1/2}^n \frac{g\Delta t}{V_{i,j}^n} (A_{xz}^n)_{i,j+1/2}^2 (\eta_{i,j+1}^{n+1} - \eta_{i,j}^{n+1}) \right] \\
& - \theta_c \frac{\Delta t}{(A_{xy}^n)_{i,j}} \left[E_{y \ i,j-1/2}^n (A_{xz}^n)_{i,j-1/2} - I_{i,j-1/2}^n \frac{g\Delta t}{V_{i,j}^n} (A_{xz}^n)_{i,j-1/2}^2 (\eta_{i,j}^{n+1} - \eta_{i,j-1}^{n+1}) \right] \\
& = \eta_{i,j}^n - (1 - \theta_c) \frac{S_{i,j}^n}{(A_{xy}^n)_{i,j}} + \frac{\Delta t}{(A_{xy}^n)_{i,j}} T_{i,j}^{n+1/2} \tag{5.19}
\end{aligned}$$

For simplicity in exposition, let

$$\begin{aligned}
C_{i+1/2,j}^n &\equiv \theta_c \frac{g(\Delta t)^2}{(A_{xy}^n)_{i,j} V_{i,j}^n} I_{i+1/2,j}^n (A_{yz}^n)_{i+1/2,j}^2 \\
C_{i-1/2,j}^n &\equiv \theta_c \frac{g(\Delta t)^2}{(A_{xy}^n)_{i,j} V_{i,j}^n} I_{i-1/2,j}^n (A_{yz}^n)_{i-1/2,j}^2 \\
C_{i,j+1/2}^n &\equiv \theta_c \frac{g(\Delta t)^2}{(A_{xy}^n)_{i,j} V_{i,j}^n} I_{i,j+1/2}^n (A_{xz}^n)_{i,j+1/2}^2 \\
C_{i,j-1/2}^n &\equiv \theta_c \frac{g(\Delta t)^2}{(A_{xy}^n)_{i,j} V_{i,j}^n} I_{i,j-1/2}^n (A_{xz}^n)_{i,j-1/2}^2
\end{aligned}$$

and

$$\begin{aligned}
G_{i,j}^n &\equiv \Delta t \left[E_{x \ i+1/2,j}^n (A_{yz}^n)_{i+1/2,j} - E_{x \ i-1/2,j}^n (A_{yz}^n)_{i-1/2,j} \right] \\
& + \Delta t \left[E_{y \ i,j+1/2}^n (A_{xz}^n)_{i,j+1/2} - E_{y \ i,j-1/2}^n (A_{xz}^n)_{i,j-1/2} \right]
\end{aligned}$$

Substituting G and C into Eq. 5.19, we have

$$\begin{aligned}
& \eta_{i,j}^{n+1} - C_{i+1/2,j}^n (\eta_{i+1,j}^{n+1} - \eta_{i,j}^{n+1}) + C_{i-1/2,j}^n (\eta_{i,j}^{n+1} - \eta_{i-1,j}^{n+1}) \\
& - C_{i,j+1/2}^n (\eta_{i,j+1}^{n+1} - \eta_{i,j}^{n+1}) + C_{i,j-1/2}^n (\eta_{i,j}^{n+1} - \eta_{i,j-1}^{n+1}) + \theta_c \frac{G_{i,j}^n}{(A_{xy}^n)_{i,j}} \\
& = \eta_{i,j}^n - (1 - \theta_c) \frac{S_{i,j}^n}{(A_{xy}^n)_{i,j}} + \frac{\Delta t}{(A_{xy}^n)_{i,j}} T_{i,j}^{n+1/2}
\end{aligned} \tag{5.20}$$

Rearranging Eq. (5.20) provides

$$\begin{aligned}
& \eta_{i,j}^{n+1} [1 + C_{i+1/2,j}^n + C_{i-1/2,j}^n + C_{i,j+1/2}^n + C_{i,j-1/2}^n] \\
& - \eta_{i+1,j}^{n+1} C_{i+1/2,j}^n - \eta_{i-1,j}^{n+1} C_{i-1/2,j}^n - \eta_{i,j+1}^{n+1} C_{i,j+1/2}^n - \eta_{i,j-1}^{n+1} C_{i,j-1/2}^n \\
& = \eta_{i,j}^n - (1 - \theta_c) \frac{S_{i,j}^n}{(A_{xy}^n)_{i,j}} + \frac{\Delta t}{(A_{xy}^n)_{i,j}} T_{i,j}^{n+1/2} - \theta_c \frac{G_{i,j}^n}{(A_{xy}^n)_{i,j}}
\end{aligned} \tag{5.21}$$

For the present work, we limit our focus to a Backwards Euler discretization, applying $\theta_c = 1$. Thus, Eq. (5.21) is reduced to:

$$\begin{aligned}
& \eta_{i,j}^{n+1} [1 + C_{i+1/2,j}^n + C_{i-1/2,j}^n + C_{i,j+1/2}^n + C_{i,j-1/2}^n] \\
& - \eta_{i+1,j}^{n+1} C_{i+1/2,j}^n - \eta_{i-1,j}^{n+1} C_{i-1/2,j}^n - \eta_{i,j+1}^{n+1} C_{i,j+1/2}^n - \eta_{i,j-1}^{n+1} C_{i,j-1/2}^n \\
& = \eta_{i,j}^n + \frac{\Delta t}{(A_{xy}^n)_{i,j}} T_{i,j}^{n+1/2} - \frac{G_{i,j}^n}{(A_{xy}^n)_{i,j}}
\end{aligned} \tag{5.22}$$

Note that in the formulation above the cell face values (e.g., A_{yz}) always appear in terms that (when products are broken down) have forms such as $A_{yz}V^{-1}$ or $A_{yz}A_{xy}^{-1}$. As a result, such terms will go to zero (rather than infinity) when a subgrid face is dry as long as some portion of the subgrid geometry remains wet. Thus, the only special handling for wetting and drying is the conventional approach used in Frehd (i.e., as $h_{i,j} \rightarrow 0$), which can be interpreted here as applying when $V_{i,j} \rightarrow 0$.

For a linear solution of η^{n+1} , the free-surface solution, Eq. (5.22) requires subgrid cross-sectional areas A_{xz} , A_{yz} , effective grid-cell surface area A_{xy} , and storage volume of a resolved grid cell V to be known at time n for elevation η^n in each grid cell. These are determined directly from the subgrid topography. Appendix C provides the equations computing subgrid geometric quantities. Figure 5.4 depicts the structure of computation nodes at a grid in the present approach.

In comparison to the original approach in Frehd discussed in Chapter 3, the new subgrid model considers how the cell storage volume varies nonlinearly with the surface elevation as well as the subgrid integrated surface forces at the cell faces. Calculating the continuous range of geometric values for any η can be computationally expensive, especially when the subgrid contains a large number of cells. To reduce this effort, we employ a “look-up table” scheme (Appendix D), which stores subgrid geometry values at pre-defined intervals of $\Delta\eta$ for each grid cell. The accuracy and time-efficiency of the subgrid model implemented with/without the look-up table scheme is compared in Chapter 6.

5.4 Subgrid topography sampling

One challenge for implementing subgrid topography effects into the resolved grid scale is in the potential for flow connectivity at water surface elevations below the model-resolved grid bottom elevation (see discussion in Section 1.1 and Fig. 1.5). That is, if the resolved grid represents the bottom elevation (Z_b) of a grid cell with

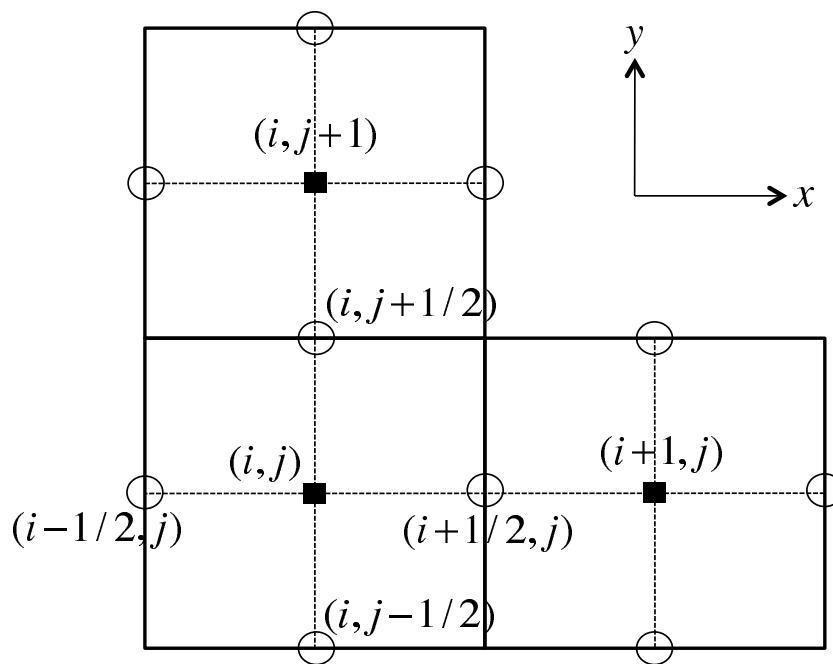


Figure 5.4: Computation nodes at a grid. Squares: free-surface elevation (η), depth (h), water volume (V), and surface flow area (A_{xy}); Circles: velocities (u, v), fluxes (Q), and face flow areas (A_{yz}, A_{xz})

a simple average of the subgrid elevations (z_b) over the $n_r \times n_s$ subgrid cells, e.g.,

$$Z_b \equiv \frac{1}{n_r n_s} \sum_{r=1}^{n_r} \sum_{s=1}^{n_s} z_b(r, s)$$

then there is a potential for a continuous path of subgrid cells r, s across the resolved grid cell such that $z_b(r, s) < Z_b$. Thus, flow is physically possible along the subgrid path, but is blocked at the resolved grid scale because the resolved grid cell is nominally “dry” (i.e., $\eta \leq Z_b$). Simple approaches to obtaining resolved bathymetry from subgrid topography cannot directly represent flow conveyance through subgrid flow passages where $\eta_{i,j} < Z_{b(i,j)}$, but a connected path of $z_b(r, s) < Z_b$ exists within the subgrid topography.

Although a full investigation of subgrid connectivity is beyond the scope of the present work, herein we experiment with using the minimum subgrid elevation to represent the resolved grid cell elevation, i.e.,

$$Z_b \equiv \min [z_b(r, s)] \quad : \quad r = \{1, 2, \dots, n_r\} \quad , \quad s = \{1, 2, \dots, n_s\}$$

Applying this bathymetry treatment requires reconsideration of the resolved grid cell depth within the subgrid method. The simplest approach to the resolved flow depth is the difference between the resolved free surface elevation and the resolved bottom, i.e., $h_{i,j}(t) = \eta_{i,j}(t) - Z_{b(i,j)}(t)$. However, when Z_b represents the minimum depth, this value for h is not a good representation of the effective flow depth at the resolved scale. Herein we use the average of subgrid depths ($\overline{h_{f(i,j)}}$) instead of the model-resolved depth.

$$\overline{h_{f(i,j)}}(t) \equiv \frac{1}{n_r n_s} \sum_{r=1}^{n_r} \sum_{s=1}^{n_s} h_f(r, s, t)$$

For computational convenience, the subgrid depth $h_f(r, s, t)$ is defined as:

$$h_f(r, s, t) = h(t) - \delta z(r, s, t)$$

where

$$\delta z(r, s, t) \equiv \min [z_b(r, s) - Z_b, h(t)]$$

As a subject for future study, there is an open question as to whether the simple average (used above) or a median value would provide a more effective approach. Herein we used the average based solely on computational efficiency.

Chapter 6

Validation and Verification of Subgrid Models

6.1 Introduction

This chapter presents descriptions of the simulation cases and the metrics used to evaluate subgrid model performance. Section 6.2 describes the numerical experiments, reference, and control cases for different subgrid model options. Section 6.3 describes the test section of the Nueces River Delta and the coarse resolution bathymetries used in the model testing. Section 6.4 describes the boundary conditions and other inputs to the models. In Section 6.5, the standard metrics for comparing models at different grid resolutions are presented and discussed. The results of the numerical experiments with the subgrid models (herein simply “experiments” for brevity) are compared to both reference cases and control cases and discussed in Chapter 6.6. Section 6.7 describes a new set of global indicators that we propose which can be used to evaluate time-varying subgrid model performance.

6.2 Numerical experiments, reference, and control cases

All modeling herein uses a portion of the complex marsh topography of the Nueces River Delta described in Appendix A. The reference cases use the Frehd model (Chapter 3) at 1×1 m grid resolution (see Section 6.3). The experiments and

the control cases use same portion of the Nueces River Delta, but coarsen the grid resolution to 15×15 m, which has proven a computationally tractable scale for modeling the entire Nueces River Delta (Ryan, 2011). The control cases use the Frehd model (Chapter 3) as the reference cases and averaging of static drag coefficients as the simplest approach for handling subgrid variability. Ideally, numerical models of natural systems should be validated directly from field data, but the frequency and spatial distribution of available observation data in complex topographical systems are generally insufficient for model validation. Herein we use model-model comparisons to validate new model features, which follows the precedent of prior researchers in subgrid algorithms (e.g., Wu et al., 2016; Volp et al., 2016).

A total of 8 model runs for a single scenario were conducted to test and validate the new algorithms (see Table 6.1). To identify the different model aspects in a particular run we use a series of letters, e.g., MDB, which can be parsed as follows. The fine-grid reference and the control are denoted as “F” and “C”, respectively. A “D” is used to denote experiments using the new drag model of Chapter 4. An “M” is used to denote experiments using the new momentum model of Chapter 5. Simulations using subgrid topography sampling (Section 5.4) are denoted with a “B.” An “L” is used to denote use of a look-up table for geometry values rather than direct computation (Appendix D). A “G” is used to denote experiments with the subgrid model approach that applies only the flux integration developed by Casulli (2009) and described in Appendix B. These “G” runs were designed to evaluate the improvements of the present approaches over the predecessor model.

For simplicity in naming, model runs use the same algorithms as the control

(C) case unless otherwise specified; e.g., a GL run uses the [Casulli \(2009\)](#) flux integration subgrid model with the Look-up table algorithm, but otherwise applies the same topography and drag treatment of the Control case. The new subgrid methods were tested both in combination (MDB) and separately (D and M) to better understand the effect of each model. Note that the look-up table (L) does not significantly effect the model results, but it does effect the computational performance. Thus, for clarity the L is only appended on model runs that are used for comparisons of performance with and without the look-up table. The expected performance of the topography sampling (B) for addressing the flow advection under the resolved grid cell bottom elevation requires parameterization of the subgrid topography on the face flow area.

Table 6.1: Run cases

| Run case | Model aspect | | |
|-----------------|--------------------------|----------------------|-----------------------------|
| | Subgrid Momentum (M) | Subgrid Drag (D) | Topography Sampling (B) |
| F (Reference) | X | X | X |
| C (Control) | X | X | X |
| G | X | X | X |
| M | O | X | X |
| D | X | O | X |
| MD | O | O | X |
| MB | O | X | O |
| MDB | O | O | O |

6.3 Test bathymetry

The reference model used the best available grid-scale bathymetry (1×1 m) of the Nueces Delta in the southern Texas (USA), which was compiled from lidar data by J. Gibeaut of Texas A&M Corpus Christi. We selected two test sections of 300×300 m that include the typical natural heterogeneity of the delta. To minimize numerical effects of edge boundary conditions, 300 m wide buffer domains were added around all edges of each test section. In effect, the test sections were centered in 900×900 m modeling domains developed from the lidar data. The fine resolution bathymetry for test sections A and B and their surrounding buffer domains are shown in Figures 6.1 and 6.2.

With the exception of B experiments using the subgrid topography sampling, the 15×15 m grid-scale bathymetry for the model experiments and control cases were obtained by the mean elevation of the fine-grid bathymetry within a coarse grid cell, Eq. (5.23). The *B* experiments used the minimum local elevation, Eq. (5.23) to examine small flow passage effects (Section 5.4).

6.4 Boundary conditions and model parameters

The model boundary conditions are artificial approximations of typical conditions in the Nueces Delta. Three of the boundaries were forced with simple linear, in-phase tidal oscillations, as indicated in Figure 6.3. The fourth boundary used a fixed inflow of $Q_{BC} = 10 \text{ m}^3/\text{s}$ distributed uniformly over the 900 m edge of the buffer domain. Frehd's approach to an inflow boundary is to distribute the flow proportionally with the local area. That is, given the depth $h_{edge,j}$ for $j = 1 \dots N_j$

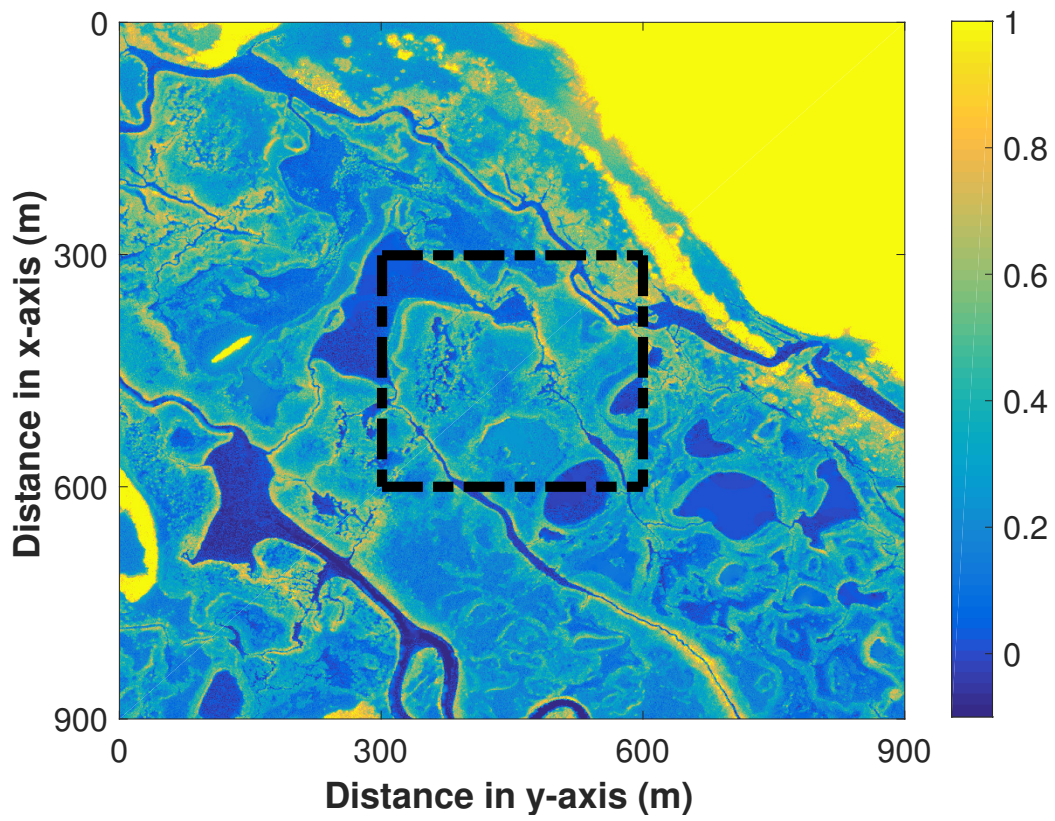


Figure 6.1: $1 \times 1\text{m}$ grid scale bathymetry of the test section A. The color scale is of the bottom elevation (m). Bold lines indicate the boundaries of the test section.

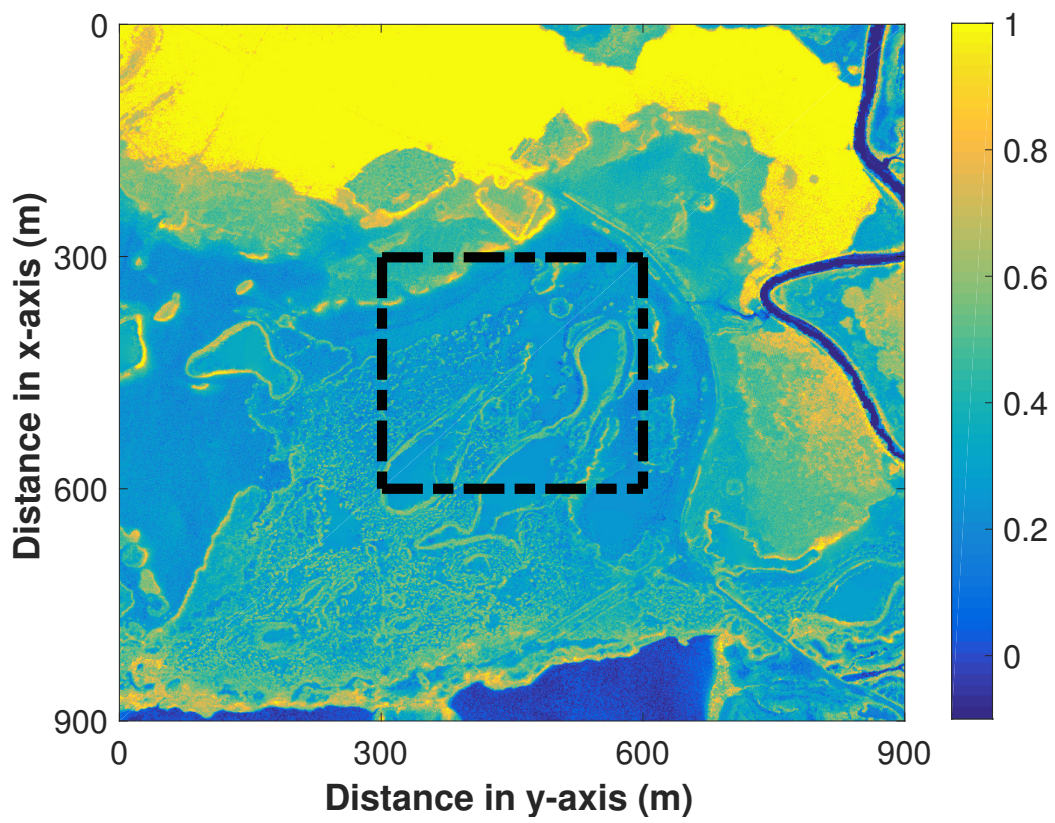


Figure 6.2: 1×1 m grid scale bathymetry of the test section B. The color scale is of the bottom elevation (m). Bold lines indicate the boundaries of the test section.

edge cells, the inflow $Q_{edge,j}$ at the j grid cell will be

$$Q_{edge,j} = Q_{BC} \frac{h_{edge,j}}{\sum_1^{N_j} h_{edge,j}}$$

Thus, the distribution of the flow across changes with time in response to the interior water levels of the simulation. Total model simulated time was 24 hours.

Although real-world conditions can be expected to have spatially-varying drag coefficients, for the present work we used a uniform drag coefficient (C_{Df}) of 0.01 across the entire fine-grid modeling domain. The coarse-grid control cases (C) and all non-D experiments use a simple spatial average for C_{Da} , so they also have uniform drag coefficients of 0.01. The D model experiments have dynamically-adjusting non-uniform coefficients computed by Eqs. (4.11) and (4.12). This approach enables us to examine the most simple form of the model behavior and compare with the effects of heterogeneity developed by the subgrid model.

The horizontal eddy viscosity was selected as 10^{-4} m²/s over the entire modeling domain. A small uniform value was chosen rather than invoking a more complex turbulence model so that the focus of the work remains on the performance of the subgrid model itself. A time step of 24 seconds was used for all the coarse grid experiments and control cases. The fine grid cases used a time step of 16 seconds. With these times steps the CFL conditions were typically 0.1 for the coarse grid runs and 0.5 for the fine grid runs.

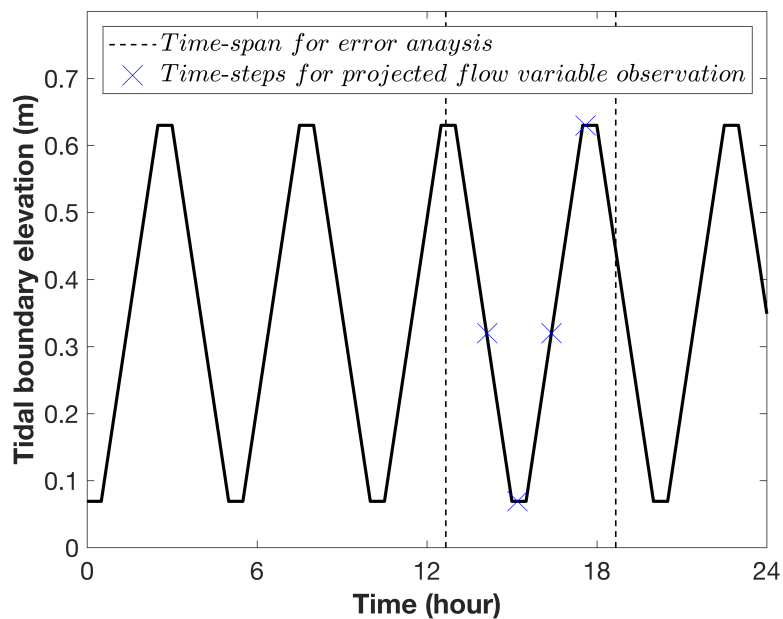
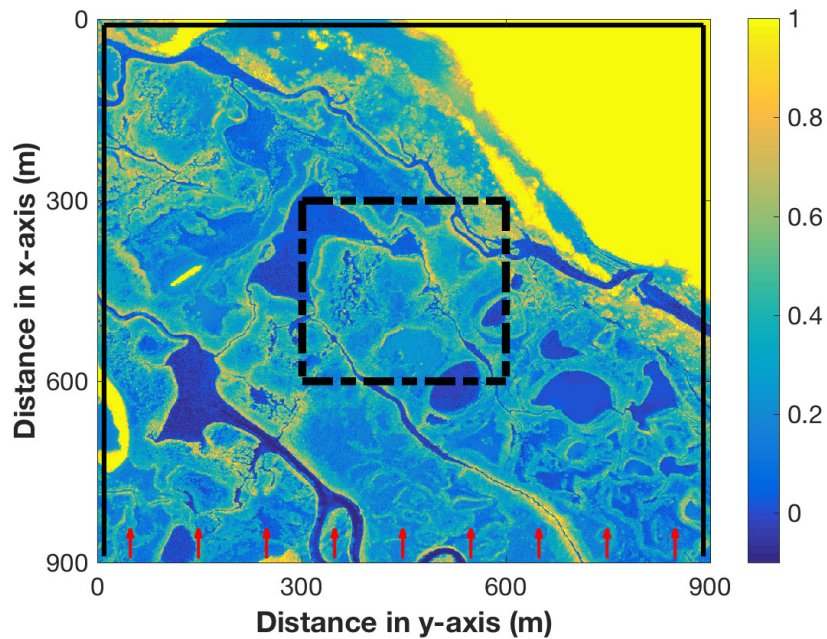


Figure 6.3: Boundary conditions for the numerical test. (top) Black lines: tidal boundaries, red arrows: inflow, and black dashed box: test section. (bottom) Black line: tidal boundary elevation, blue “X”s: time-steps of comparing projected flow variable, and black dashed lines: time-span of analyzing errors.

6.4.1 Evaluation time interval

To allow for spin-up of the oscillating flow driven by the tidal boundary conditions, the time interval for evaluating the metrics of Section 6.5 was from 12.67 hours to 18.67 hours, corresponding to the third tidal peak to the fourth tidal peak of the boundary conditions (see Fig. 6.3).

6.5 Standard statistical metrics

6.5.1 Projected flow variables

To compare the fine-grid simulations to the coarse-grid simulations requires the either downscaling the coarse-grid results to the fine grid, or upscaling the fine-grid results to the coarse grid. These are the “projected” variables. Herein we use downscaling for the water surface elevation (η) and upscaling for the fluxes. The downscaling is used for η as we seek to understand the error associated with accumulated water volume within a coarse grid cell that depends on the difference between η and the fine-grid bottom elevation. In contrast, the reference fluxes are upscaled from the fine grid to the coarse grid as our interest is whether the net fluxes in/out of a coarse grid cell are being adequately represented, whereas the local interchanges within the coarse-grid cell is of lesser import.

We use a simple uniform distribution downscaling, so that the value of $\eta_{i,j}$ for a cell i, j in the coarse-grid domain is applied to all the r, s subgrid elements in that cell. If we use X to represent the coarse-grid model nomenclature (e.g., MD as described above), then a downscaled η_X for coarse grid cell i, j can be formally

represented as η_{dX} , where

$$\eta_{dX}(r, s, t) \equiv \eta_X(t) \quad : \quad r \in \{1 : n_r\}, \quad s \in \{1 : n_s\}$$

The downscaled depth is the difference between the downscaled water surface elevation and the fine-grid bottom elevation, with negative depths set to zero:

$$h_{dX}(r, s, t) \equiv \max[(\eta_{dX}(r, s, t) - z_b(r, s)), 0] \quad (6.1)$$

The flow velocities at the edges of the reference grid cell (u_F and v_F) are upscaled by integrating along the faces to obtain the net coarse-grid flux, denoted as Q_{uF} , which is computed for the x and y directions as:

$$\begin{aligned} Q_{Fx}(r, s, t) &\equiv h_F(r, s, t) u_F(r, s, t) \\ Q_{Fy}(r, s, t) &\equiv h_F(r, s, t) v_F(r, s, t) \\ Q_{uFx}(t) &\equiv \sum_{s=1}^{n_s} Q_{Fx}(n_r, s, t) \Delta s \\ Q_{uFy}(t) &\equiv \sum_{r=1}^{n_r} Q_{Fy}(r, n_s, t) \Delta r \end{aligned} \quad (6.2)$$

where n_r and n_s are the numbers of fine-grid cells composing the fine-grid system for r and s -directions, and Δr and Δs are the unit lengths of the fine-grid coordinates. Fluxes at the resolved grid cell of the coarse-grid simulation method X are scaled with the flow velocities at the edges of the coarse-grid cell (u_X and v_X) as:

$$\begin{aligned} Q_{Xx}(t) &\equiv h_X(t) u_X(t) \Delta y \\ Q_{Xy}(t) &\equiv h_X(t) v_X(t) \Delta x \end{aligned} \quad (6.3)$$

where Δx and Δy are the unit lengths of a model-resolved grid cell for x and y -directions.

The time-varying spatial average of the free-surface elevations over the test region, $\overline{\eta_X}(t)$ can be determined as:

$$\overline{\eta_X}(t) \equiv \frac{1}{N_x N_y} \sum_{i=1}^{N_x} \sum_{j=1}^{N_y} \eta_X(i, j, t) \quad (6.4)$$

and for the reference model, $\overline{\eta_F}(t)$ is determined as:

$$\overline{\eta_F}(t) \equiv \frac{1}{N_x N_y} \sum_{i=1}^{N_x} \sum_{j=1}^{N_y} \left[\frac{1}{n_r n_s} \sum_{r=1}^{n_r} \sum_{s=1}^{n_s} \eta_F(r, s, t) \right]_{(i,j)} \quad (6.5)$$

where N_x and N_y are the numbers of model-resolved grid cells for x and y -directions over the test domain.

6.5.2 Standard comparison metrics

In the present work, two previously-defined error metrics, the ‘‘absolute mean error’’ ([Anderson and Bates, 2001](#)) and the ‘‘Willmott Skill Score’’ ([Willmott, 1981](#)) were applied to quantify time-space scales of discrepancies of the experiments and the control from the reference. The absolute mean error is selected as a more restrictive metric than a simple mean error. The latter was not chosen as it allows underprediction in one location (or time) to be offset by overprediction in another location (or time), hence producing a smaller error result for oscillating flows that does not reflect the actual performance of the models. In contrast to the absolute mean error, the Willmott Skill Score provides a normalized metric of errors across a time-space domain. To ensure that effects of boundary conditions and spin-up do not

dominate the error metrics, we use a limited space domain (i.e., the central portion of the domain, see Section 6.3) and a limited time span (i.e., beginning after spin up is completed) for computations (see Section 6.4.1).

For coarse-grid simulation method X , the relative error for subgrid element $\eta_{dX}(r, s, t)$ in coarse-grid cell i, j is denoted as $\delta\eta_{dX}$, and is scaled on the maximum subgrid depth over the coarse-grid cell.

$$\delta\eta_{dX}(r, s, t) \equiv \frac{\eta_{dX}(r, s, t) - \eta_F(r, s, t)}{\max[h_F(\alpha, \beta, t)]} \quad : \quad \alpha \in \{1 : n_r\} , \beta \in \{1 : n_s\} ,$$

$$\max[h_F(\alpha, \beta, t)] > \epsilon$$

With ϵ chosen as the depth tolerance (10^{-3} m), one order of magnitude larger than the depth tolerance used in the Frehd model to designated dry cells. This approach prevents nearly dry cells (i.e., 1 mm of water) from dominating the error metric. By use of the uniform distribution downscaling for η , the relative error of the depth (h) is identical to that of η .

The relative error of the coarse-grid flux for the coarse-grid simulation method X is denoted as δQ_{uX} , and is scaled on the maximum subgrid flux over the coarse-grid cell as:

$$\delta Q_{uX}(i, j, t) \equiv \frac{[(Q_{Xx}(i, j, t) - Q_{uFx}(i, j, t))^2 + (Q_{Xy}(i, j, t) - Q_{uFy}(i, j, t))^2]^{1/2}}{\max\left[\sqrt{Q_{Fx}^2(\alpha, \beta, t) + Q_{Fy}^2(\alpha, \beta, t)}\right]}$$

$$: \quad \alpha \in \{1 : n_r\} , \beta \in \{1 : n_s\} , \max\left[\{Q_{Fx}^2(\alpha, \beta, t) + Q_{Fy}^2(\alpha, \beta, t)\}^{1/2}\right] > 0$$

The condition, $\max\left[\{Q_{Fx}^2(\alpha, \beta, t) + Q_{Fy}^2(\alpha, \beta, t)\}^{1/2}\right] > 0$ prevents the denominator from going to zero in the case of zero fluxes.

The time-varying absolute mean error across all of space is simply the spatial-average of the absolute relative errors ($|\delta\eta_{dX}|$) across the test domain, denoted as $\overline{E_{X\eta}}(t)$:

$$\overline{E_{X\eta}}(t) \equiv \frac{1}{N_x N_y} \sum_{i=1}^{N_x} \sum_{j=1}^{N_y} \left[\frac{1}{n_r n_s} \sum_{r=1}^{n_r} \sum_{s=1}^{n_s} |\delta\eta_{dX}(r, s, t)| \right]_{(i,j)} \quad (6.6)$$

Similarly, the space-varying absolute mean error across all of time at coarse-grid cell i, j is $\overline{E_{Xt\eta}}(i, j)$ and computed as:

$$\overline{E_{Xt\eta}}(i, j) \equiv \frac{1}{N_t} \sum_{t=1}^{N_t} \left[\frac{1}{n_r n_s} \sum_{r=1}^{n_r} \sum_{s=1}^{n_s} |\delta\eta_{dX}(r, s, t)| \right]_{(i,j)} \quad (6.7)$$

The time-varying absolute mean error of the upscaled flux is:

$$\overline{E_{XQ}}(t) \equiv \frac{1}{N_x N_y} \sum_{i=1}^{N_x} \sum_{j=1}^{N_y} \delta Q_{uX}(i, j, t) \quad (6.8)$$

$$\overline{E_{XtQ}}(i, j) \equiv \frac{1}{N_t} \sum_{t=1}^{N_t} \delta Q_{uX}(i, j, t) \quad (6.9)$$

It follows that the absolute mean error across the solution time and space is

$$\overline{\overline{E_{X\theta}}} \equiv \frac{1}{N_t} \sum_{t=1}^{N_t} \overline{E_{X\theta}}(t) \quad : \quad \theta \in \{\eta, Q\} \quad (6.10)$$

The standard deviation of the time-varying spatial-averaged errors over time-scale $\sigma(E_{X\theta})$ ($\theta \in \{\eta, Q\}$) is:

$$\sigma(E_{X\eta})(t) \equiv \sqrt{\frac{1}{N_x N_y} \sum_{i=1}^{N_x} \sum_{j=1}^{N_y} \left[\frac{1}{n_r n_s} \sum_{r=1}^{n_r} \sum_{s=1}^{n_s} (\delta\eta_{dX}(r, s, t) - \overline{E_{X\eta}}(t))^2 \right]_{(i,j)}} \quad (6.11)$$

$$\sigma(E_{XQ})(t) \equiv \sqrt{\frac{1}{N_x N_y} \sum_{i=1}^{N_x} \sum_{j=1}^{N_y} (\delta Q_{uX}(i, j, t) - \overline{E_{XQ}}(t))^2} \quad (6.12)$$

The above error metrics are such that smaller values indicate better model performance, and are used to provide insight into the model behavior in Section 6.6

The Willmott Skill Score has been used for assessing model fidelity over a non-dimensional range from 0 to 1 with higher values indicating better results (e.g., Kärnä et al., 2015; Liu et al., 2009). The Willmott Skill Score is typically applied for comparison of modeling results and observation data, but the methodology can be readily modified for a comparison to the reference model results. Let $\overline{W}(t)$ denote the Willmott Skill Score for the X experiment (e.g., MB) or control case (C) at time t . The time-varying metric of the X experiment for η over the spatial domain is

$$\overline{W}_{X\eta}(t) \equiv 1 - \frac{\sum_{i=1}^{N_x} \sum_{j=1}^{N_y} [\sum_{r=1}^{n_r} \sum_{s=1}^{n_s} (\eta_{dX}(r, s, t) - \eta_F(r, s, t))^2]_{(i,j)}}{\sum_{i=1}^{N_x} \sum_{j=1}^{N_y} [\sum_{r=1}^{n_r} \sum_{s=1}^{n_s} (|\eta_{dX}(r, s, t) - \overline{\eta_F}(t)| + |\eta_F(r, s, t) - \overline{\eta_F}(t)|)^2]_{(i,j)}} \quad (6.13)$$

Let

$$Q_X(i, j, t) \equiv \sqrt{Q_{Xx}^2(i, j, t) + Q_{Xy}^2(i, j, t)}$$

$$Q_{uF}(i, j, t) \equiv \sqrt{Q_{uFx}^2(i, j, t) + Q_{uFy}^2(i, j, t)}$$

and the spatial average flux over time for the reference model ($\overline{Q_F}(t)$) is:

$$\overline{Q_F}(t) \equiv \frac{1}{N_x N_y} \sum_{i=1}^{N_x} \sum_{j=1}^{N_y} \sqrt{Q_{uFx}^2(i, j, t) + Q_{uFy}^2(i, j, t)}$$

It follows that the metric for the upscaled flux over the spatial domain is as:

$$\overline{W}_{XQ}(t) \equiv 1 - \frac{\sum_{i=1}^{N_x} \sum_{j=1}^{N_y} [Q_X(i, j, t) - Q_{uF}(i, j, t)]^2}{\sum_{i=1}^{N_x} \sum_{j=1}^{N_y} [|Q_X(i, j, t) - \overline{Q_F}(t)| + |Q_{uF}(i, j, t) - \overline{Q_F}(t)|]^2} \quad (6.14)$$

As the Willmott Skill Score is always positive, it is reasonable to take an average of the time-varying score as a measure of the overall model skill:

$$\overline{\overline{W_{X\theta}}} \equiv \frac{1}{N_t} \sum_{t=1}^{N_t} \overline{W_{X\theta}}(t) \quad : \quad \theta \in \{\eta, Q\} \quad (6.15)$$

The average metric over time-space domain above considers the relative scale of error over time-varying spatial-averaged error. Values of $\overline{W_X}(t)$ and $\overline{\overline{W_X}}$ closer to one indicate model experiments or control cases that are closer to the reference case. To provide insight into the variability of the model skill, the standard deviation of $\overline{W_{X\theta}}(t)$ ($\theta \in \{Q, \eta\}$) can be computed as:

$$\sigma(W_{X\theta}) \equiv \sqrt{\frac{1}{N_t} \sum_{t=1}^{N_t} (\overline{W_{X\theta}}(t) - \overline{\overline{W_{X\theta}}})^2} \quad (6.16)$$

where a smaller value of $\sigma(W_{X\theta})$ indicates smaller variability in model fidelity over the time-space domain.

6.5.3 Time fraction metric

The purpose of using a subgrid model at a coarse grid resolution rather than directly solving a fine-grid model is to allow a larger domain to be computed with reduced computational costs. Thus, the computational performance of the subgrid model is of interest. Let t_X and t_F represent the computational time for the X experiment and the fine-grid reference case for identical initial and boundary conditions. A time-fraction metric can be defined as:

$$T_X \equiv \frac{t_X}{t_F} \quad (6.17)$$

where a smaller value indicates better performance of the subgrid model.

6.6 Test results and discussion

6.6.1 Overview

The new models were examined through error metric analysis in Section 6.6.2 and observation of projected flow variables in Section 6.6.3. In Section 6.6.4, performances of various model aspects are discussed. Computational costs of the subgrid models and the effectiveness of the look-up table (L) simulations are evaluated in Section 6.6.5.

6.6.2 Comparison of error metrics

An analysis of error metrics verifies that the combined model using the new methods (MDB) was effective in reducing the discrepancy between the coarse-grid and fine-grid solutions across the time-space domain in the test cases. The MDB case was quantitatively more effective than both the G case with the Casulli (2009) approach or the Control case (C). Tables 6.2 and 6.3 compare the time-space average error metrics across the experiments and control in the test sections A and B: for the absolute mean error \overline{E} , from Eq. (6.10), see Table 6.2; and for the Willmott Skill Score \overline{W} , from Eq. (6.15), see Table 6.3. The Willmott Skill Score close to one indicates model experiments that are closer to the reference, while the absolute mean error close to zero indicates a good agreement with the reference.

The absolute mean error for η of the MDB run was 67% (Section A) and 74% (Section B) lower than the C simulation. The corresponding Q errors for MDB were also 8% (Section A) and 22% (Section B) lower. In comparison with the G simulations, the MDB reduced the η error by 22% and 35% for Sections A and B,

respectively, with the Q error similarly reduced by 56% and 5%.

Table 6.2: Absolute mean errors

| Run case | \overline{E}_η | | \overline{E}_Q | |
|----------|---------------------|-----------|------------------|-----------|
| | Section A | Section B | Section A | Section B |
| C | 0.1173 | 0.1368 | 0.4471 | 0.4938 |
| G | 0.0517 | 0.0565 | 1.0607 | 0.8804 |
| MDB | 0.0403 | 0.0365 | 0.4436 | 0.3834 |

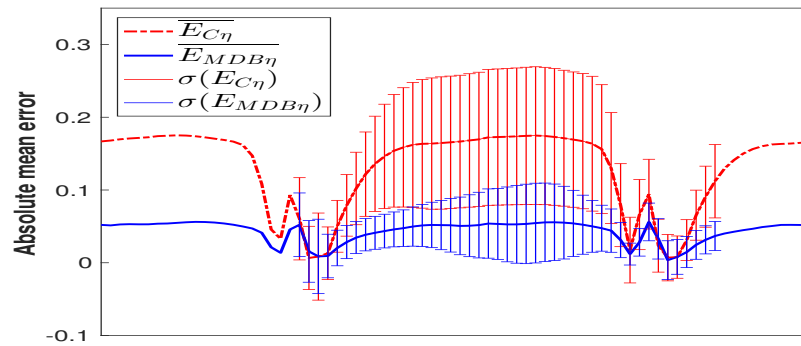
The Willmott Skill Score metric (Table 6.3) shows minor improvements with the MDB model, i.e., 4% and 10% increases for η skill compared to C, and 4% increase for Q . More importantly is that the time-variability of the skill (represented by σ) is significantly lower for the MDB simulations. Again, the MDB outperforms the G simulations in both the value of the Willmott Skill Score and reduced variability over time.

Table 6.3: Average and standard deviation of the Willmott Skill Score

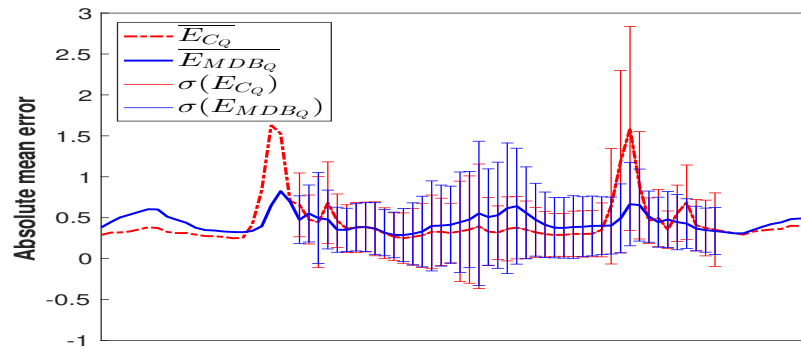
| Run case | \overline{W}_η | $\sigma(W_\eta)$ | \overline{W}_η | $\sigma(W_\eta)$ | \overline{W}_Q | $\sigma(W_Q)$ | \overline{W}_Q | $\sigma(W_Q)$ |
|----------|---------------------|------------------|---------------------|------------------|------------------|---------------|------------------|---------------|
| | Section A | | Section B | | Section A | | Section B | |
| C | 0.9536 | 0.0323 | 0.9052 | 0.0617 | 0.7228 | 0.1087 | 0.6409 | 0.1615 |
| G | 0.9906 | 0.0072 | 0.9770 | 0.0289 | 0.3577 | 0.1089 | 0.4186 | 0.1490 |
| MDB | 0.9943 | 0.0035 | 0.9927 | 0.0056 | 0.7535 | 0.0700 | 0.6718 | 0.1077 |

The improvements in the MDB run can also be seen in the time-evolution of the error metrics and their variability, as shown in Figures 6.4 and 6.5 for tests in Section A, and Figures 6.6 and 6.7 for Section B.

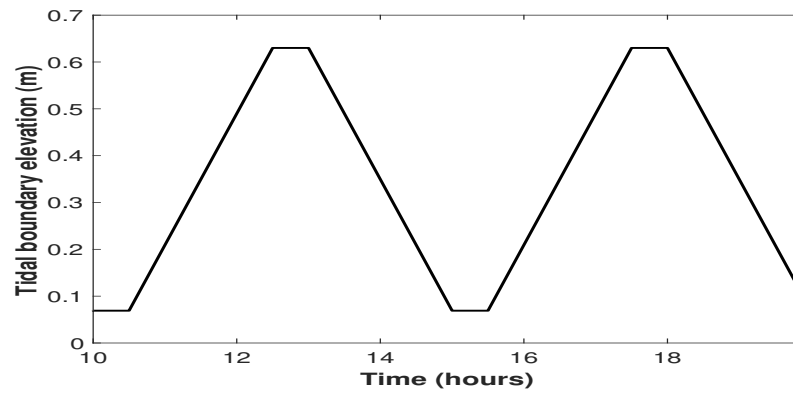
The scales of the error metrics vary over time with the time-varying tidal boundary elevation (η_t). The time-evolution of the absolute mean error for η over



(a) \overline{E}_η

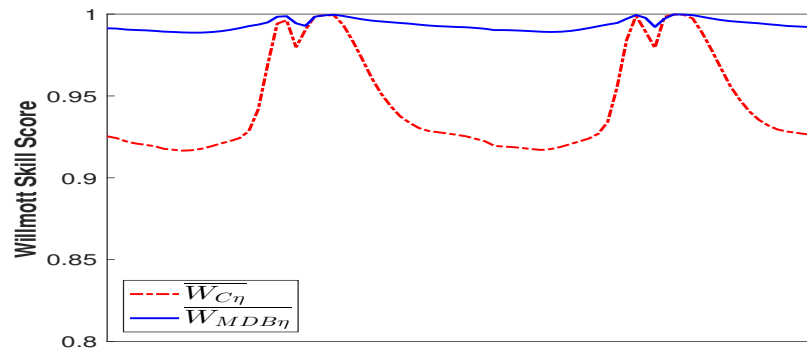


(b) \overline{E}_Q

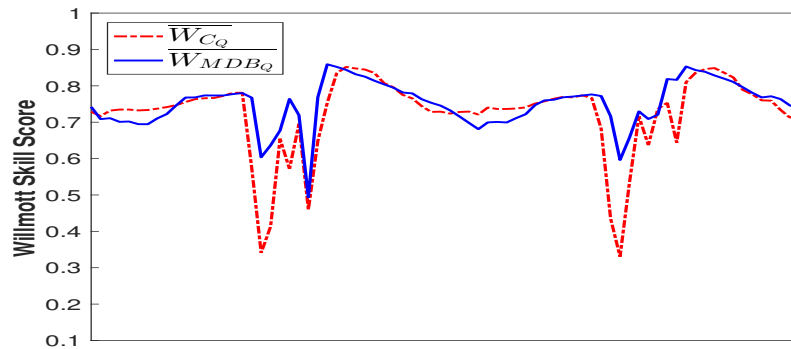


(c) η_t

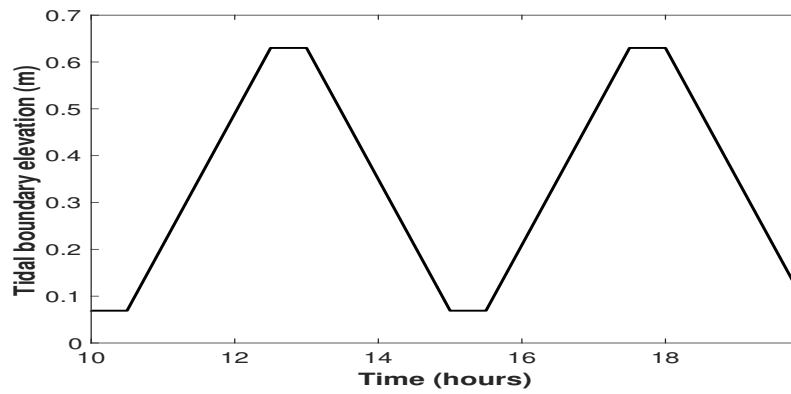
Figure 6.4: Absolute mean errors of the *MDB* experiment and control in the test section A



(a) \overline{W}_η

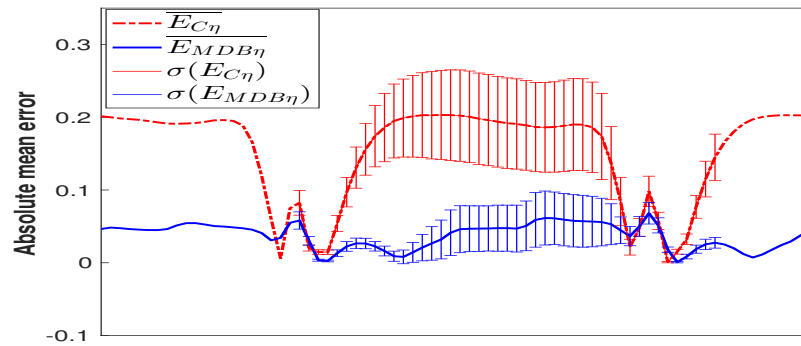


(b) \overline{W}_Q

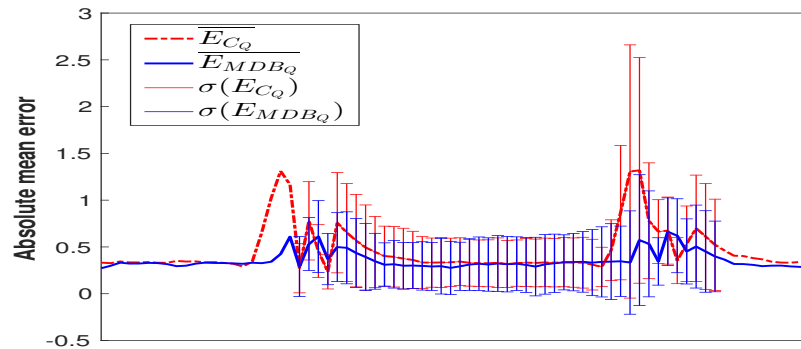


(c) η_t

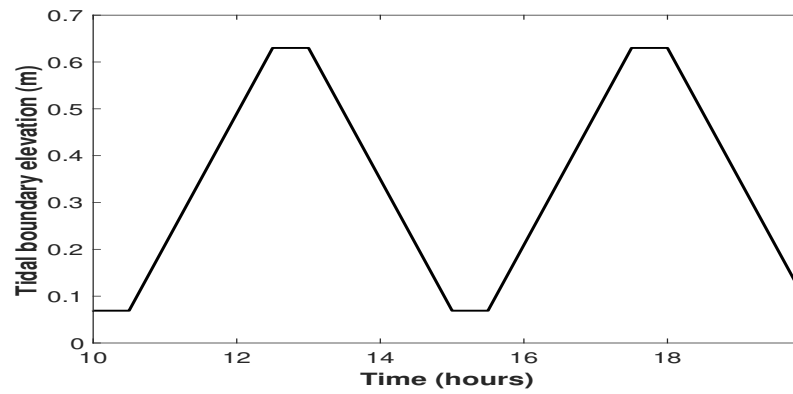
Figure 6.5: Willmott Skill Scores of the *MDB* experiment and control in the test section A



(a) \overline{E}_η

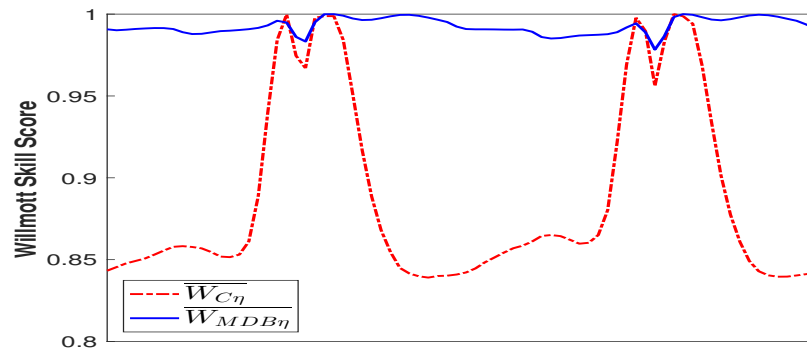


(b) \overline{E}_Q

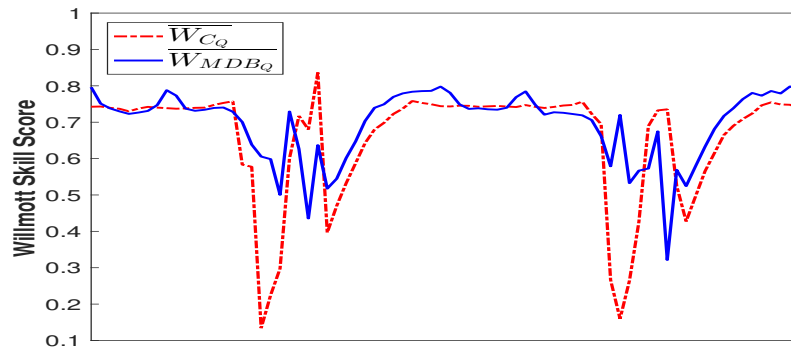


(c) η_t

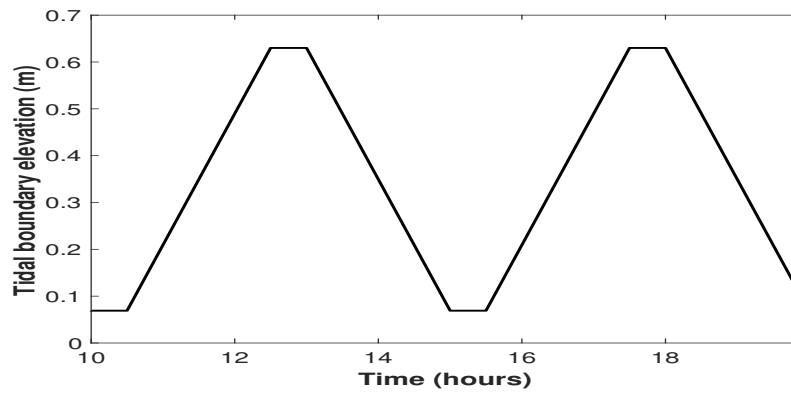
Figure 6.6: Absolute mean errors of the *MDB* experiment and control in the test section B



(a) $\overline{W_\eta}$



(b) $\overline{W_Q}$



(c) η_t

Figure 6.7: Willmott Skill Scores of the *MDB* experiment and control in the test section B

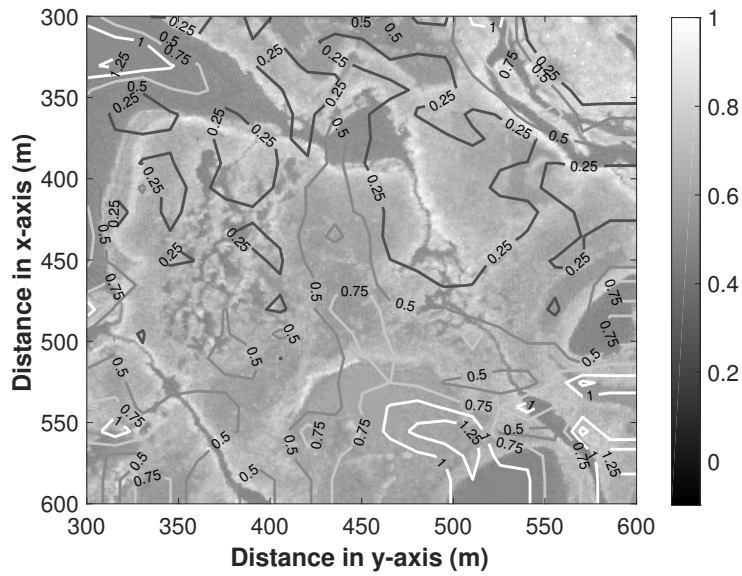
the test domain, $\overline{E_\eta}$ along with its standard deviation $\sigma(E_\eta)$ is overall less than 0.1 for the MDB case over all the range of η_t , which is about a half of that of the C case (upper row in Figs. 6.4 and 6.6). The Willmott Skill Score support this analysis as the score for η was close to unity throughout the MDB run (upper row of Figs. 6.5 and 6.7).

For flux (Q) on the coarse-grid scale, the MDB also reduced the discrepancies from the reference, but the results are not significantly different than the C case. However, there does appear to be a consistent reduction in the variability in the Willmott Skill Score for Q . Of particular performance is the behavior at high tide. When the tidal elevation reaches close to its highest elevation ($\eta_t \rightarrow 0.63$ m), $\overline{E_Q}(t)$ and $\sigma(E_Q)(t)$ of the MDB case are smaller than those of the C (middle panels of Figs. 6.4 and 6.6), but in the other range of η_t , the error metrics of MDB are similar to case C. The Willmott Skill Score $\overline{W}(t)$ shows a similar trend with tide (middle panels of Figs. 6.5 and 6.7). These results indicate the importance of the dynamic adjustments with tidal elevation that are part of the MDB methods.

Figures 6.8 and 6.9 show the spatial distribution of absolute mean errors Eqs. (6.7) and (6.9) in the MDB run. The numbers marked with the contour lines indicate the absolute mean errors for projected free-surface elevation and flowrate ($\overline{E_{Xt\eta}}$ and $\overline{E_{XtQ}}$) in the test regions A and B, respectively.

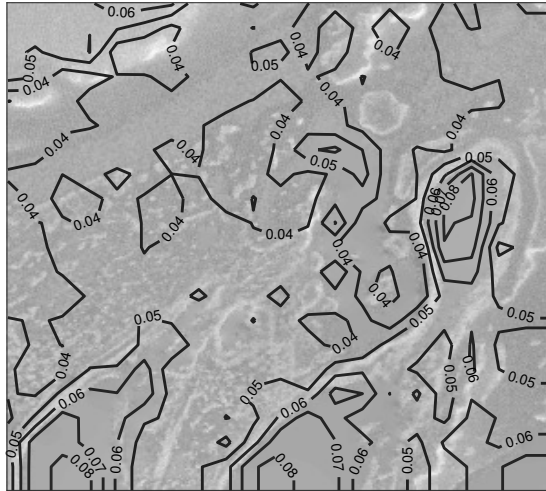


(a) $\overline{E_{Xt\eta}}$

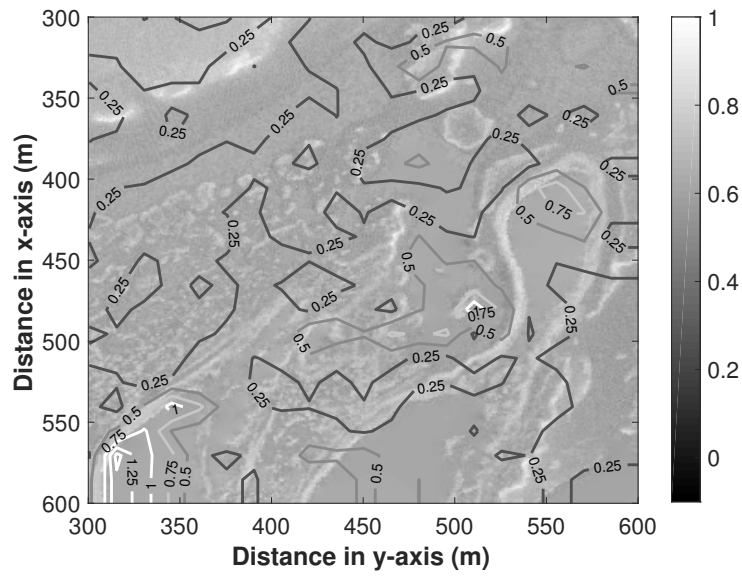


(b) $\overline{E_{XtQ}}$

Figure 6.8: Spatial distribution of absolute mean errors in the test region A



(a) $\overline{E_{Xt\eta}}$



(b) $\overline{E_{XtQ}}$

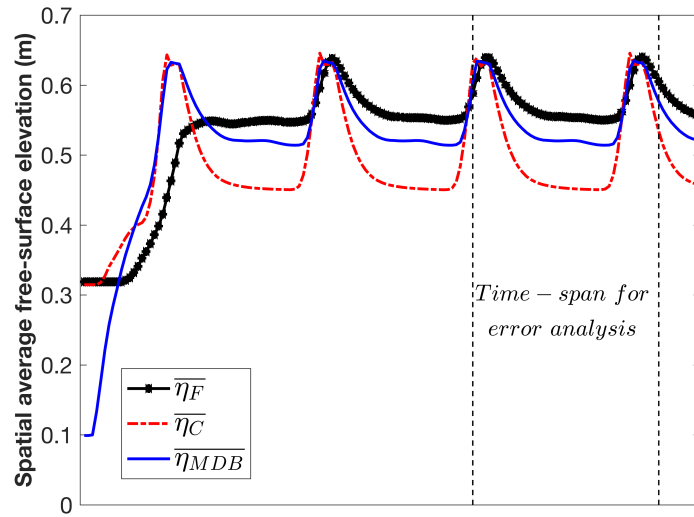
Figure 6.9: Spatial distribution of absolute mean errors in the test region B

6.6.3 Behaviors of projected flow variables

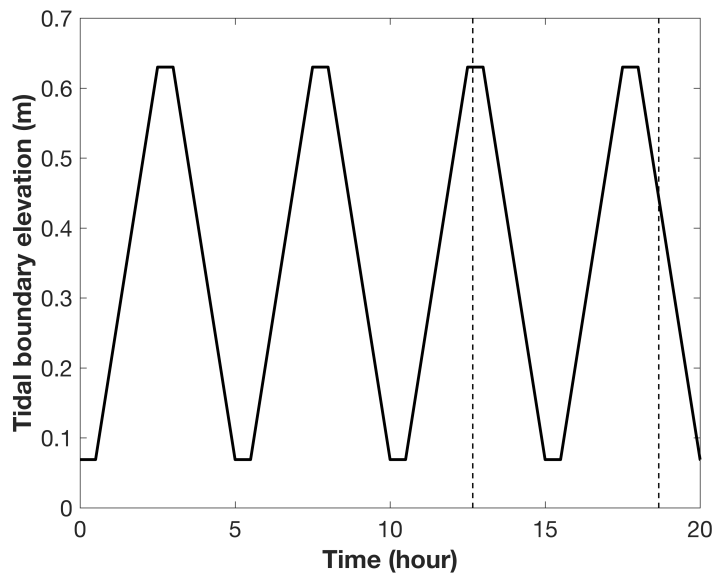
Comparisons of projected flow variables indicate that the MDB simulations are a better match for the F (fine-grid reference) case than the C (control) case. In particular, the MDB captures horizontally-deflected flow routes affected by subgrid topographic variations that cannot be seen in the C case. The flow variables compared between MDB, C, and F cases are (i) spatial-average free-surface elevation over time, $\bar{\eta}(t)$, Eqs. (6.4) and (6.5); (ii) spatial distribution of directional fluxes on the coarse-grid scale, Q_{ux} and Q_{uy} , Eqs. (6.2) and (6.3), (iii) spatial scales of flow depths on the fine-grid scale, h_d , Eq. (6.1), and (iv) spatial distribution of the drag coefficients. The spatial distribution of directional fluxes, flow depths, and drag coefficients were investigated at different tidal elevations: $\eta_t = 0.07$ m ($t = 15.2$ hours), 0.32 m (14.1 and 16.4 hours), and 0.63 m (17.6 hours). To investigate the effect of a change of the tidal elevation on a rise or drop, the variables were compared at two different time-steps ($t = 14.1$ hours and 16.4 hours) while η_t was 0.32 m at both cases.

The spatial-average free-surface elevation over time $\bar{\eta}(t)$ of the MDB run is observed to be better matched with $\bar{\eta}(t)$ of the reference, compared with that of the control. These effects can be seen in Figures 6.10 and 6.11, which compare $\bar{\eta}(t)$ of the MDB run (blue line), C (red dashed line) and F (black bold line) in the test sections A and B, respectively. The difference between $\bar{\eta}(t)$ in MDB and F increases at low tidal elevations ($\eta_t = 0.07$ m, 15.2 hours), but remains smaller than that difference between C and F indicating that MDB is performing better than C. The larger differences between F and both the MDB and C cases at low tidal levels (compared to high tide levels) likely indicates the effect of subgrid small channels. The control

(C) uses the average bottom elevation that misses these channels whereas the MDB uses of the minimum subgrid elevation that (at least partially) represents subgrid channels.

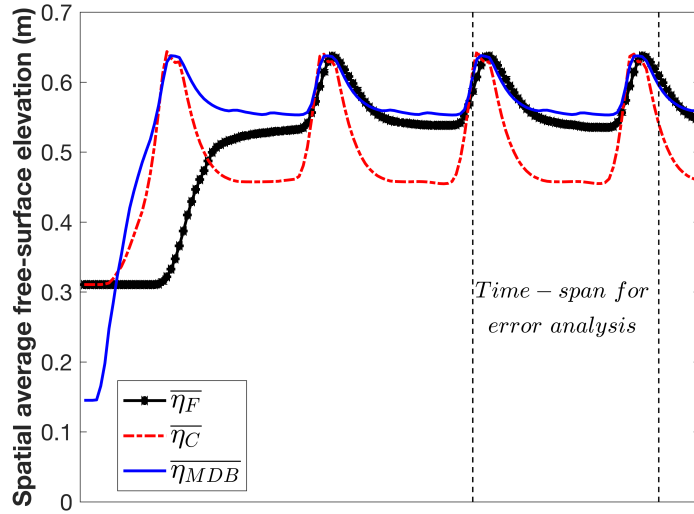


(a) Spatial average free-surface elevation ($\bar{\eta}$)

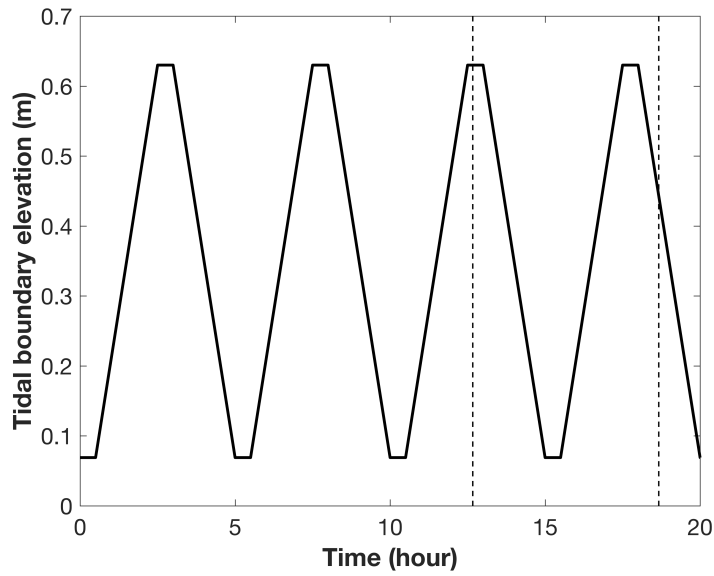


(b) Tidal boundary elevation (η_t)

Figure 6.10: Spatial average free-surface elevation of the *MDB* experiment and control in the test section A



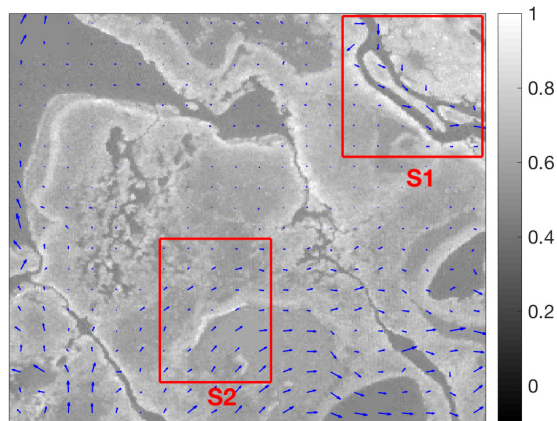
(a) Spatial average free-surface elevation ($\bar{\eta}$)



(b) Tidal boundary elevation (η_t)

Figure 6.11: Spatial average free-surface elevation of the *MDB* experiment and control in the test section B

Flow deflection can be caused by subgrid topography that is higher than represented by the mean bottom elevation in a grid cell. Such deflections can cause convoluted flow paths, thereby dissipating more energy in actual flow dynamics. Both the MDB and F cases show deflected flows around submerged topographic obstructions at the high tidal elevation, but similar deflections are not apparent in C cases. Figures 6.12 through 6.15 depict flux distribution at different tidal stages over the spatial domain for the reference (F) case, MDB experiment, and control (C) case over test section A. The blue arrows indicate the magnitude and direction of flux vectors on the resolved coarse-grid cell. In these figures, an area with narrow channels is identified as S1 and an area with an embankment is identified as S2. Neither MDB nor C simulations were able to capture the flows in the narrow channels of S1, which indicates that future work should include a focus on the problem of poorly-resolved channels. At low tidal elevations (Fig. 6.12 through 6.14) the MDB and C perform similarly in the S2 region and do not show substantial pattern differences from the F case. However, at higher tidal elevations (Fig. 6.15), the F case shows a flow deflection in the S2 area that is clearly represented in the MDB case and entirely missing in C. These results are consistent with the previous error analyses, that showed the MDB performed significantly better for Q than the C case at higher tidal elevations, but had similar variability at lower tides.



Reference

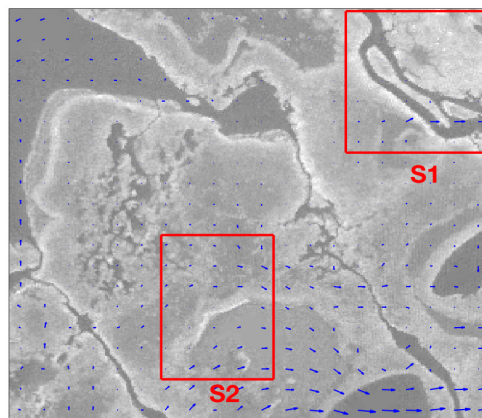
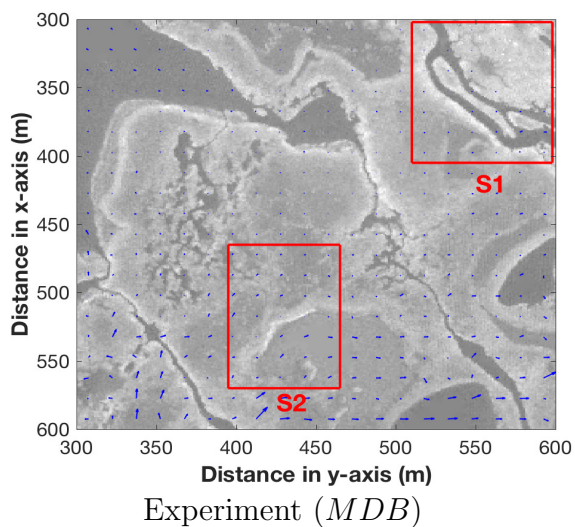
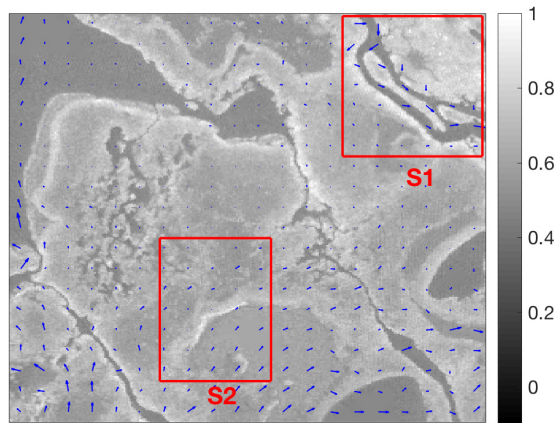
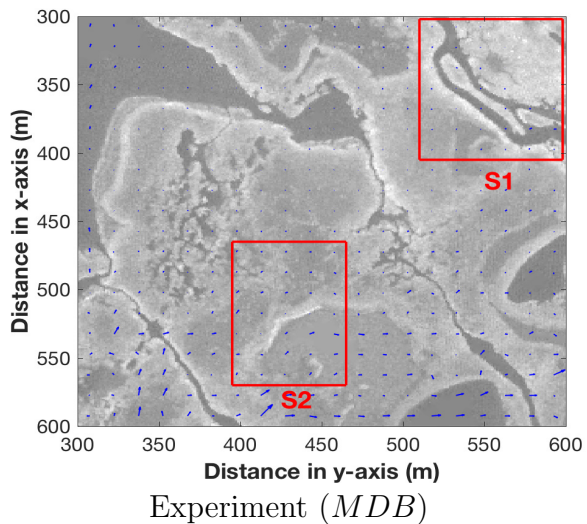


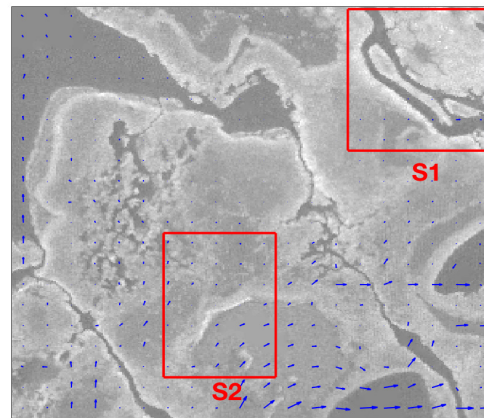
Figure 6.12: Fluxes projected in the test section A at $\eta_t = 0.32$ m ($t = 14.1$ hours). The grey scale is of the bottom elevation (m). A blue arrow indicates a flux vector on the resolved coarse-grid cell (m^3/s).



Reference

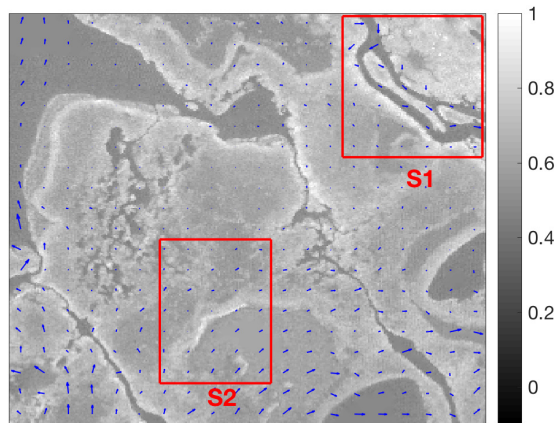


Experiment (*MDB*)



Control

Figure 6.13: Fluxes projected in the test section A at $\eta_t = 0.07$ m ($t = 15.2$ hours). The grey scale is of the bottom elevation (m). A blue arrow indicates a flux vector on the resolved coarse-grid cell (m^3/s).



Reference

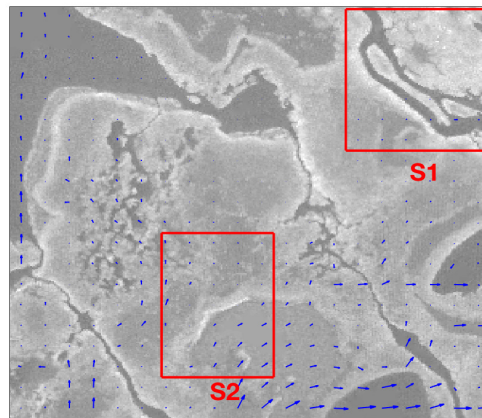
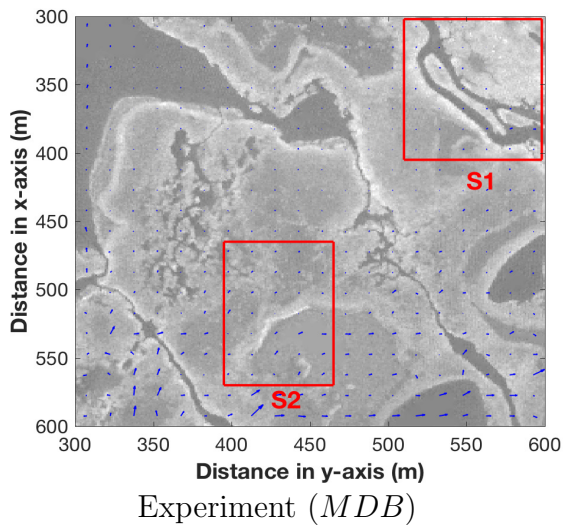
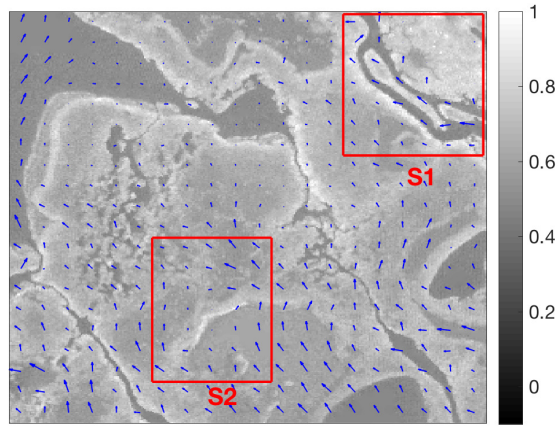


Figure 6.14: Fluxes projected in the test section A at $\eta_t = 0.32$ m ($t = 16.4$ hours). The grey scale is of the bottom elevation (m). A blue arrow indicates a flux vector on the resolved coarse-grid cell (m^3/s).



Reference

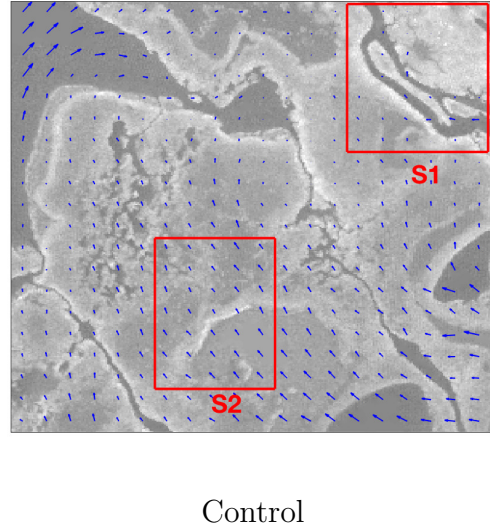
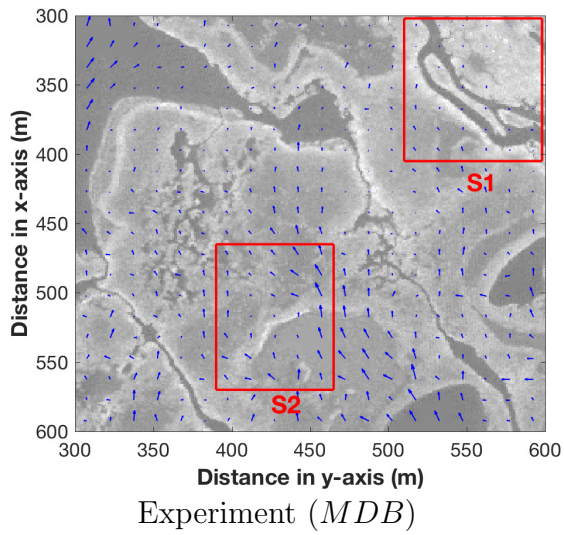
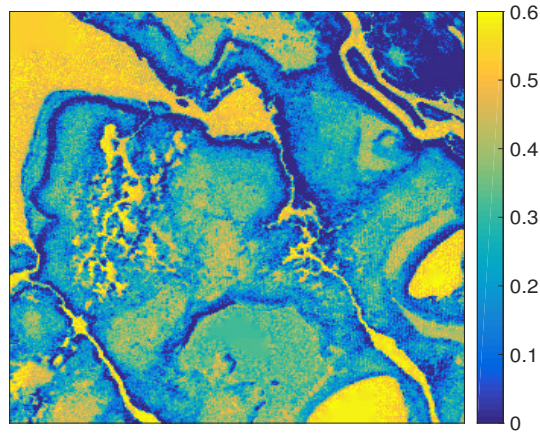
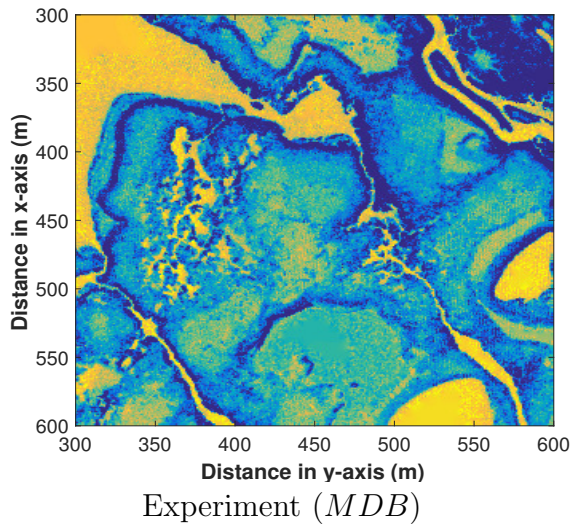


Figure 6.15: Fluxes projected in the test section A at $\eta_t = 0.63$ m ($t = 17.6$ hours). The grey scale is of the bottom elevation (m). A blue arrow indicates a flux vector on the resolved coarse-grid cell (m^3/s).

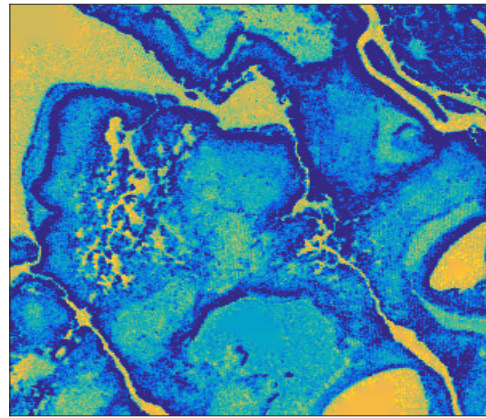
The spatial distribution of flow depths can be visually compared for several tidal conditions in Figs. 6.16 through 6.23. In general the MDB is a better match for the F case than is C over all the range tidal conditions in both test sections. Compared with the flow depths of F, those of the C were typically shallower (darker tint) at the low tidal levels, (Figs. 6.16 through 6.18 and 6.20 through 6.22), which agrees with the prior error analyses of the spatially-average free-surface elevation. At the high tidal level in section A, Figs. 6.19, the C depths were typically deeper (brighter tint), with the highland areas marked with “H1” showing the C has water in areas that are essentially dry in both F and MDB. However, in section B the high-tide differences between MDB and F are not visually obvious, as indicated by Fig. 6.23. Thus, the performance of the subgrid model is closely linked to the variability in the bathymetry.



Reference

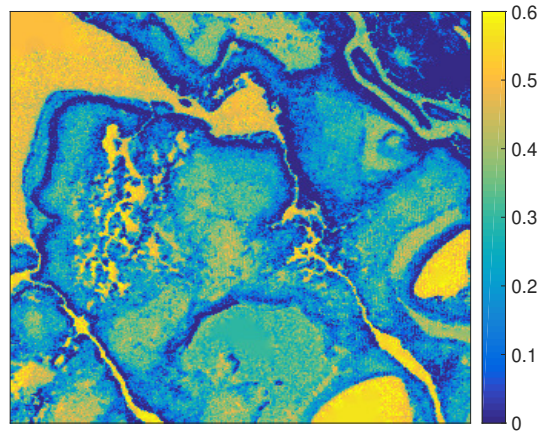


Experiment (*MDB*)

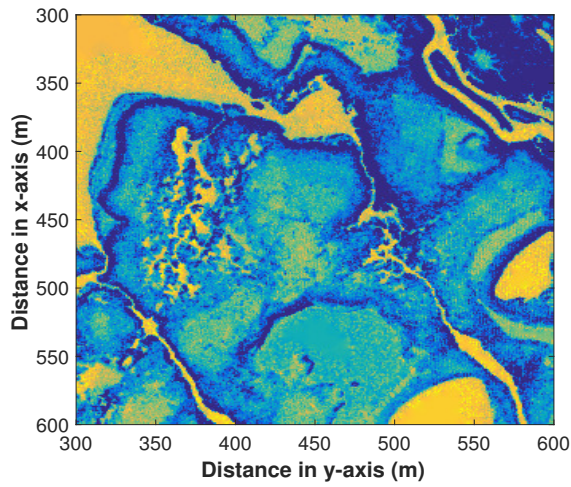


Control

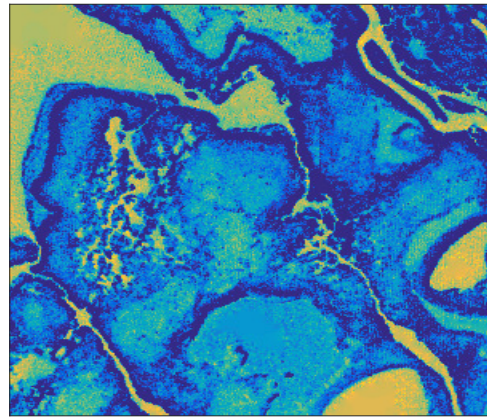
Figure 6.16: Flow depths on the fine-grid scale projected in the test section A at $\eta_t = 0.32$ m ($t = 14.1$ hours). The color scale is of the depth (m)



Reference

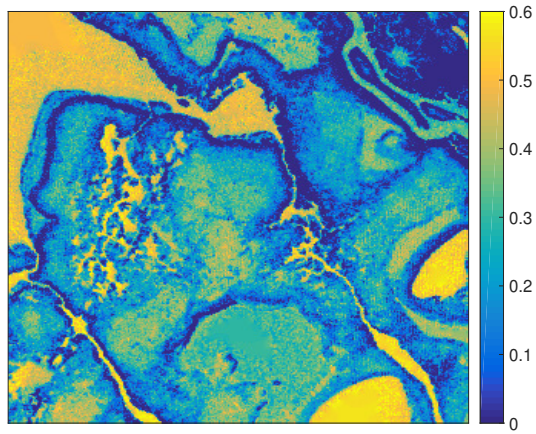


Experiment (*MDB*)



Control

Figure 6.17: Flow depths on the fine-grid scale projected in the test section A at $\eta_t = 0.07$ m ($t = 15.2$ hours). The color scale is of the depth (m)



Reference

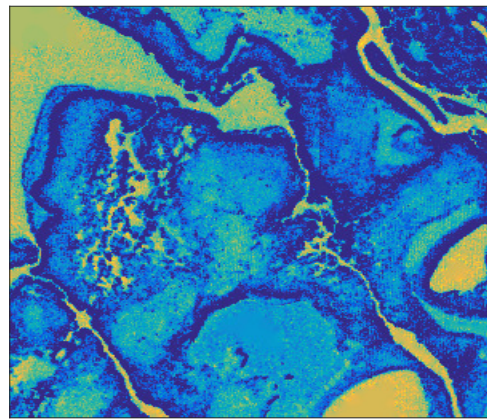
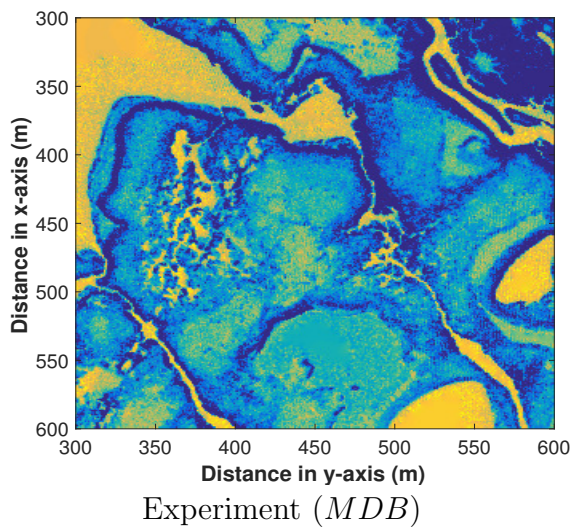
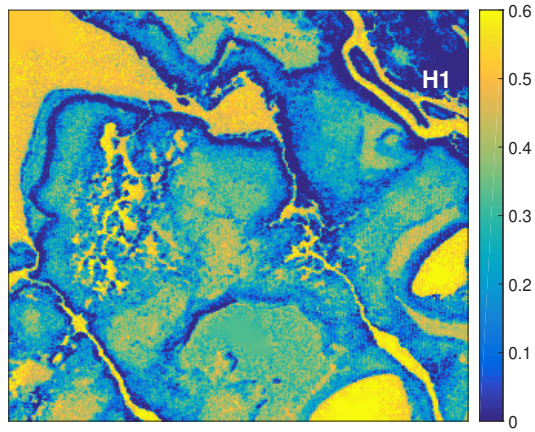
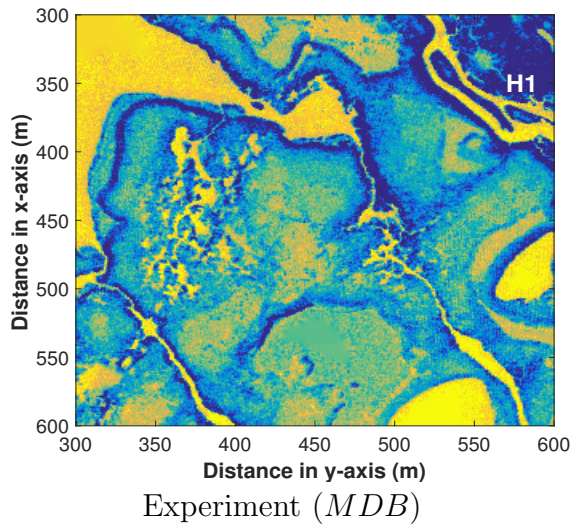


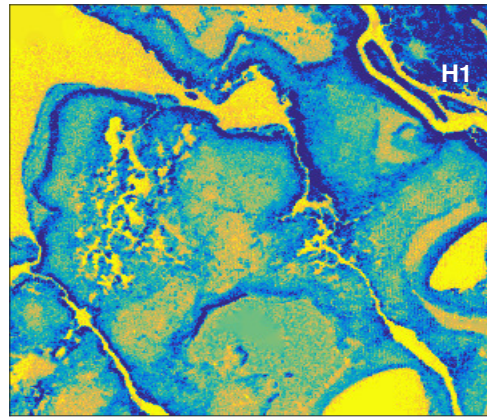
Figure 6.18: Flow depths on the fine-grid scale projected in the test section A at $\eta_t = 0.32$ m ($t = 16.4$ hours). The color scale is of the depth (m)



Reference

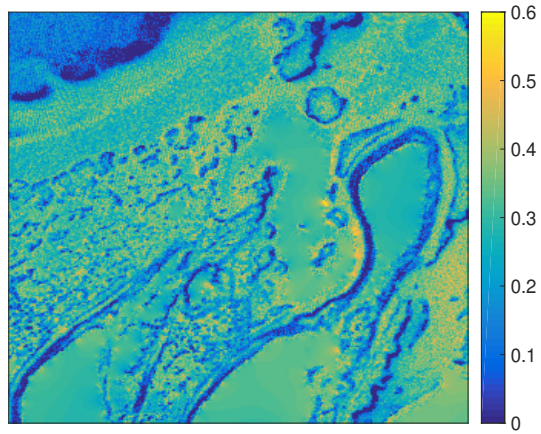


Experiment (*MDB*)

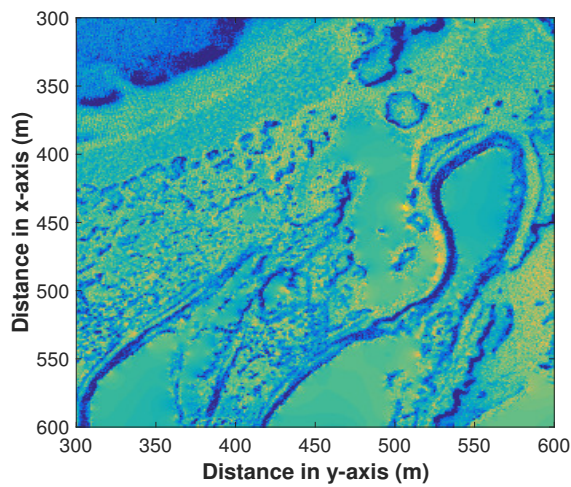


Control

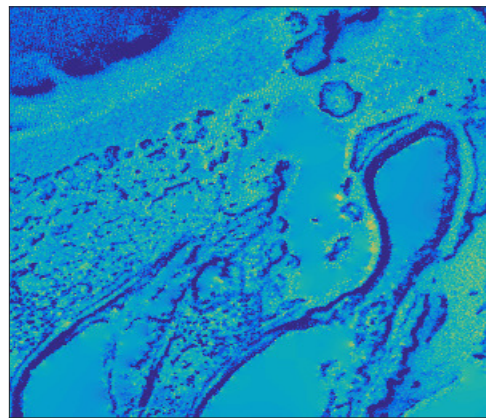
Figure 6.19: Flow depths on the fine-grid scale projected in the test section A at $\eta_t = 0.63$ m ($t = 17.6$ hours). The color scale is of the depth (m)



Reference

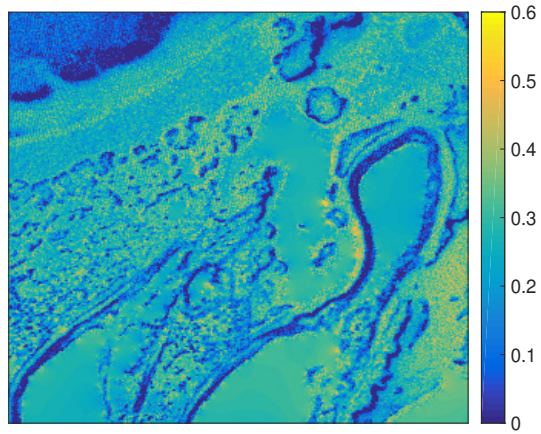


Experiment (*MDB*)

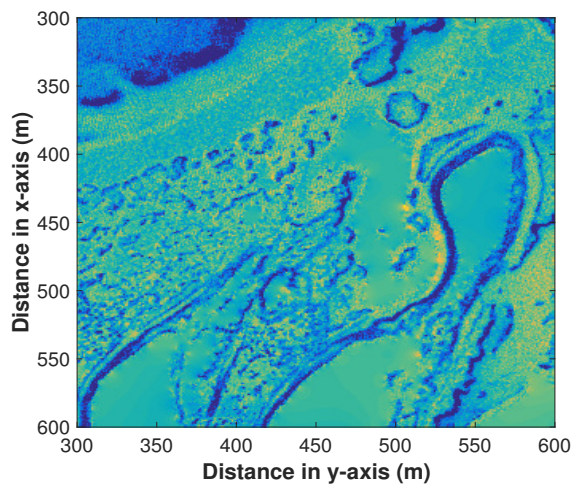


Control

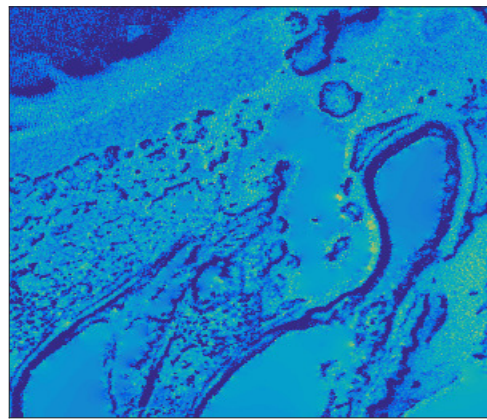
Figure 6.20: Flow depths on the fine-grid scale projected in the test section B at $\eta_t = 0.32$ m ($t = 14.1$ hours). The color scale is of the depth (m)



Reference

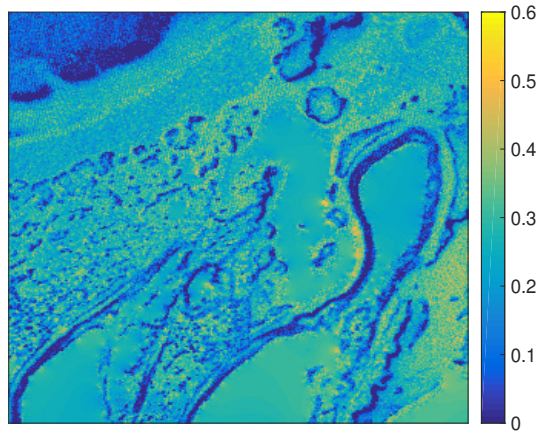


Experiment (*MDB*)

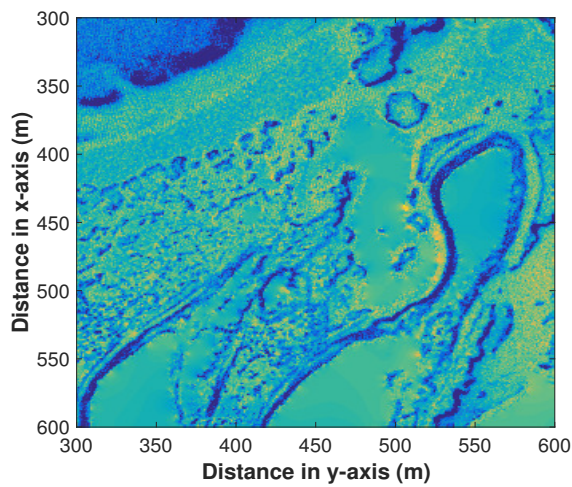


Control

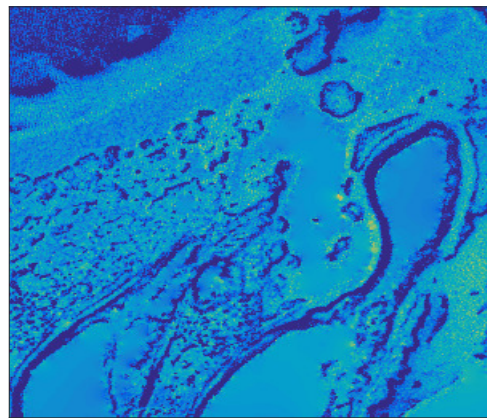
Figure 6.21: Flow depths on the fine-grid scale projected in the test section B at $\eta_t = 0.07$ m ($t = 15.2$ hours). The color scale is of the depth (m)



Reference

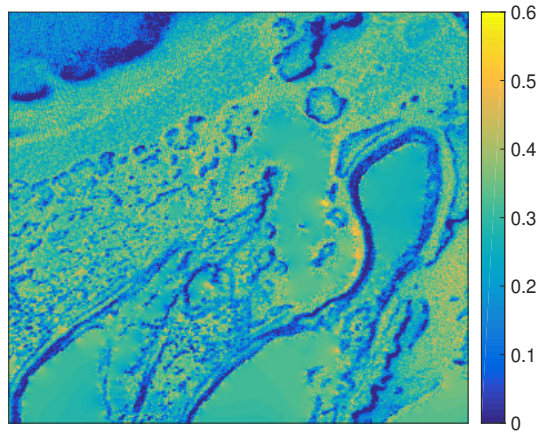


Experiment (*MDB*)

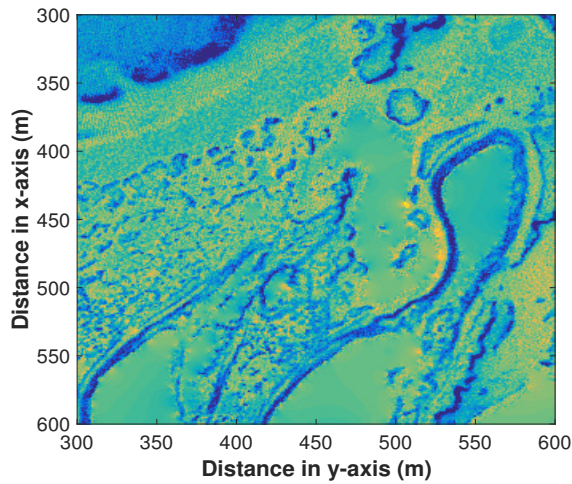


Control

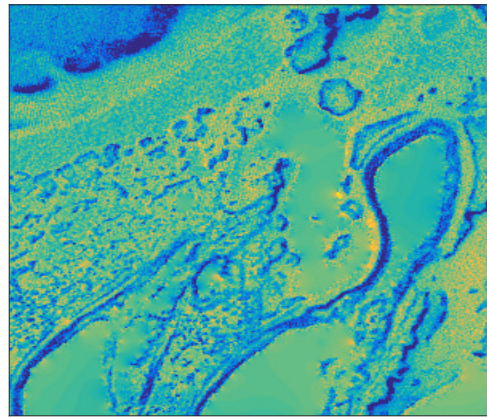
Figure 6.22: Flow depths on the fine-grid scale projected in the test section B at $\eta_t = 0.32$ m ($t = 16.4$ hours). The color scale is of the depth (m)



Reference



Experiment (*MDB*)



Control

Figure 6.23: Flow depths on the fine-grid scale projected in the test section B at $\eta_t = 0.63$ m ($t = 17.6$ hours). The color scale is of the depth (m)

The MDB method computes directional coarse-grid drag coefficients that vary in both space and time (Chapter 4). The minimum drag coefficient is 0.01, which is the value used for the (uniform) fine-grid C_D . The maximum value is 1.0, which can occur when subgrid depths are small. Figures 6.24 through 6.27 depict the resolved-grid drag coefficients in the MDB run for the test sections A and B. There is considerable time-space variability in the drag coefficients and their directionality (i.e., different values in x and y -direction).

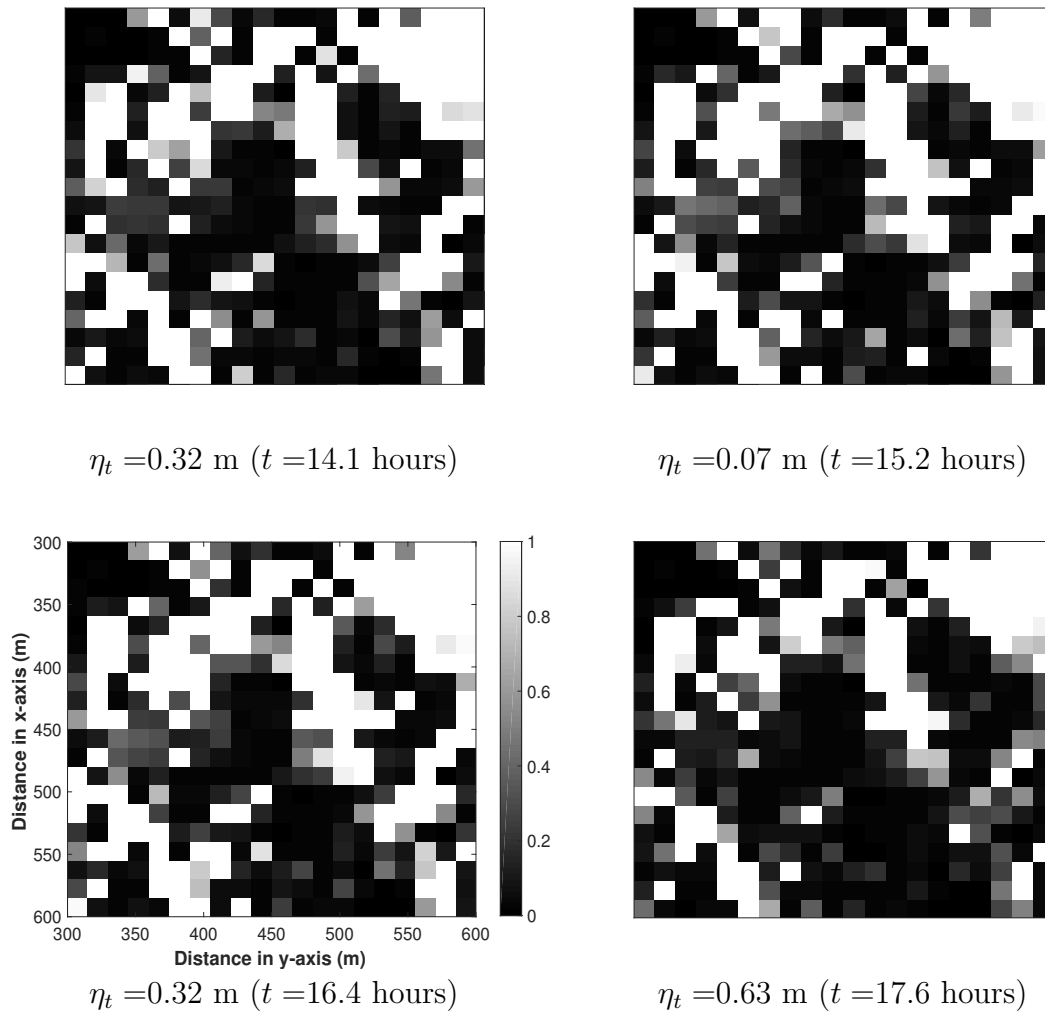


Figure 6.24: x -directional drag coefficients applied to the *MDB* experiment in the test section *A*. The grey scale is the scale of the drag coefficient.

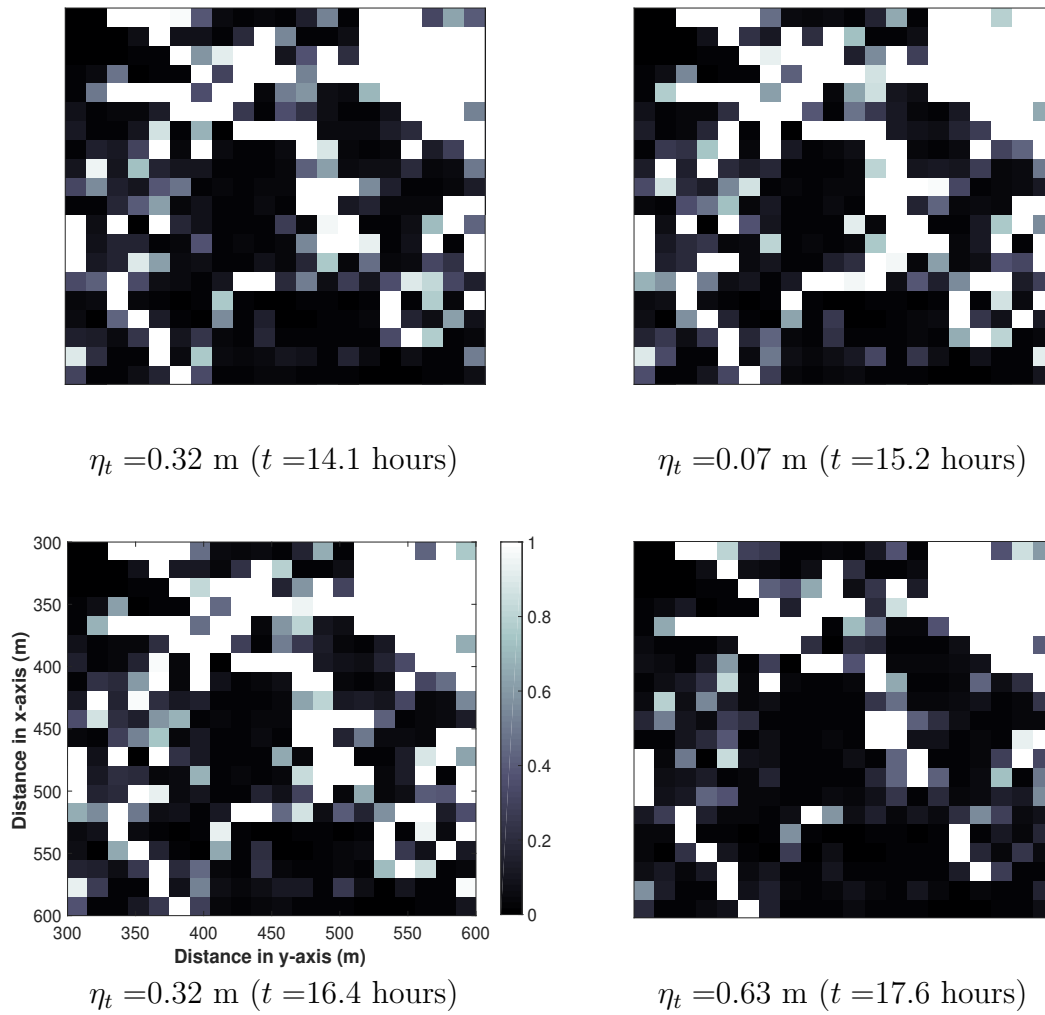


Figure 6.25: y -directional drag coefficients applied to the *MDB* experiment in the test section *A*. The grey scale is the scale of the drag coefficient.

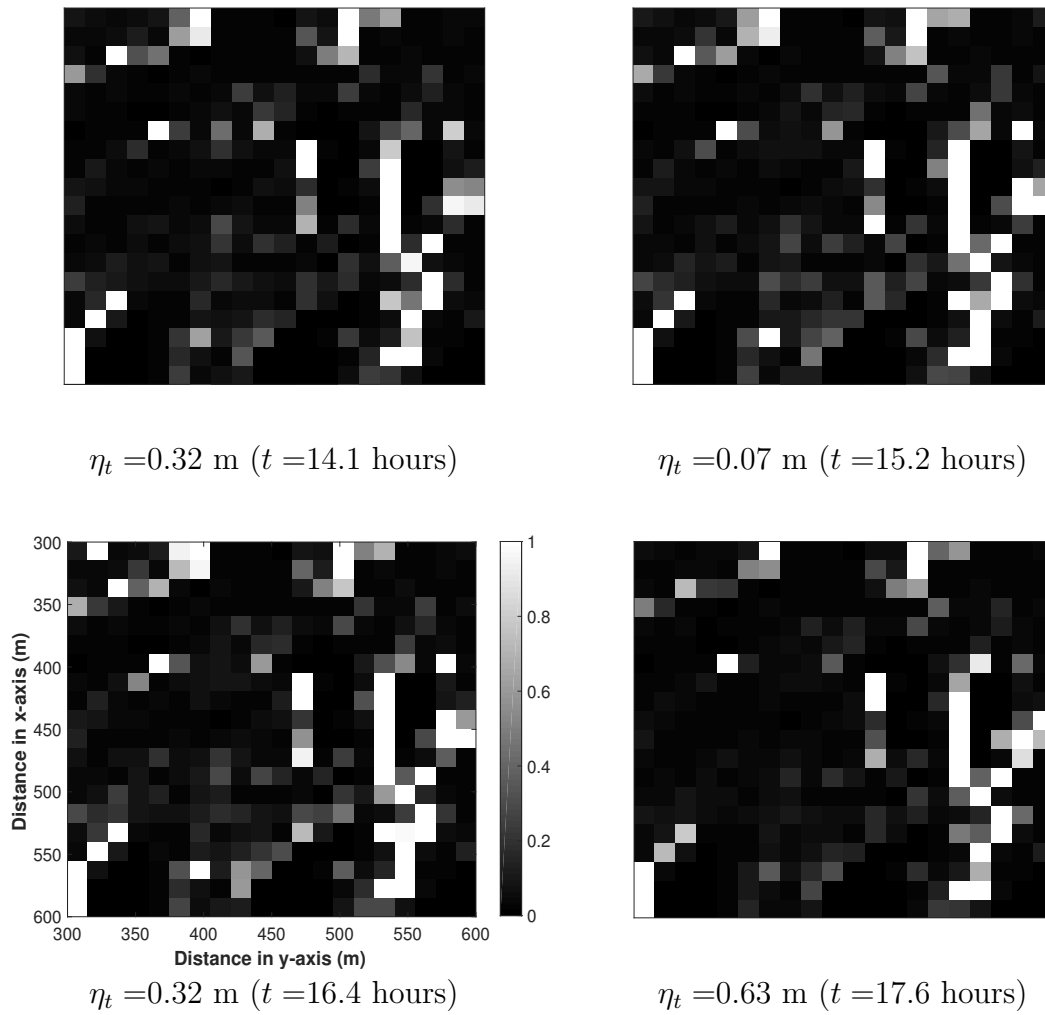


Figure 6.26: x -directional drag coefficients applied to the *MDB* experiment in the test section B . The grey scale is the scale of the drag coefficient.

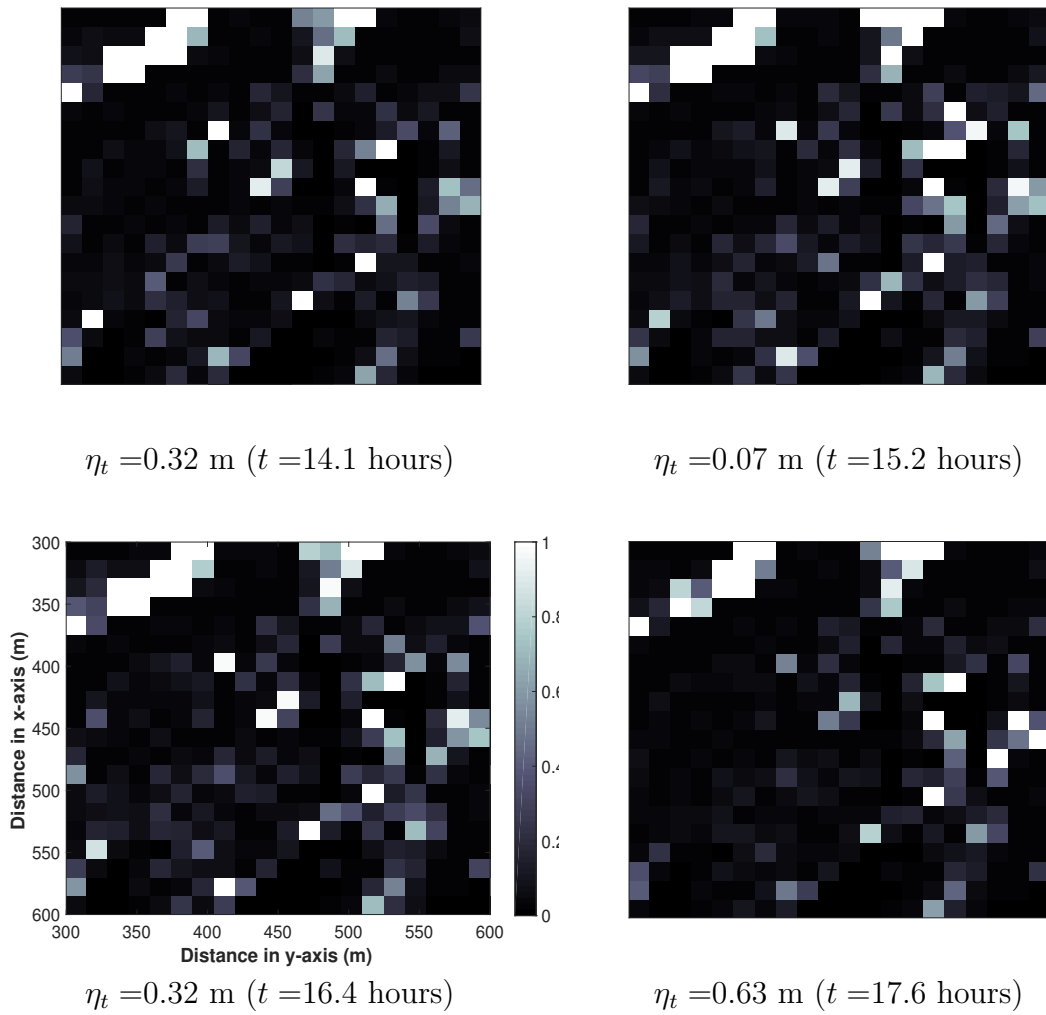


Figure 6.27: y -directional drag coefficients applied to MDB experiment in the test section B . The grey scale is the scale of the drag coefficient.

6.6.4 Evaluation of component models

The error analysis (Section 6.6.2) and the observation of projected flow variables (Section 6.6.3) verify the validity of the combined subgrid model (MDB). Evaluating the performance of individual model components provides insight into the effectiveness of the different approaches. Herein we compare simulations using only the subgrid momentum model (M), only the subgrid drag model (D), and combinations MD, and MB, where B is the topographic sampling method. The Willmott Skill Scores are provided in Tables 6.4 and 6.5

Table 6.4: Absolute mean errors of all the experiments and control

| Run case | $\overline{E_\eta}$ | | $\overline{E_Q}$ | |
|-------------------|---------------------|---------------|------------------|---------------|
| | Section A | Section B | Section A | Section B |
| <i>C</i> | 0.1173 | 0.1368 | 0.4471 | 0.4938 |
| <i>G</i> | 0.0517 | 0.0565 | 1.0607 | 0.8804 |
| <i>MDB</i> | 0.0403 | 0.0365 | 0.4436 | 0.3834 |
| <i>MB</i> | 0.1400 | 0.1488 | 0.5393 | 0.4745 |
| <i>MD</i> | 0.0304 | 0.1390 | 0.4601 | 1.1348 |
| <i>M</i> | 0.0570 | 0.0649 | 0.8185 | 1.3180 |
| <i>D</i> | 0.0891 | 0.0964 | 0.3654 | 0.4278 |

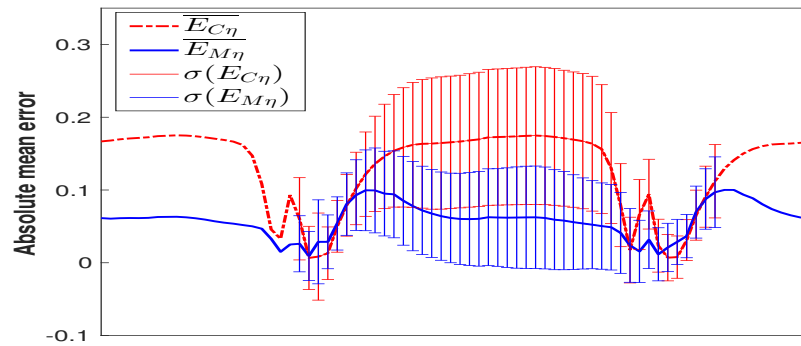
It can be seen that overall the MDB is the preferred scheme, with error metrics and skill scores equivalent to, or better than, the other methods. It is interesting that the absolute mean error for η in the MD case for Section A is slightly less than the MDB error, but the Q error for Section B is dramatically greater. This result indicates that B approach to topography is likely important to obtaining the correct fluxes. The error metrics and skill scores indicate that momentum model (M) is important to getting the surface elevations correct, whereas the drag model and

Table 6.5: Willmott Skill Scores of all the experiments and control

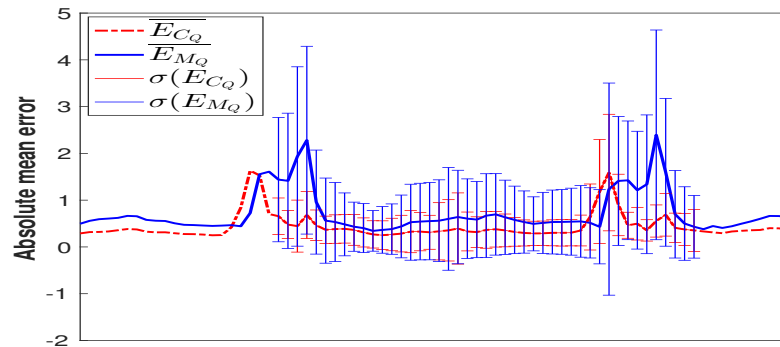
| Run case | \overline{W}_η | | \overline{W}_Q | |
|------------|---------------------|-----------|------------------|-----------|
| | Section A | Section B | Section A | Section B |
| <i>C</i> | 0.9536 | 0.9052 | 0.7228 | 0.6409 |
| <i>G</i> | 0.9906 | 0.9770 | 0.3577 | 0.4186 |
| <i>MDB</i> | 0.9943 | 0.9927 | 0.7535 | 0.6718 |
| <i>MB</i> | 0.9301 | 0.8890 | 0.6732 | 0.6201 |
| <i>MD</i> | 0.9953 | 0.9200 | 0.7341 | 0.3022 |
| <i>M</i> | 0.9894 | 0.9778 | 0.4563 | 0.2477 |
| <i>D</i> | 0.9726 | 0.9499 | 0.7571 | 0.6385 |

bathymetric model (B) are important to getting the fluxes correct. As the Q skill is substantially lower than the η skill, these results indicate that future efforts should focus on improving the flux representation.

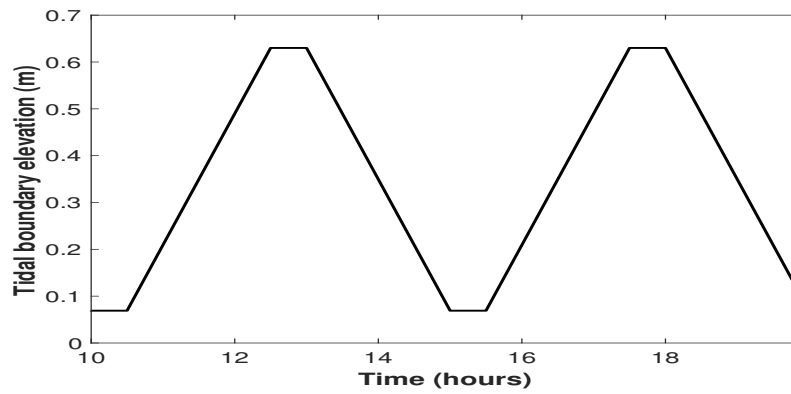
The time-varying error metrics and their variability for cases M and C are shown in Figure 6.28. It can be seen that the η error is smaller and has less variability for the M case, but the Q error for M has significantly greater variability than C. This provides further confirmation that the momentum method alone cannot solve the problem of subgrid topography.



(a) \overline{E}_η



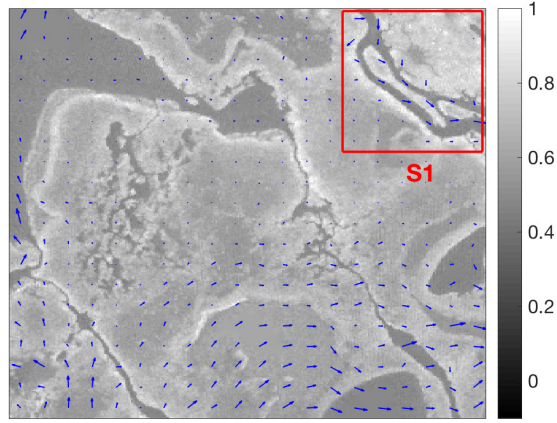
(b) \overline{E}_Q



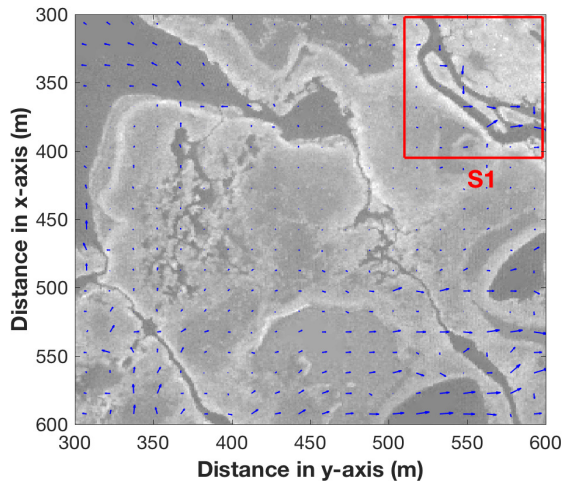
(c) η_t

Figure 6.28: Absolute mean errors of the M experiment and control in the test section A

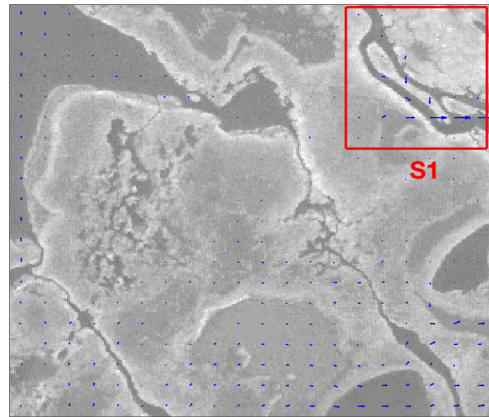
The combination of momentum with the topographic sampling (MB) appears to be more valuable than M alone. Figure 6.29 shows fluxes of M, MB, and F for a typical condition in Section A. Clearly the overall fluxes in MB are close to F, and the channelized area in region S1 is better represented in case MB than in M. In Figure 6.30 for Section A, it can be seen in the S4 region that the M case provides a flux that is entirely in the wrong direction, and misses the entire flow variability around S5. The MB case does not perfectly represent the F case, but does show the directional variability in the S5 region that is closer to the F case. However, comparison of error metrics in Figure 6.31 indicate that the MB combination actually has greater error and variability than the M case for η , but slightly lower variability in Q . From this we conclude that the topographic sampling method (B) is critical to the overall success in representing Q , but appears to introduce some issues into the solution of the free surface. This may indicate a limitation of sampling method for the minimum subgrid elevation (i.e., with an increase of η , the effect of unresolved connectivity below the resolved grid-cell may decrease). Developing a dynamic sampling corresponding to a change of the water level could be one effective approach for addressing flow advection, but such work is beyond the present study.



Reference

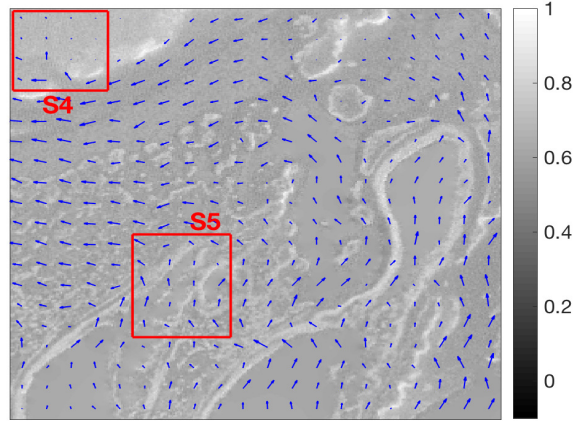


Experiment (*MB*)

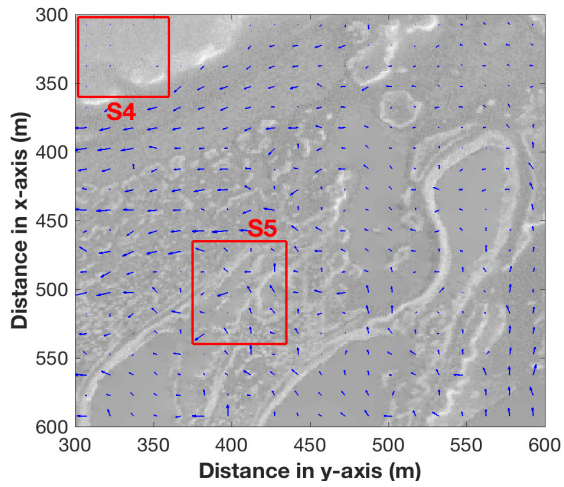


Experiment (*M*)

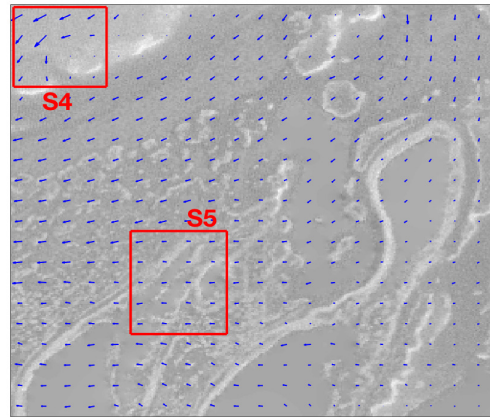
Figure 6.29: Comparison of projected fluxes between the *MB* and *M* experiments in the test section A at $\eta_t = 0.32$ m ($t = 14.1$ hours). The grey scale is of the bottom elevation (m). A blue arrow indicates a flux vector on the resolved coarse-grid cell (m^3/s).



Reference

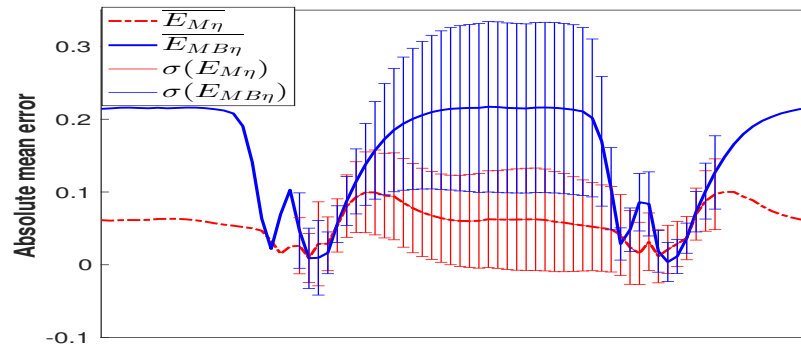


Experiment (*MB*)

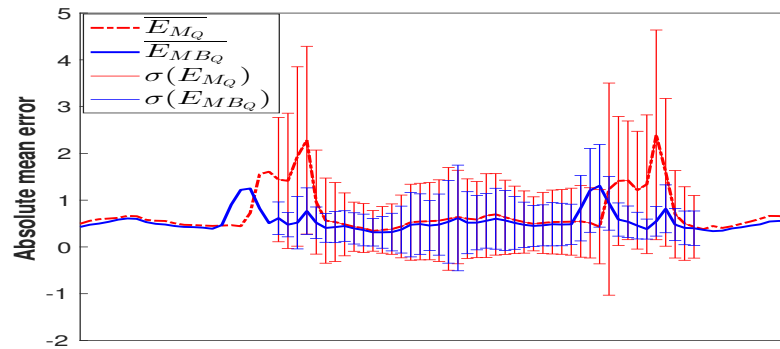


Experiment (*M*)

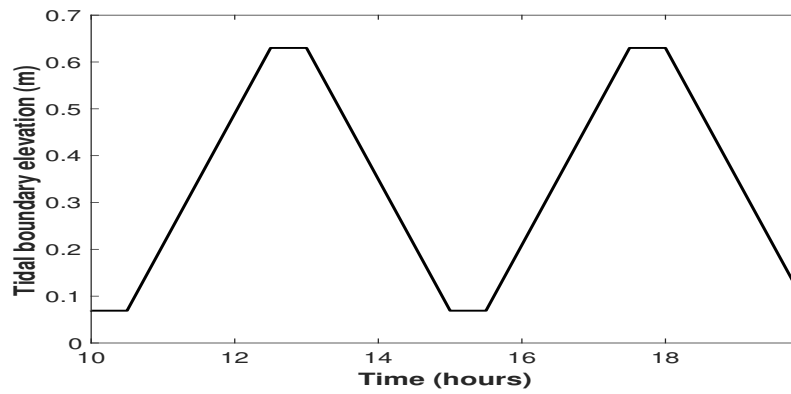
Figure 6.30: Comparison of projected fluxes between the *MB* and *M* experiments in the test section B at $\eta_t = 0.07$ m ($t = 15.2$ hours). The grey scale is of the bottom elevation (m). A blue arrow indicates a flux vector on the resolved coarse-grid cell (m^3/s).



(a) \overline{E}_η



(b) \overline{E}_Q

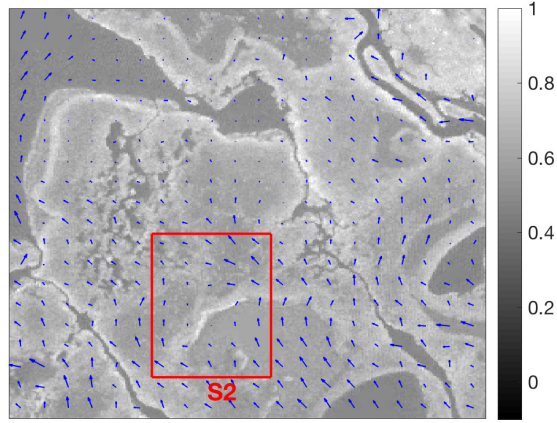


(c) η_t

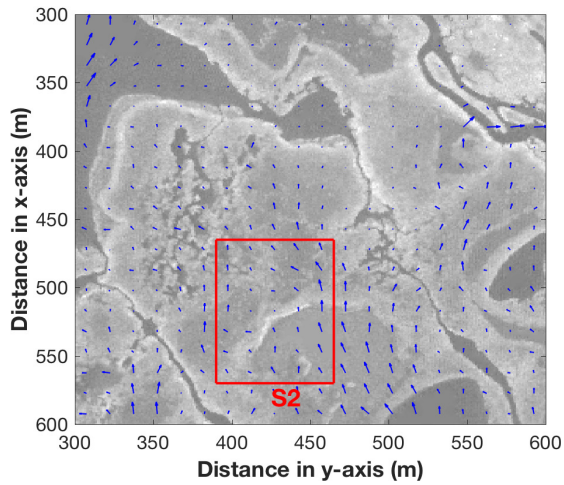
Figure 6.31: Absolute mean errors of the M and MB experiments in the test section A

The subgrid drag model (D) has slightly smaller errors and increased skill compared to the control (C) and prior subgrid model (G) for both η and Q except for the Section B skill score for Q , where the C and D skills are similar. Combining D with M has inconsistent results, causing some error reduction (skill increases) and some error increases (skill reduction) compared to D or M alone. Comparison of the fluxes in the M and MD runs in Figure 6.32 shows that MD is significantly better than M in capturing the flux scales and the deflected flow motion at S2 test section A. These results indicate the subgrid drag term (D) is a critical addition to the momentum model (M) for capturing topographical effects.

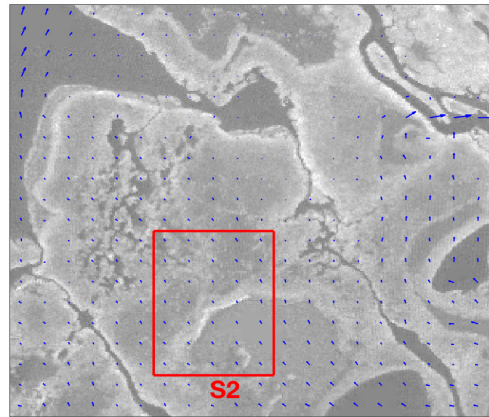
Of particular interest is a comparison of the time-varying, spatially-averaged, free-surface elevation produced by the different model configurations, as shown in Figure 6.33 over the entire simulation time (including spin-up). The MB case significantly underestimates the average surface elevation, as does the control (C). In contrast, the M case slightly underestimates the free surface whereas the MD is quite close after spin-up. The behavior of all the cases is quite different during the initial tidal period, which is likely due to how the different models respond to the initial conditions. Arguably, the fine-grid case (which does not see an initial elevation peak) is filling the test domain initially through small channels, whereas the other simulations can only fill depressions by flooding over significant topographic obstructions.



Reference

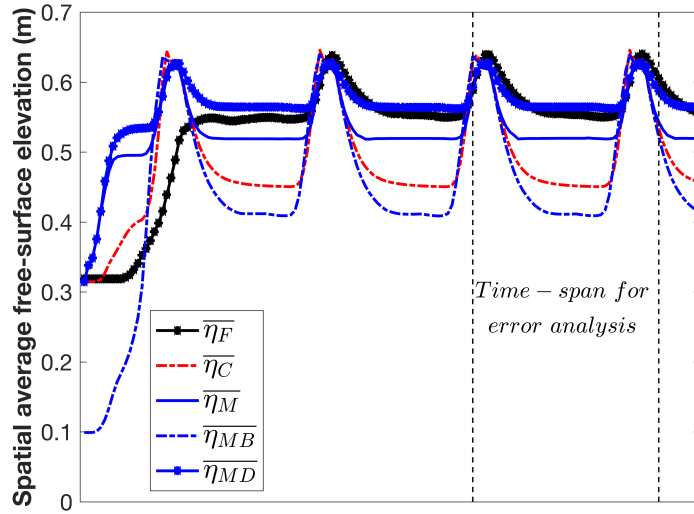


Experiment (*MD*)

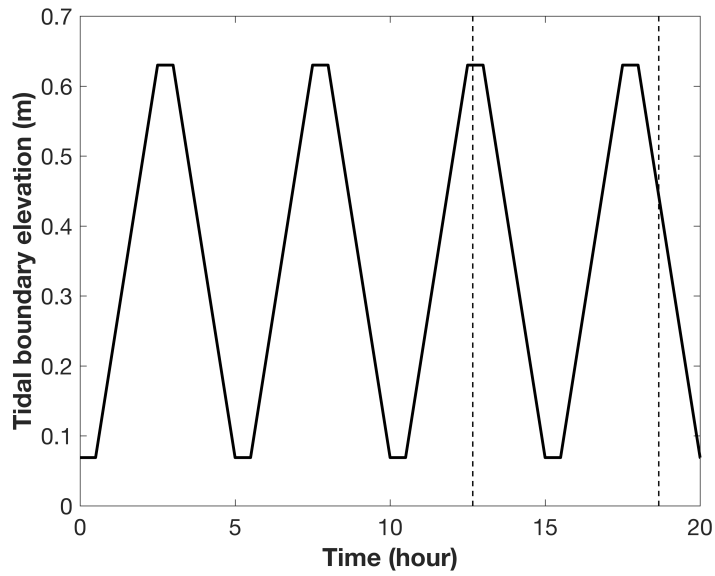


Experiment (*M*)

Figure 6.32: Comparison of projected fluxes between the *MD* and *M* experiments in the test section A at $\eta_t = 0.63$ m ($t = 17.6$ hours). The grey scale is of the bottom elevation (m). A blue arrow indicates a flux vector on the resolved coarse-grid cell (m^3/s).



(a) Spatial average free-surface elevation ($\overline{\eta}$)



(b) Tidal boundary elevation (η_t)

Figure 6.33: Spatial average free-surface elevation of the M , MB , MD experiments, control, and reference in the test section A

6.6.5 Computational cost of subgrid models and look-up table method

The computational cost of the experiments and control was evaluated using the time fraction metric, T , from Eq. (6.17), which relates the computational time of the subgrid model to the computational time for a fine-scale (F) model. Table 6.6 compares the time fraction metric across the experiments and control along with the time-space average error metrics ($\overline{E_\theta}$ & $\overline{W_\theta}$: $\theta \in \{Q, \eta\}$). The time fraction metric of the experiments was measured in the range of 0.011 (D) to 0.027 (MD), which indicates that all the subgrid models used less than 3% of the simulation time that the fine-grid reference model used for the current test scenario. The time fraction metric of MDB model was reduced from 0.026 to 0.021 with a marginal increase of the error metrics by using the look-up table (i.e., MDBL experiment) in the test section A. Thus, the best subgrid method, MDBL used about 2.1% of the reference model's run-time upon the test conditions. It should be noted that this is 3 times the computational time of the control (C), so the subgrid method is computationally expensive relative to the control, but inexpensive relative to the reference. However, as this study was necessarily exploratory in its approach, it is likely that there are coding efficiencies that could further reduce the computational time of the MDBL model.

The look-up table method (L), as described in Appendix D, applies a linear interpolation for approximating subgrid geometry quantities corresponding to the modeled η from the stored data at the interval of $\Delta\eta$. The *MDBL* experiment applied a look-up table built with 0.01 m interval of $\Delta\eta$ for the test section A. Figure 6.34 compares the linearly interpolated grid cell surface area (A_{xy}) of the test

Table 6.6: Time fraction and error metrics of the experiments and the control in the test section A

| Run case | $\Delta\eta$ | Time fraction (T) | $\overline{E_\eta}$ | $\overline{W_\eta}$ | $\overline{E_Q}$ | $\overline{W_Q}$ |
|----------|---------------------------|-----------------------|---------------------|---------------------|------------------|------------------|
| Control | - | 0.007 | 0.1173 | 0.9536 | 0.4471 | 0.7228 |
| G | - | 0.025 | 0.0517 | 0.9906 | 1.0607 | 0.3577 |
| MDB | - | 0.026 | 0.0403 | 0.9943 | 0.4436 | 0.7535 |
| $MDBL$ | 0.01 m (interpolation) | 0.021 | 0.0421 | 0.9922 | 0.6143 | 0.6623 |
| MB | - | 0.025 | 0.1400 | 0.9301 | 0.5393 | 0.6732 |
| MD | - | 0.027 | 0.0304 | 0.9953 | 0.4601 | 0.7341 |
| M | - | 0.024 | 0.0570 | 0.9894 | 0.8185 | 0.4563 |
| D | - | 0.011 | 0.0891 | 0.9726 | 0.3654 | 0.7571 |

section A with a change of $\Delta\eta$ in the look-up table from 0.005 m to 0.1 m. Such an analysis is entirely dependent on the complexity of the topography. For the present study it is clear that a look-up table of $\Delta\eta = 0.05$ m would likely be sufficient, and a table using 0.01 m would be too coarse. It might be useful to develop a look-up table whose intervals are customized for the particular topography and its variability.

Running the 1×1 m grid reference model (F) with the current test scenario required 1.32 hour of computer time for every hour of model simulated time on a 2.7 GHz dual-core processor, which is not practical for multi-scenario modeling across the entire the Nueces River Delta (Appendix A). In contrast, the subgrid models required less than 0.04 hour of computer time for every hour of model simulated time for the test scenarios. However, the costs of dynamically computing the drag coefficient and momentum flux areas are significantly greater than the costs for the simple control (C) model with static drag coefficients over the coarse grid. It seems

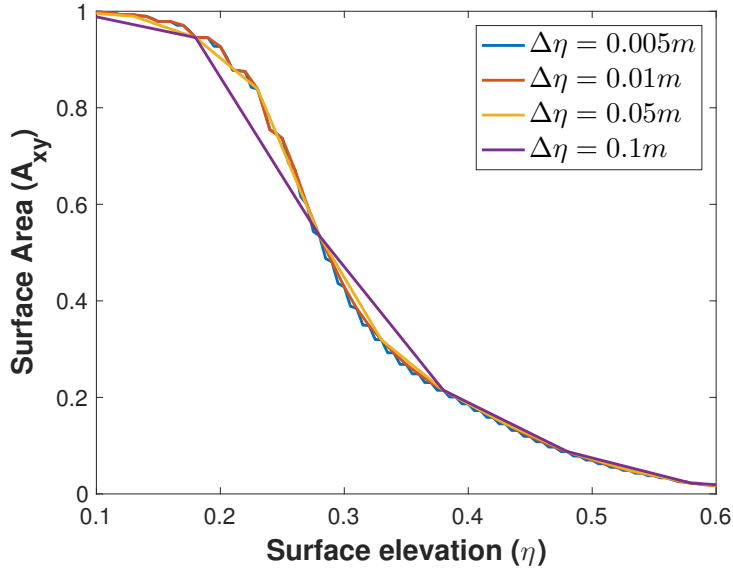


Figure 6.34: Average grid cell surface area with a change of $\Delta\eta$ in the test section A

likely that the extra computational costs can be reduced through coding efficiencies.

6.7 Global indicators for evaluation of subgrid models

The fidelity of a subgrid model is affected by topographic features below the subgrid scale, features at the resolved grid scale, and the algorithm that links these scales. A coarse-grid model using some form of subgrid approach will necessarily have some level of error relative to a fine-resolution model. There remains a challenging question: what level of error is acceptable? Although the standard comparison metrics described in Section 6.5 are useful in evaluating the relative performance of different modeling options, they are less useful in evaluating the consequences of unavoidable model errors. Herein we propose five new indicators that can be used

to evaluate subgrid model performance with quantitative measures. We believe that these indicators will prove useful in the future when selecting the resolved grid scale and subgrid models required for a desired model fidelity.

The topographic features and scales affecting the modeled flow field are diverse, including (i) topographic roughness that impedes flow, (ii) fine-scale connectivity that provides preferential flow channels, (iii) slope variability where concave or convex regions lead to preferential ponding or water shedding. To better evaluate the effects of topography on the subgrid model fidelity, we have devised new indicators that quantify some of these topographic effects. These indicators are:

- WSD : Global water storage difference (Section 6.7.1),
- WSD_m : Global water storage difference below the resolved-grid bottom elevation (Section 6.7.2) ,
- TC : Global topographic connectivity (Section 6.7.3),
- TC_m : Global topographic connectivity below the resolved-grid bottom elevation (Section 6.7.4),
- $\overline{\sigma(z_b)}$ Global subgrid roughness (Section 6.7.5).

The WSD is a global quantification of the cell storage volume difference between the fine-grid and resolved-scale bathymetry. The WSD_m provides further insight through quantifying the WSD that is below the nominal bottom of the resolved grid. The TC is a global measure of smoothness based on spatial covariance.

The TC_m uses a similar approach to TC , but with a focus on the topographic features below the resolved grid cell bottom elevation. The $\overline{\sigma(z_b)}$ provide an indication of the global variability of the topography at the subgrid scale. Section 6.7.6 examines the global indicators to provide insight into the time-varying model behavior.

6.7.1 Global water storage difference

The water storage difference (WSD) is a metric that indicates the relative importance of the unresolved volume at the resolved grid scale based solely on topography (i.e., not incorporating actual model results). The impact of the unresolved volume on the model results can be expected to depend on the ratio of the unresolved volume to the resolved volume. As this ratio depends on the water surface level, the WSD is designed as a integrated metric over a range over water surface levels.

At a given water surface elevation, η_b , the integrated water storage volume for the coarse (resolved) grid is

$$V_C(\eta_b) \equiv \min [\eta_b - Z_b(i, j), 0] \Delta y \Delta x$$

where the $\min[]$ function ensures that cells i, j where $\eta_b < Z_b(i, j)$ are not included as negative volumes. The N_x and N_y are the numbers of grid cells for x and y -directions that compose the test domain, and Δx and Δy are the unit lengths of a model-resolved grid cell for x and y -directions. Similarly, the integrated storage volume for the fine (reference) grid is

$$V_F(\eta_b) \equiv \left\{ \sum_{r=1}^{n_r} \sum_{s=1}^{n_s} \min [\eta_b - z_b(r, s), 0] \Delta s \Delta r \right\}_{(i,j)}$$

where n_r and n_s are the numbers of fine-grid cells for r and s -directions, which share outer boundaries with a coarse-grid cell; and Δr and Δs are the unit lengths of a fine-grid cell. The volume storage difference at water level η_b is

$$\Delta V(\eta_b) \equiv V_F(\eta_b) - V_C(\eta_b)$$

To provide insight into the relative scale of the subgrid topography at a given η_b , we non-dimensionalize by the volume in the test domain between η_b and the lowest point in the fine-grid bathymetry (i.e., as if the entire bottom elevation were uniform at the lowest elevation point). Formally, this provides the non-dimensionalized cell volume difference at the grid cell i, j as

$$\Delta V_S(i, j, \eta_b) \equiv \frac{\Delta V(\eta_b)}{(\eta_b - \min[z_b(\alpha, \beta)])\Delta x\Delta y} : \quad \alpha \in \{1 : n_r\} , \beta \in \{1 : n_s\}$$

Note that in the above, the magnitude of the numerator is always less than the magnitude of the denominator, but the numerator can be either positive or negative. Spatial-averaging of $\Delta V_N(i, j, \eta_b)$ over the test domain provides the non-dimensional storage volume difference over the test region ΔV_N as:

$$\Delta V_N(\eta_b) \equiv \frac{1}{N_x N_y} \sum_{i=1}^{N_y} \sum_{j=1}^{N_x} \Delta V_S(i, j, \eta_b)$$

As $\Delta V_N(\eta_b) \rightarrow 0$, the coarse-grid volume is a better approximation of the fine-grid volume over the test section. As $\Delta V_N(\eta_b) \rightarrow \pm 1$ the difference between the fine-grid volume and resolved-grid volume is increasingly large.

Integrating $\Delta V_S(\eta_b)$ over the minimum to maximum fine-grid topographic elevation provides our definition of the WSD metric as:

$$WSD \equiv \frac{1}{\max(z) - \min(z)} \int_{\min(z)}^{\max(z)} \Delta V_N(\eta_b) d\eta \quad (6.18)$$

The global indicator, WSD has a range of $-1 \sim 1$. The indicator represents a representative scale of unresolved cell storage volume induced by subgrid topographic variability relative to the resolved scale over the test domain and the range of the free-surface elevation between dry and fully submerged topography. A larger magnitude of WSD suggests greater volume distortion at the resolved scale.

6.7.2 Global water storage difference below the resolved-grid bottom elevation

The WSD described above provides a global measure of the error in the resolved grid volume over the range of water surface elevations from dry topography to fully submerged over the test domain. We can modify this metric to evaluate the subgrid volumes that are below the resolved coarse-grid bottom elevation (Z_b). That is, we define a WSD_m metric based on only the fine-grid water volume associated with water surface levels when the associated coarse-grid cell is dry.

The coarse-grid cell i, j water storage volume below both the coarse-grid bottom elevation $Z_b(i, j)$ and below a test-domain uniform water level η_b is

$$V_m(i, j, \eta_b) \equiv \sum_{s=1}^{n_s} \sum_{r=1}^{n_r} h_b(r, s, \eta_b) \Delta r \Delta s$$

where h_b denotes depths at the subgrid cells whose bottoms are located below the resolved-grid bottom elevation (Z_b)

$$h_b(r, s, \eta_b) \equiv \max[\alpha h_f(r, s, \eta_b), 0]$$

where $h_f(r, s)$ is the depth in the fine-grid r, s cell at water surface elevation η_b with

$h_f(r, s) = 0$ for dry cells, i.e.,

$$h_f(r, s, \eta_b) \equiv \max [(\eta_b - z_b(r, s)), 0]$$

and $\alpha \in \{0, 1\}$ is a binary coefficient set to select only cells where the associated coarse grid bottom elevation is higher than the water surface elevation, i.e., $\alpha = 1 \iff Z_b \geq \eta_b$.

The corresponding global non-dimensional unresolved volume (similar to the difference ΔV_N) is

$$V_{Nm}(\eta_b) \equiv \frac{\sum_{i=1}^{N_x} \sum_{j=1}^{N_y} V_m(i, j, \eta_b)}{(\eta_b - \min [z_b(\alpha, \beta)]) \Delta x \Delta y N_x N_y} \quad : \quad \alpha \in \{1 : n_r\} , \beta \in \{1 : n_s\}$$

When the fine-grid elevation $z_b(r, s)$ is identical to the model-resolved grid elevation Z_b and is everywhere uniform across cells i, j , then the V_{Nm} is formally undefined (both numerator and denominator are zero). However, if Z_b is nonuniform and $z_b(r, s)$ is identical to the associated $Z_b(i, j)$ for all r, s cells, then it follows that the denominator is non-zero whereas the numerator $V_m(i, j, \eta_b) = 0$ for all η_b ; therefore $V_{Nm}(\eta_b) = 0$ is the lower bound. Furthermore, the construction of V_{Nm} ensures that (i) its numerator is always non-negative, (ii) the denominator is always positive, and (iii) the numerator always smaller than the denominator. Thus, $0 \leq V_{Nm} \leq 1$.

Limiting η_b to the range of the minimum to the maximum subgrid elevation over the test domain (i.e., $\min [z_b(\alpha, \beta)] \leq \eta_b \leq \max [z_b(\alpha, \beta)]$, $\alpha \in \{1 : n_r N_x\}$, $\beta \in \{1 : n_s N_y\}$), the global metric for the unresolved volume below the model-resolved grid bottom elevation is

$$WSD_m \equiv \frac{1}{\max(z) - \min(z)} \int_{\min(z)}^{\max(z)} V_{Nm}(\eta_b) d\eta \quad (6.19)$$

WSD_m has a range of $-1 \sim 1$. The indicator WSD_m provides a metric for the volume that is below the resolved bottom of the coarse-grid system, which is an indication of whether unresolved volumes might provide flow paths and volume retention at low water surface elevations that will be missing from the coarse-grid system. A larger WSD_m indicates the potential of effects by unresolved flow connectivity below the resolved coarse-grid bottom elevation.

6.7.3 Global topographic connectivity

We propose TC_I as the indicator of the spatial correlation of topographic obstructions that might be poorly resolved at the coarse-grid scale. The TC_I is an integrated measure based on a proposed TC_δ that is inspired by measures of spatial covariance in geostatistics (e.g., [Wackernagel, 2009](#)). Specifically, for N pairs of points x_i with some property θ with separation δ , the spatial covariance is formally

$$C_s(\delta) \equiv \frac{1}{N} \sum_{i=1}^N \theta(x_i)\theta(x_i + \delta) - \overline{\theta(x_i)} \overline{\theta(x_i + \delta)}$$

where $\bar{\theta}$ denotes the mean over the samples.

To develop our metric for the fine-grid topography, we first need an estimate of mean distances between similar elevation levels in the test domain, i.e., the equivalent of $\bar{\theta}$ in the geostatistics spatial covariance. Let $\zeta_b \in \{\zeta_b(1), \zeta_b(2), \dots, \zeta_b(N_b)\}$ represent a finite set of discrete elevations so that a number of fine-grid cells share a common discrete value within some tolerance ϵ , i.e., for any $\zeta_b(k)$ there are a set of fine-grid cells α, β satisfying $\zeta_b(k) - \epsilon < z_b(\alpha, \beta) \leq \zeta_b(k) + \epsilon$, and the number of cells satisfying this condition is $N_\zeta(k)$. It will generally be convenient to have uniform

intervals between adjacent ζ_b values, but that is not necessarily required. Note that the set of discrete ζ_b values and ϵ should be chosen so that $\sum N_\zeta = n_r n_s N_x N_y$; i.e., each fine grid cell is included in exactly one ζ_b set. From the above it follows that $N_\zeta(k)$ is the number of fine-grid cells with $z_b \approx \zeta_b(k)$.

For any $\zeta_b(k)$, let x_m, y_m be the Cartesian coordinates of a fine-grid cell in the $\zeta_b(k)$ set, such that $m \in \{1 : N_\zeta(k)\}$. For simplicity in exposition, let $M = N_\zeta(k)$, then the non-dimensional average distance between the fine-grid cells of similar elevation in the set $\zeta_b(k)$ can be written as

$$L(k) \equiv \frac{1}{\{M-1\}!} \left\{ \sum_{m=2}^M \frac{1}{\ell} [(x_1 - x_m)^2 + (y_1 - y_m)^2]^{1/2} + \sum_{m=3}^M \frac{1}{\ell} [(x_2 - x_m)^2 + (y_2 - y_m)^2]^{1/2} + \cdots + \sum_{m=M-1}^M \frac{1}{\ell} [(x_{M-1} - x_m)^2 + (y_{M-1} - y_m)^2]^{1/2} \right\} \quad (6.20)$$

where ℓ is an appropriate length scale for non-dimensionalizing. Herein we use a normalization length scale equivalent to a half of the diagonal length of the test domain:

$$\ell \equiv \frac{1}{2} \sqrt{(\Delta x N_x)^2 + (\Delta y N_y)^2}$$

It follows that $L(k)$ is a separation length scale providing a measure of the fraction of the domain typically separating cells of $z_b \approx \zeta_b(k)$.

The the normalized mean square separation between cells at levels $\zeta_b(k)$ and $\zeta_b(m)$ can be compared to the product of their separation length scales $L(k)L(m)$ as measure whether topographical obstructions/channelization scaling on $\zeta_b(k) - \zeta_b(m)$

is expected, i.e.,

$$C_1(k, m) \equiv \frac{\sum_{i=1}^{N_\zeta(k)} \sum_{j=1}^{N_\zeta(m)} (x_i - x_j)^2 + (y_i - y_j)^2}{\ell^2 N_\zeta(k) N_\zeta(m)} - L(k) L(m) \quad (6.21)$$

If $C_1 < 0$, the length scales between $\zeta_b(k)$ and $\zeta_b(m)$ are small compared to the connective lengths scales of either $L(k)$ or $L(m)$, which indicates rough topography that is likely to have significant obstructions and channelization. In contrast, if $C_1 > 0$, it can be expected that the topography is smoother with areas of similar elevation being more coherent in space.

As a metric, the problem with C_1 is that it is related to the specific $\zeta_b(k)$ and $\zeta_b(m)$ elevations, which provides $N_b(N_b - 1)$ individual metrics. A more useful metric might be based based on topographic height differences. To do this, we define the difference between $\zeta_b(k)$ and $\zeta_b(m)$ elevations as:

$$\delta_{km} \equiv \zeta_b(k) - \zeta_b(m) \quad (6.22)$$

If we limit our approach to using a uniform incremental distance (δ_h) separating adjacent ζ_b values, then it follows that

$$\delta_{km} = \delta_h (k - m) \quad (6.23)$$

as correlations for $-\delta_{km}$ are the same as for δ_{mk} , we can consider only the positive value, i.e.,

$$1 \leq \frac{\delta_{km}}{\delta_h} \leq N_b - 1 \quad (6.24)$$

We can now define a metric for the vertical separation of $n\delta_h$ as

$$TC_\delta(n) \equiv \frac{\sum_{k=1}^{N_b} C_1(k, k+n) N_\zeta(k) N_\zeta(k+n)}{\sum_{k=1}^{N_b} N_\zeta(k) N_\zeta(k+n)} \quad : \quad 1 \leq n \leq N_b - 1 \quad (6.25)$$

which provides $N_b - 1$ metrics over a range of $n\delta_h$ scales to describe the spatial relationships. Similar to C_1 , for $TC_\delta < 1$ we expect obstructions and/or channelization and for $TC_\delta > 1$ we expect relative smoothness.

Finally, we can define TC_I as an integrated metric of the correlation scales across all separation distances:

$$TC_I \equiv \frac{1}{N_b - 1} \sum_{n=1}^{N_b-1} TC_\delta(n) \quad (6.26)$$

This preserves the meaning of TC_δ that values $TC_I > 1$ are relatively smooth topography and $TC_I < 1$ are obstructed or channelized.

6.7.4 Global topographic connectivity below the resolved-grid bottom elevation

We can modify TC_I to evaluate the spatial correlation of topographic obstructions that are below the resolved coarse-grid bottom elevation (Z_b). That is, we define a TC_{Im} metric based on the spatial correlation of only the fine-grid cells whose elevations are below Z_b , which is as an indicator for the potential of subgrid flow passages at the surface elevation below the resolved grid bottom elevation. Note that the metric analyzes the spatial correlation of fine-grid cells over the test domain like TC_I , but it uses only the fine-grid cells (α, β) at the coarse-grid cell (γ, κ) satisfying the condition $z_{b(\gamma, \kappa)}(\alpha, \beta) < Z_b(\gamma, \kappa)$: $\alpha \in \{1 : n_r\}$, $\beta \in \{1 : n_s\}$, $\gamma \in \{1 : N_x\}$, $\kappa \in \{1 : N_y\}$.

Consider for any $\zeta_{bs}(k)$ that there are a set of fine-grid cells α_s, β_s satisfying both $\zeta_{bs}(k) - \epsilon < z_b(\alpha_s, \beta_s) \leq \zeta_{bs}(k) + \epsilon$ and $z_{b(\gamma, \kappa)}(\alpha_s, \beta_s) < Z_b(\gamma, \kappa)$, and the number of cells satisfying this condition is $N_{\zeta_s}(k)$. Let x_s, y_s be the Cartesian coordinates of a fine-grid cell in the $\zeta_{bs}(k)$ set, such that $s \in \{1 : N_{\zeta_s}(k)\}$. Then Eqs. (6.20) through (6.26) above are computed correspondingly for $\zeta_{bs}(k)$, x_s , and y_s . The resulting metric in a form that is similar to Eq. (6.26), but computed with $\zeta_{bs}(k)$, x_s , and y_s , is denoted as TC_{Im} .

6.7.5 Global subgrid roughness

As a simple metric representing variability of subgrid topography over the test domain, we can use the average of the standard deviations of subgrid topographic elevations in each resolved coarse-grid cell over the test domain, i.e., let denote $\sigma(z_b)$ as the standard deviation of subgrid elevations over a resolved coarse-grid cell, and the average of $\sigma(z_b)$ over the test region is denoted as $\overline{\sigma(z_b)}$ which is used as the subgrid roughness metric in the current work.

The standard deviation of fine-grid topographic elevations over the resolved coarse-grid cell is:

$$\sigma(z_b) \equiv \sqrt{\frac{1}{n_r n_s} \sum_{s=1}^{n_s} \sum_{r=1}^{n_r} (z_b(r, s) - \overline{z_b})^2}$$

with $\overline{z_b}$ denoting the average of fine-grid bottom elevations over the resolved grid cell, i.e.,

$$\overline{z_b} \equiv \frac{1}{n_r n_s} \sum_{s=1}^{n_s} \sum_{r=1}^{n_r} z_b(r, s)$$

It follows that $\overline{\sigma(z_b)}$ is:

$$\overline{\sigma(z_b)} \equiv \frac{1}{N_x N_y} \sum_{i=1}^{N_x} \sum_{j=1}^{N_y} \sigma(z_b)_{(i,j)} \quad (6.27)$$

The metric arguably has an effect of considering the relative variability of subgrid topography over the discretized grid scale, compared with the standard deviation of all the fine-grid cells over the test region, i.e.,

$$\sigma_e(z_b) \equiv \sqrt{\frac{1}{N_x N_y} \sum_{i=1}^{N_x} \sum_{j=1}^{N_y} \left[\frac{1}{n_r n_s} \sum_{r=1}^{n_r} \sum_{s=1}^{n_s} (z_b(r, s) - \overline{z_b})^2 \right]_{(i,j)}}$$

where $\overline{z_b} \equiv (1/N_x N_y) \sum_{i=1}^{N_x} \sum_{j=1}^{N_y} [(1/n_r n_s) \sum_{r=1}^{n_r} \sum_{s=1}^{n_s} z_b(r, s)]_{(i,j)}$.

6.7.6 Evaluation of subgrid models with indicators

One question raised from the test results (Sections 6.6.2 and 6.6.3) is different behaviors of the model behavior in several coupled approaches between the test sections A and B. The performance of a subgrid model is arguably affected by diverse features of subgrid topography, a scale ratio of subgrid and resolved topography as well as the limitations of the model's parameterization.

As an experiment examining use of the indicators, the present work compares any possible linkages between the models simulations (Tables 6.4 and 6.5) and magnitudes of the indicators for the test sections A and B in Table 6.7.

The test results (Section 6.6.4) provides different performances of the models between the test sections A and B, which are: (i) the coarse-grid control model provided larger discrepancies for both η and Q from the reference in the test section

Table 6.7: Magnitude of global indicators for the test bathymetries

| Test Bathymetry | WSD | WSD_m | TC_I | TC_{Im} | $\overline{\sigma(z_b)}$ |
|-----------------|--------|---------|--------|-----------|--------------------------|
| A | 0.0173 | 0.0104 | 1.2296 | 0.5148 | 0.1255 |
| B | 0.0178 | 0.0092 | 0.3952 | 0.3048 | 0.0787 |

B than A; (ii) coupling with the B aspect was more effective in reducing discrepancies of the coarse-grid solution for Q from the reference in the test section B than A; (iii) coupling with the D aspect was effective in reducing discrepancies for both η and Q in the test section A, but was not for η in the section B; (iv) different behaviors of the M/G aspects between the test sections A and B.

One dominant difference of subgrid topography between the test sections A and B is a difference in magnitude of the topographic connectivity indicator, TC_I , Eq. (6.26) as shown in Table 6.7. The indicator TC_I was measured to be three times as large in the test section A than B, which indicates smoother topography for the test section A. A difference in magnitude of the indicator for submerged subgrid variability WSD , Eq. (6.18) is slight between the two regions. The magnitudes of the indicators for subgrid topography below the model-resolved grid bottom elevation, i.e., WSD_m , Eq. (6.19) and TC_{Im} , show a similar pattern to the case of WSD and TC_I , which indicate a higher subgrid connectivity below the resolved grid cell bottom elevation for the test section A. However, a larger $\overline{\sigma(z_b)}$, Eq. (6.27) in the test section A compared to B (i.e., A's is about 1.5 times of B's) indicates a higher variability of subgrid topography in the test section A than B, while its magnitude is relatively small in both regions. Such indication for higher subgrid connectivity and higher variability in the test section A may be able to explain better performance of the D

model aspect in the test section A. However, this idea is not matched with larger discrepancies of the control model and better performance of B aspect in the test section B.

Verifying the global utility of the indicators requires investigations using more diverse controlled bathymetric data (e.g., reversed bathymetries, smoothed bathymetries) and models simulations. One issue in developing indicators is a scale ratio of the resolved topography and the subgrid bathymetry. A scale ratio of neglected subgrid topography and the resolved bathymetry can be an indicator for the performance of the subgrid model. The other issue is the effect of time-varying water surface elevation, which provides time-varying wet-dry interfaces (e.g., emergent topography changes with the water level). Arguably, the effect of neglected subgrid topography moderates or decreases as the water level increases.

The indicators, WSD and WSD_m represent a difference between the resolved topography and the subgrid topography, although their magnitudes are small and similar in two region. The connectivity indicators, TC_I and TC_{Im} can be applied for the resolved bathymetry with a correcting factor for a different grid scale. Any differences of these indicators in magnitude between the resolved bathymetry and subgrid bathymetry can provide insight for understanding a subgrid model behavior. The proposed indicators are integrated (averaged) across the spatial domain and along the length of the minimum subgrid bottom elevation to the maximum subgrid bottom elevation over the test domain. Substituting a range of possible water surface elevation for the length of the minimum subgrid elevation to the maximum subgrid elevation can be useful for the indicators.

Chapter 7

Conclusions and Future Works

7.1 Addressing the research objectives

The present work developed a new subgrid drag model by deriving a relationship between subgrid topography and the resolved grid cell scale that provides integrating of time-space varying subgrid drag effect at the resolved grid scale (Chapter 4). The new subgrid drag model provides time-space varying directional drag coefficients parameterizing variability of subgrid drags on the resolved grid scale, which has an effect of capturing energy dissipation of subgrid obstructions. The present work verified the effect of the new model's parameterization of subgrid drag in the numerical tests which showed improved model fidelity in projection of directional fluxes by coupling the drag approach.

This study developed a new subgrid momentum model by constructing the momentum sources with the integrated fluxes in/out the faces of a grid cell (Chapter 5). The new momentum model coupled with the flow continuity model for the integrated fluxes on the faces of a grid cell provides the free-surface solution representing subgrid topographic effect across resolved grid faces on surface shear forces and flow continuity, which has an effect of representing strict mass and momentum conservative relationships.

Sampling the minimum subgrid elevation for addressing flow connectivity below the resolved-grid cell bottom elevation was verified to improve model fidelity for projection of directional fluxes by coupling with the new drag and momentum models. The expected effect of the coupled approach using the new subgrid drag model, the new momentum model, and the subgrid topography sampling is representing an unresolved combined effect of subgrid topography in subgrid region, at the interface between two resolved grid cells, and below a resolved coarse-grid bottom elevation.

The coupled approach was verified to improve model fidelity at the coarse-grid (15×15 m) scale in the current test scenario. One advantage of the coupled model was representation of horizontal flow deflection caused by topographic obstructions, which was excluded in the coarse-grid solution without subgrid scheme.

The look-up table that pre-stores subgrid geometric data at the pre-defined interval of the surface elevation had an effect of reducing computational cost of our subgrid model, while its effectiveness might be limited by the pre-defined interval scale and the interpolation scheme.

This study proposed five new global indicators for integrated effects of subgrid topography over the test region. The new indicators were examined for their use in an analysis of the subgrid model behavior, but verifying the utility of the indicators requires more investigations using diverse bathymetric data and model simulations.

7.2 Recommendation for future work

Noting that the validity of the new subgrid models was verified for the test scenario of the current work, further investigation using diverse test scenarios is recommended for verifying the effectiveness of the new models. For examining the use of the new indicators for a study of a subgrid model behavior, further investigation using diverse bathymetries is recommended.

Developing a subgrid turbulence model that addresses horizontal shear effects by distributed subgrid topographic features is recommended. The present subgrid drag model approximated subgrid bottom shears to be dominant over subgrid horizontal shears. Neglected horizontal shear effects can be problematic in modeling studies that are interested in local flow processes (e.g., narrow channels). Combining the quadtree approach [Volp et al. \(2013\)](#) for surface shear forces with our subgrid drag model can provide an effective approach.

Developing a subgrid topography sampling for ensuring flow connectivity below the resolved-grid cell bottom elevation is recommended. The current work simply assigned the minimum subgrid elevation for the model-resolved grid elevation. A dynamic sampling corresponding to a change of the water level can be effective for addressing unresolved flow advection. Developing an dynamic and customized interpolation scheme corresponding to the water level and topographic feature is recommended for the applicability of the look-up table.

Appendices

Appendix A

Nueces Delta and Restoration Efforts

A.1 Geography and climate

The Nueces Estuary is located nearby the city of Corpus Christi in the southeast Texas. It consists of the Nueces Delta, the Nueces River tidal segment, the Corpus Christi Bay, the Nueces Bay, the Oso Bay, and the Redfish Bay (Montagna et al., 2009a). The Nueces Delta which extends about 57 km^2 (Montagna et al., 2009b) $\sim 75 \text{ km}^2$ (United States and Bureau of Reclamation, 2000) is mainly composed of shallow vegetated marshes, mudflats, and shallow ponds (Fig. 1.6). This region is belonged to the semi-arid climate zone where mean precipitation is about $75\sim 76 \text{ cm/year}$ (Rasser, 2009; Tolan, 2007).

The Nueces Delta receives freshwater from the Nueces River, pumped water from the Calleen Pool through the Rincon Bayou Pipeline, and rainfall. While the Nueces River passes by the delta at the usual time, it overbanks into the Nueces Delta on the occasion of severe floods (Hill et al., 2012).

Tidal flow from the Gulf of Mexico is the another source of water for the Nueces Delta. The daily tidal range was reported to be about 0.3m (Hodges et al., 2012) while the tidal elevation varies seasonally (neap and spring tides) and annually: e.g., the water level changed from -0.25 to 1.06m (NADV88 datum) during October

2009 through September 2010 at the White Point station (011) by the Conrad Blucher Institute for Surveying and Science, Texas A&M University-Corpus Christi (herein, CBI); and at near the inlet to the Nueces Bay (NUDE3 station (043)), the water level varied from -0.63 to 0.86m during October 2011 through September 2012 (water depths measured at station datum were converted to NADV88 datum). The salinity of the region broadly varies: e.g., approximately 2~34 parts per thousand (ppt) in the Nueces Delta and Bay ([Guadalupe, San Antonio, Mission, and Aransas Rivers and Mission, Copano, Aransas, and San Antonio Bays Basin and Bay Expert Science Team, 2011](#)); and 1~70 practical salinity units (psu) in the Nueces Delta during October 2011 through September 2012 at NUDE2 (042) by CBI. Mean annual salinity was recorded to be approximately 25 ppt in the Nueces Delta and Bay ([Guadalupe, San Antonio, Mission, and Aransas Rivers and Mission, Copano, Aransas, and San Antonio Bays Basin and Bay Expert Science Team, 2011](#)).

A.2 Threats to the Nueces Delta

The tidal marshes of the Nueces Delta in the southern Texas have provided unique habitats for wildlife ([Zimmerman et al., 2002](#)). The stuarine systems provide breeding or nursery habitats for about 50% of commercial marine finfish and shellfish in the US ([Lellis-Dibble et al., 2008](#)). The tidal-freshwater seasonal pulse helps nutrient exchange and distribution, and buffers against drastic changes of the salinity and temperature ([Hill et al., 2015](#)). However, man- and nature-made interruptions have substantially reduced freshwater inflow to the Nueces Delta, thereby altering the tidal-freshwater balance in this region ([Hill et al., 2012](#)).

Severe droughts and increasing urban water use have significantly altered freshwater inflow to the Nueces Delta since 1940 ([Guadalupe, San Antonio, Mission, and Aransas Rivers and Mission, Copano, Aransas, and San Antonio Bays Basin and Bay Expert Science Team, 2011](#)). The precipitation dropped to be as little as 20.0cm during September 2010 through August 2011 at NUDEWX gauge in the proximity of the delta, while most of this precipitation was measured before the drought season began ([Tunnell and Lloyd, 2011](#)). Moreover, consecutive construction of dams (the Wesley Seale Dam (Lake Corpus Christi) (1958) on the Nueces River and the Choke Canyon Dam (1982) on the Frio River) and increased water use upstream have significantly reduced freshwater inflow to the delta. For example, [Asquith et al. \(1997\)](#) reported that the mean number of annual overbanking events has decreased from 2.3 to 0.8 since the construction of the Choke Canyon Dam (1982). As a result, the mean annual freshwater that flows into the upper delta has dropped by over 99% since 1980s, compared to the record before 1958 ([United States and Bureau of Reclamation, 2000](#)).

Reduced freshwater inflow made seawater intrude further to upstream, thereby, increasing the salinity over the delta. Increased porewater salinity is posing a danger to marine fish species as the porewater salinity over 25 ppt could significantly limit the productivity of biomass which feeds marine fish species ([Stachelek, 2012](#)). The alteration in seasonal freshwater flushing has affected the sedimentation and erosion processes in the region, which it that considerable tidal marsh vegetations in the lower delta has been lost by enhanced erosion ([Hodges et al., 2012](#)). A weakened sedimentation and a loss of vegetation are degrading ecological habitat conditions,

which provide breeding and nursery habitats for diverse marine species ([Guadalupe, San Antonio, Mission, and Aransas Rivers and Mission, Copano, Aransas, and San Antonio Bays Basin and Bay Expert Science Team, 2011](#)).

A.3 Restoration effort for the Nueces Delta

The ecological ill-functioning of the Nueces Estuary resulted in its being considered as the only part of an estuarine system which is ecologically unsound in the comprehensive studies mandated by Texas Senate Bill 3 ([Guadalupe, San Antonio, Mission, and Aransas Rivers and Mission, Copano, Aransas, and San Antonio Bays Basin and Bay Expert Science Team, 2011](#)). For restoring the ecological soundness of the Nueces Estuarine system, USCE, the Coastal Bend Bay and Estuaries Program (herein CBBEP), and the Texas Water Development Board (herein TWDB) have proposed and implemented multiple measures since 1980s. These measures included construction of bypass pipelines and overflow channels which supply freshwater to the delta and establishment of environmental flow recommendations as described fully below.

Multi-agency collaboration efforts led to construction of freshwater pumping facilities and establishment of freshwater inflow recommendations ([Hill et al., 2015](#)), but, we lack a comprehensive understanding on the efficient way of supplying freshwater to maximize the ecological efficiency in the delta. Ecological habitats require hydrologic heterogeneity for their maintenance ([Crowder and Diplas, 2000](#); [Poff et al., 1997](#)). Achieving the ecological effectiveness of inundation needs a best estimate on flow processes in time-space scales. Such circumstance required the Frehd model

(Chapter 3) as a tool for investigation on freshwater pumping scenarios (see Section A.4).

A.3.1 Rincon Bayou demonstration and diversion project

The US Bureau of Reclamation (herein USBR) conducted the Rincon Bayou Demonstration Project for a purpose of sending more freshwater to the delta during 1994 ~ 1999 (Guadalupe, San Antonio, Mission, and Aransas Rivers and Mission, Copano, Aransas, and San Antonio Bays Basin and Bay Expert Science Team, 2011; United States and Bureau of Reclamation, 2000). This project proposed the construction of (i) the Nueces Overflow Channel that connects the Nueces River to the headwater of the Rincon Bayou Creek and (ii) the Rincon Bayou Overflow channel that connects the upper Rincon Bayou Creek to the tidal mudflat of the delta. The Nueces Overflow Channel was closed in 2000 and re-opened in 2001. These overflow channels are used only in overbanking floods.

The Rincon Bayou Pipeline is capable to deliver up to 60,000 gallon/minute and to 3,000 acre-feet/month with all three pumps operating from the Calallen Pool to the upper delta (Montagna et al., 2009b). The Calallen Dam and Pool were created to prevent seawater intrusion from impairing drinking water resource of the city of Corpus Christi in the late 1980s. They are located approximately 10 mile upstream from the mouth of the river. The Rincon Bayou Pipeline was completed and has been operated since 2008 (Tunnell and Lloyd, 2011). Nueces River Authority monitors the amount of freshwater pumped through the pipeline to the delta.

A.3.2 Allison wastewater treatment plant diversion project

The City of Corpus Christi conducted the Allison Wastewater Treatment Plant Diversion Project, which included a construction of a pipeline to deliver the treated water from the Allison Wastewater Treatment Plant to the delta during 1997 ~ 2003. The Wastewater plant located in the south bank of the Nueces River has discharged its secondary treated effluent to the Nueces River since it was built in 1966. The pipeline, which was created below the bottom of the Nueces River, can deliver the wastewater plant effluent of approximately 2.0×10^6 gallon/day from the plant to the lower delta region. the project helps ease the salinity surge in the lower delta, but its capacity may not be sufficient for the freshwater flushing effect in the delta (Ryan, 2011).

A.3.3 Nueces Delta freshwater inflow

The “environmental flow” (herein, EF) indicates the flow required for maintaining an ecologically sound environmental condition (“recommended flow regime for environment and ecosystem”) in river, channels, estuaries, and bays (Nueces River and Corpus Christi and Baffin Bay Basin and Bay Area Stakeholder Committee, 2012). The environmental flow is often compatibly used with the “instream flow” required for inland water bodies or “freshwater inflow” required for coastal water bodies. Herein, the EF in the Nueces Delta indicates the latter case. A plan for EF supply addresses diverse factors of EF regime, such as timing, frequency, quantity, and duration, based on regional hydrodynamic conditions (Bradsby, 2009).

Two legislative directives guide EF plan in Texas: the Senate Bill 2 and the

Senate Bill 3. The Senate Bill 2 directs state agencies to conduct the data collection and evaluation programs for attaining the data required for determining EF recommendations (Mallard et al., 2005). The Senate Bill 3 directs to determine EF recommendations based on the data by the Senate Bill 2 for all Texas river basins and estuaries (Guadalupe, San Antonio, Mission, and Aransas Rivers and Mission, Copano, Aransas, and San Antonio Bays Basin and Bay Expert Science Team, 2011). The Senate Bill 3 enhances a stakeholders leading process for establishing EF recommendations. In accordance with the Senate Bill 3, 7 among 11 basins in Texas have established EF recommendations to date (Texas Water Development Board, 2014.3; <http://www.twdb.state.tx.us/surfacewater/flows/environmental/index.asp>).

The recent EF recommendations for the Nueces Estuarine system, i.e., Nueces River and Corpus Christi and Baffin Bay Basin and Bay Area Stakeholder Committee (2012), were proposed based on the HEFR method, which categorizes flow conditions into four regimes: subsistence flows, base flows, high flow pulses, and overbank flows (Science Advisory Committee, 2009). Each flow regime was classified based on magnitude, duration, timing frequency, and rate of change. Hydrologic conditions of each flow regime were combined with the data of ecology, geomorphology, and water quality for assessing the integrated ecological functioning under each flow regime. Based on the full years records, Guadalupe, San Antonio, Mission, and Aransas Rivers and Mission, Copano, Aransas, and San Antonio Bays Basin and Bay Expert Science Team (2011) investigated 25, 50, and 75 percentile of daily flows at perennial streams in the basin as the base flows in dry, average, and wet hydrologic conditions, while it determined the subsistence flow, using the median of the lowest 10% base

flows that did not include zero flows. It followed that high flow pulses and overbank flow, based on the frequency of the flow events that increased above 75 percentile daily flow were determined, using logarithmic regression model and multipeaks-multiplier hydrographic separation method (selected multiplier: 1.5).

Considering an interaction of flow regime and ecological condition, [Guadalupe, San Antonio, Mission, and Aransas Rivers and Mission, Copano, Aransas, and San Antonio Bays Basin and Bay Expert Science Team \(2011\)](#) established multi-tier EF recommendations to achieve a desirable environmental flow regime at each hydrologic condition. [Nueces River and Corpus Christi and Baffin Bay Basin and Bay Area Stakeholder Committee \(2012\)](#) reviewed and approved the recommendations through the stakeholders decision-making process. The EF recommendations are summarized in Table A.1. Detailed methodology and processes are out-lined in [Nueces River and Corpus Christi and Baffin Bay Basin and Bay Area Stakeholder Committee \(2012\)](#).

Table A.1: Environmental flow recommendations for the Nueces Delta and Bay

| Condition (Target salinity) | Nueces Bay Freshwater Inflow Regime | | | | Recommendations |
|--------------------------------|--|----------------------|----------------------|-------------|---------------------------------|
| | Nov. ~ Feb. | Mar. ~ Jun. | Jul. ~ Aug. | Sep. ~ Oct. | Annual Total |
| - | one overbanking event per year of 39,000acft, maximum discharge of 3,600cfs | | | | - |
| High Flows (10ppt) | 125,000acft (Attainment 11%) | 250,000acft (11%) | 375,000acft (12%) | | 750,000acft (Attainment 16%) |
| Base Flows (18ppt) | 22,000acft (23%) | 88,000acft (30%) | 56,000acft (40%) | | 166,000acft (47%) |
| Subsistence Flows (34ppt) | 5,000acft (69%) | 10,000acft (88%) | 15,000acft (74%) | | 30,000acft (95%) |

Previous EF plans were based on the system (upstream reservoir) storage and allowed for no pass when the system storage drops under 30% ([Nueces River](#)

and Corpus Christi and Baffin Bay Basin and Bay Area Stakeholder Committee, 2012). The recent EF recommendations provided more enforceable guidelines based on the understanding of regional integrated ecological regime. It set the required amount of flow that has to pass downstream at 18 streams locations so as to maintain at least the subsistence flow condition over the delta and bay (Table A.1). The recent recommendations included not only the flow amount, but also the attainment frequency for restoring a seasonal pulse of tidal-freshwater in order to ensure the implementation of the guidelines.

A.4 Role of the Frehd model for restoring the Nueces Delta

The Frehd code (Chapter 3) has been applied into the recent restoration efforts for the Nueces Delta (e.g., Li and Hodges, 2015). While the recent restoration efforts constructed the pipelines and pumps for freshwater water supply and established the EF recommendations, but it did not provide operating plans for local infrastructures (Hodges et al., 2012). The EF recommendations provided annual total freshwater inflow to the Nueces Bay (Table A.1), but not freshwater inflow required for the Nueces Delta separately. Therefore, establishing a practical operating plan at local scale needs an additional study evaluating the effect of freshwater inflow, and here is a need of a reliable tool for hydrodynamic modeling. The Frehd code has the ease and stability in hydrodynamic, which makes it a tool for investigating an optimal freshwater inflow plan to maximize the ecological efficiency (Hodges et al., 2012).

One challenge for hydrodynamic modeling of the Nueces Delta that is a shallow tidal marsh with a highly complex terrain is unresolved small topographic de-

tails. For hydrodynamic modeling of the Nueces Delta, Frehd employed $15 \times 15\text{m}$ (e.g., [Hodges et al., 2012](#)) $\sim 30 \times 30\text{m}$ grid scale (e.g., [Li and Hodges, 2015](#)), which were rasterized from the $1 \times 1\text{m}$ grid-scale lidar-derived bathymetric data by J. Gibeaut(2010). The observation of the $1 \times 1\text{m}$ grid resolution bathymetric data of the Nueces Delta indicates the presence of high spatial variability in bottom topography of shallow marshlands (e.g., sediment bars), which makes use of a smooth bottom boundary for subgrid areas hard to be rationalized. A fine-grid model is arguably not feasible for a multi-scenario simulation in a large water basin with dimension up to 100km^2 ([Ryan, 2011](#)), and a processor solving a matrix of large-scale flow mechanics is not easily accessible for a modeler.

Neglect of topographic forcing caused by subgrid topographic details can restrict model fidelity in addressing wetting and drying processes in shallow flow (e.g., flow volume, time-space coverage, rate, and route) ([Tsubaki and Kawahara, 2013](#); [Yu and Lane, 2011](#)). Considering the tidal fluctuations in the delta, wetting and drying process is a key process in hydrodynamics with respect to the regional ecological functioning. Therefore, addressing the effect of unresolved topographic features is a key task for the application of Frehd into exploring flow dynamics in the shallow complex terrain of the Nueces Delta. The prior Frehd model for the Nueces Delta used roughness parameters that were determined from the land-cover legend (e.g., 2001 National Land Cover Dataset) and the Manning's coefficient n conversion ([Hossain et al., 2009](#)). Using a friction parameter estimated from the lumped land-cover classes arguably provides uncertainty since it does not represent physical processes induced by local surface roughness and topographic forcing. Moreover, the

roughness parameter was set on a coarser grid scale than the model grid scale (i.e., land-cover data was built at $30\times 30\text{m}$ grid scale that is coarser than the model grid scale ($15\times 15\text{m} \sim 30\times 30\text{m}$)). These circumstances provided a motivation for the current work, which is developing a subgrid method to incorporate the effect of local forcing exerted by subgrid topography into a coarse-grid solution.

Appendix B

Free-surface Solution Applying the Flux Integration Approach for the flow continuity

B.1 Flow continuity equation

The mass conservative relationship for the integrated net fluxes (Q) at the faces of the grid cell (Casulli, 2009) provides the new flow continuity equation, Eqs. (5.14) ~ (5.17). Applying θ weighting method into Eq. (5.17) and assuming $A^{n+1} \simeq A^n$ provides

$$\frac{[(A_{xy}^{n+1})_{i,j}\eta_{i,j}^{n+1} - (A_{xy}^n)_{i,j}\eta_{i,j}^n]}{\Delta t} \left[\begin{aligned} & \left[u_{i+1/2,j}^{n+1/2} (A_{yz}^{n+1/2})_{i+1/2,j} - u_{i-1/2,j}^{n+1/2} (A_{yz}^{n+1/2})_{i-1/2,j} \right] \\ & \left[v_{i,j+1/2}^{n+1/2} (A_{xz}^{n+1/2})_{i,j+1/2} - v_{i,j-1/2}^{n+1/2} (A_{xz}^{n+1/2})_{i,j-1/2} \right] \end{aligned} \right] = 0$$

Arranging the equation above follows

$$\begin{aligned} & (A_{xy}^n)_{i,j}\eta_{i,j}^{n+1} - (A_{xy}^n)_{i,j}\eta_{i,j}^n + \theta_c \Delta t \left[u_{i+1/2,j}^{n+1} (A_{yz}^n)_{i+1/2,j} - u_{i-1/2,j}^{n+1} (A_{yz}^n)_{i-1/2,j} \right] \\ & + \theta_c \Delta t \left[v_{i,j+1/2}^{n+1} (A_{xz}^n)_{i,j+1/2} - v_{i,j-1/2}^{n+1} (A_{xz}^n)_{i,j-1/2} \right] \\ & + (1 - \theta_c) \Delta t \left[u_{i+1/2,j}^n (A_{yz}^n)_{i+1/2,j} - u_{i-1/2,j}^n (A_{yz}^n)_{i-1/2,j} \right] \\ & + (1 - \theta_c) \Delta t \left[v_{i,j+1/2}^n (A_{xz}^n)_{i,j+1/2} - v_{i,j-1/2}^n (A_{xz}^n)_{i,j-1/2} \right] \\ & = \Delta t T_{i,j}^{n+1/2} \end{aligned}$$

where $T_{i,j}^{n+1/2}$ represents all external volume sources (e.g., inflow, pump).

Let define an explicit source term (S) as:

$$\begin{aligned} S_{i,j}^n &\equiv \Delta t \left[u_{i+1/2,j}^n (A_{yz}^n)_{i+1/2,j} - u_{i-1/2,j}^n (A_{yz}^n)_{i-1/2,j} \right] \\ &\quad + \Delta t \left[v_{i,j+1/2}^n (A_{xz}^n)_{i,j+1/2} - v_{i,j-1/2}^n (A_{xz}^n)_{i,j-1/2} \right] \end{aligned}$$

Substituting S for the explicit source terms and rearranging the equation provides

$$\begin{aligned} &\eta_{i,j}^{n+1} (A_{xy}^n)_{i,j} - \eta_{i,j}^n (A_{xy}^n)_{i,j} + (1 - \theta_c) S_{i,j}^n \\ &\quad + \theta_c \Delta t \left[u_{i+1/2,j}^{n+1} (A_{yz}^n)_{i+1/2,j} - u_{i-1/2,j}^{n+1} (A_{yz}^n)_{i-1/2,j} \right] \\ &\quad + \theta_c \Delta t \left[v_{i,j+1/2}^{n+1} (A_{xz}^n)_{i,j+1/2} - v_{i,j-1/2}^{n+1} (A_{xz}^n)_{i,j-1/2} \right] \\ &= \Delta t T_{i,j}^{n+1/2} \end{aligned}$$

The flow continuity equation is reduced as:

$$\begin{aligned} \eta_{i,j}^{n+1} + \theta_c \frac{\Delta t}{(A_{xy}^n)_{i,j}} \left[u_{i+1/2,j}^{n+1} (A_{yz}^n)_{i+1/2,j} - u_{i-1/2,j}^{n+1} (A_{yz}^n)_{i-1/2,j} \right] \\ + \theta_c \frac{\Delta t}{(A_{xy}^n)_{i,j}} \left[v_{i,j+1/2}^{n+1} (A_{xz}^n)_{i,j+1/2} - v_{i,j-1/2}^{n+1} (A_{xz}^n)_{i,j-1/2} \right] \\ = \eta_{i,j}^n - (1 - \theta_c) \frac{S_{i,j}^n}{(A_{xy}^n)_{i,j}} + \frac{\Delta t}{(A_{xy}^n)_{i,j}} T_{i,j}^{n+1/2} \end{aligned} \quad (\text{B.1})$$

B.2 Momentum conservation equation

The first-order upwind discretized momentum equation is stated as:

$$h_{i+1/2,j}^n u_{i+1/2,j}^{n+1} = h_{i+1/2,j}^n E_{x \ i+1/2,j}^n - I_{i+1/2,j}^n h_{i+1/2,j}^n \frac{g \Delta t}{\Delta x} (\eta_{i+1,j}^{n+1} - \eta_{i,j}^{n+1}) \quad (\text{B.2})$$

where E is the sum of the explicit terms (advection term N , diffusive friction term D_{xx} and D_{yx}) as:

$$E_{x \ i+1/2,j}^n \equiv I_{i+1/2,j}^n (u_{i+1/2,j}^n - \Delta t N_{x \ i+1/2,j}^n + \Delta t D_{xx \ i+1/2,j}^n + \Delta t D_{yx \ i+1/2,j}^n)$$

$$N_{x \ i+1/2,j}^n = u_{i+1/2,j}^n \frac{(u_{i+1/2,j}^n - u_{i-1/2,j}^n)}{\Delta x} + v_{i+1/2,j}^n \frac{(u_{i+1/2,j}^n - u_{i+1/2,j-1}^n)}{\Delta y}$$

$$D_{xx \ i+1/2,j}^n = \frac{1}{\Delta x} \left[(\nu_x)_{i+3/2,j} \frac{(u_{i+3/2,j}^n - u_{i+1/2,j}^n)}{\Delta x} - (\nu_x)_{i+1/2,j} \frac{(u_{i+1/2,j}^n - u_{i-1/2,j}^n)}{\Delta x} \right]$$

where ν is horizontal turbulence eddy viscosity. $D_{yx \ i+1/2,j}^n$ is discretized similarly.

Further define I as:

$$I_{i+1/2,j}^n \equiv \frac{1}{1 - \Delta t B_{x \ i+1/2,j}^n}$$

where

$$B_{x \ i+1/2,j}^n = \frac{1}{2h_{i+1/2,j}^n} C_D \sqrt{[(u_{i+1/2,j}^n)^2 + (v_{i+1/2,j}^n)^2]}$$

Arranging Equation (B.2) provides,

$$u_{i+1/2,j}^{n+1} = E_{x \ i+1/2,j}^n - I_{i+1/2,j}^n \frac{g\Delta t}{\Delta x} (\eta_{i+1,j}^{n+1} - \eta_{i,j}^{n+1}) \quad (\text{B.3})$$

B.3 Free-surface elevation solution

Substituting $u_{i+1/2,j}^{n+1}$ in Eq. (B.3) into Eq. (B.1) provides

$$\begin{aligned}
\eta_{i,j}^{n+1} + \theta_c \frac{\Delta t}{(A_{xy}^n)_{i,j}} & \left[E_{x \ i+1/2,j}^n - I_{i+1/2,j}^n \frac{g\Delta t}{\Delta x} (\eta_{i+1,j}^{n+1} - \eta_{i,j}^{n+1}) \right] (A_{yz}^n)_{i+1/2,j} \\
& - \theta_c \frac{\Delta t}{(A_{xy}^n)_{i,j}} u_{i-1/2,j}^{n+1} (A_{yz}^n)_{i-1/2,j} \\
& + \theta_c \frac{\Delta t}{(A_{xy}^n)_{i,j}} \left[v_{i,j+1/2}^{n+1} (A_{xz}^n)_{i,j+1/2} - v_{i,j-1/2}^{n+1} (A_{xz}^n)_{i,j-1/2} \right] \\
& = \eta_{i,j}^n - (1 - \theta_c) \frac{S_{i,j}^n}{(A_{xy}^n)_{i,j}} + \frac{\Delta t}{(A_{xy}^n)_{i,j}} T_{i,j}^{n+1/2}
\end{aligned} \tag{B.4}$$

$u_{i-1/2,j}^{n+1}$, $v_{i,j+1/2}^{n+1}$, and $v_{i,j-1/2}^{n+1}$ can be substituted similarly.

For further simplicity in exposition, let

$$\begin{aligned}
C_{i+1/2,j}^n & \equiv g(\Delta t)^2 \frac{(A_{yz}^n)_{i+1/2,j}}{\Delta x (A_{xy}^n)_{i,j}} I_{i+1/2,j}^n \\
C_{i-1/2,j}^n & \equiv g(\Delta t)^2 \frac{(A_{yz}^n)_{i-1/2,j}}{\Delta x (A_{xy}^n)_{i,j}} I_{i-1/2,j}^n \\
C_{i,j+1/2}^n & \equiv g(\Delta t)^2 \frac{(A_{xz}^n)_{i,j+1/2}}{\Delta x (A_{xy}^n)_{i,j}} I_{i,j+1/2}^n \\
C_{i,j-1/2}^n & \equiv g(\Delta t)^2 \frac{(A_{xz}^n)_{i,j-1/2}}{\Delta x (A_{xy}^n)_{i,j}} I_{i,j-1/2}^n
\end{aligned}$$

and

$$\begin{aligned}
G_{i,j}^n & \equiv \frac{\Delta t}{(A_{xy}^n)_{i,j}} \left[E_{x \ i+1/2,j}^n (A_{yz}^n)_{i+1/2,j} - E_{x \ i-1/2,j}^n (A_{yz}^n)_{i-1/2,j} \right] \\
& + \frac{\Delta t}{(A_{xy}^n)_{i,j}} \left[E_{y \ i,j+1/2}^n (A_{xz}^n)_{i,j+1/2} - E_{y \ i,j-1/2}^n (A_{xz}^n)_{i,j-1/2} \right]
\end{aligned}$$

Substituting C and G into Eq. (B.4), the free-surface solution is derived in a

form that is similar to Eq. (3.9).

$$\begin{aligned}
& \eta_{i,j}^{n+1} \left(1 + C_{i+1/2,j}^n + C_{i-1/2,j}^n + C_{i,j+1/2}^n + C_{i,j-1/2}^n \right) \\
& - \eta_{i+1,j}^{n+1} C_{i+1/2,j}^n - \eta_{i-1,j}^{n+1} C_{i-1/2,j}^n - \eta_{i,j+1}^{n+1} C_{i,j+1/2}^n - \eta_{i,j-1}^{n+1} C_{i,j-1/2}^n \\
& = \eta_{i,j}^n - (1 - \theta_c) \frac{S_{i,j}^n}{(A_{xy}^n)_{i,j}} + \frac{\Delta t}{(A_{xy}^n)_{i,j}} T_{i,j}^{n+1/2} - G_{i,j}^n
\end{aligned} \tag{B.5}$$

Appendix C

Definition of Subgrid Quantities for New Subgrid Model

The new subgrid model (Chapter 5) requires subgrid topographic quantities A_{xy} , A_{xz} , A_{yz} , and V corresponding to time-varying model-resolved free-surface elevation (η) to be known. We can consider a fine-grid system whose outer cells share a boundary with a model-resolved grid cell for the subgrid region (Section 4.2.2).

Equation (4.13) provides the time-varying difference between the fine-grid bottom and coarse-grid bottom ($\delta z(r, s, t)$) as :

$$\delta z(r, s, t) \equiv \min [z_b(r, s) - Z_b, h(t)]$$

with a fine-grid topographic elevation $z_b(r, s)$, a coarse-grid bottom elevation Z_b that is uniform over subgrid space, and the time-varying model-resolved water depth h . It follows that the subgrid depth h_f at the time t , Eq. (4.14):

$$h_f(r, s, t) = h(t) - \delta z(r, s, t)$$

Where for some position r or s along the fine-grid axes (r, s) , time-varying difference of cross-sectional area between the fine-grid and coarse-grid system (ξ) is

$$\xi_x(r, t) \equiv \sum_{s=1}^{n_s} \delta z(r, s, t) \Delta s$$

or

$$\xi_y(s, t) \equiv \sum_{r=1}^{n_r} \delta z(r, s, t) \Delta r$$

where Δr and Δs are the unit lengths of a fine-grid cell for r and s -directions; and n_r and n_s are the numbers of fine-grid cells of the fine-grid axes (r, s) respectively. The cross-sectional flow areas A_{fx} and A_{fy} where for some position r and s along the fine-grid axes (r, s) are defined as:

$$A_{fx}(r, t) \equiv h(t) \Delta y - \xi_x(r, t)$$

and

$$A_{fy}(s, t) \equiv h(t) \Delta x - \xi_y(s, t)$$

where Δx and Δy are the discretized unit lengths of a model-resolved grid cell for x and y -directions, respectively.

The flow area of the grid cell (i, j) is assigned with a smaller area between the face flow areas of two neighboring grid cells at their common face. It follows that the face area $A_{yz}(t)$ is determined with a smaller flow area between those of two neighboring grid cells (i, j) and ($i + 1, j$) as:

$$A_{yz(i,j)}(t) \equiv \min [A_{fx(i,j)}(r = n_r, t), A_{fx(i+1,j)}(r = 1, t)]$$

Similarly, the flow area $A_{xz}(t)$ is determined as:

$$A_{xz(i,j)}(t) \equiv \min [A_{fy(i,j)}(s = n_s, t), A_{fy(i,j+1)}(s = 1, t)]$$

The cell water volume V and the effective surface area A_{xy} are determined at the center of a grid cell as:

$$V(t) \equiv \sum_{r=1}^{n_r} A_{fx}(r, t) \Delta r$$

$$A_{xy}(t) \equiv \frac{V(t)}{h(t)}$$

Note that A_{xy} set to be $\Delta x \Delta y$ when $h(t) = 0$. It prevents from making inflow boundary elevation have infinity, since Frehd's approach to an inflow boundary is to distribute the flow proportionally with the local area (i.e., $\eta_{BC} = Q_{BC}/A_{xy}$).

Appendix D

Look-up Table Scheme

The new subgrid model (Chapter 5) requires geometric data of each grid cell corresponding to the surface elevation (η). Computing a continuous range of geometric values for each grid cell can be expensive, especially when the modeling domain consists of a large number of cells. A “look-up table” method has been used in prior subgrid model studies (e.g., Wu et al., 2016; Li, 2015) in order to reduce the computational expenses associated with the computation of geometric quantities required for parameterizing the effect of subgrid topography. In the look-up table method, subgrid geometric quantities for each grid cell are computed at pre-defined increments of $\Delta\eta$, stored, and fed back to a model at each time-step corresponding to the modeled surface elevation η .

The look-up table in the current study stored four subgrid geometric quantities for each resolved grid cell, which were A_{yz} , A_{xz} , V , and $\overline{h_f}$ (Chapter 5). Note that the effective surface area A_{xy} was not stored in the look-up table, and was determined by dividing V_l fed by the look-up table with the modeled depth h at each time-step.

Let $\eta_l(k)$ is a set of the surface elevations that are determined by incrementing $k \Delta\eta$ (i.e., $\eta_l(k) = \min \eta_l + k \times \Delta\eta$; $k = \{1, \dots, N_l\}$). The geometric quantities in the

look-up table corresponding to $\eta_l(k)$ are denoted as $A_{yz(l)}(k)$, $A_{xz(l)}(k)$, $V_l(k)$, and $\overline{h_{f(l)}}(k)$, respectively. The current work set the length and range of η_l (i.e., N_l and $\min \eta_l$) by referring to the highest and lowest elevations of the test domain.

The depth at the fine-grid coordinates (r, s) at $\eta_l(k)$ is determined as:

$$h_l(r, s, k) = \min [\eta_l(k) - z_b(r, s), 0]$$

where z_b is the fine-grid elevation, and the $\min[\]$ function ensures that the geometric quantities do not include negative depth, area, or volume. It defines the average fine-grid depth and water volume at k th interval as:

$$\overline{h_{f(l)}}(k) = \frac{1}{n_r n_s} \sum_{r=1}^{n_r} \sum_{s=1}^{n_s} h_l(r, s, k)$$

where n_r and n_s are the numbers of fine-grid cells in the fine-grid coordinates (r, s) .

$$V_l(k) = \sum_{r=1}^{n_r} \sum_{s=1}^{n_s} h_l(r, s, k) \Delta s \Delta r$$

where Δr and Δs are the discretized unit lengths of a fine-grid cell.

The cross-sectional flow areas $A_{fx(l)}$ and $A_{fy(l)}$ where for some position r and s along the fine-grid axes (r, s) are defined at $\eta_l(k)$ as:

$$A_{fx(l)}(r, k) = \sum_{s=1}^{n_s} h_l(r, s, k) \Delta s$$

$$A_{fy(l)}(s, k) = \sum_{r=1}^{n_r} h_l(r, s, k) \Delta r$$

The face flow area of the grid cell (i, j) corresponding to $\eta_l(k)$ is assigned with a smaller area between the face flow areas of two grid cells (i, j) and $(i + 1, j)$ or $(i, j + 1)$, which is denoted as $A_{yz(l)}(k)$ or $A_{xz(l)}(k)$.

$$A_{yz(l)}(k) \equiv \min [(A_{fx(l)})_{i,j}(r = n_r, k), (A_{fx(l)})_{i+1,j}(r = 1, k)]$$

$$A_{xz(l)}(k) \equiv \min [(A_{fy(l)})_{i,j}(s = n_s, k), (A_{fy(l)})_{i,j+1}(s = 1, k)]$$

A look-up table storing subgrid geometric values at a small interval of the free surface elevation is preferred for model fidelity, but it degrades the effectiveness of the method. The current study simply added a linear interpolation function to the prior algorithm of [Li \(2015\)](#) in order to improve the effectiveness of the look-up table method. With the modeled surface elevation η^n at n th time-step, let $\eta_l(\alpha)$ is the closest elevation to η^n , which is determined by incrementing $\alpha \Delta\eta$, and $\theta_l(k)$ ($k = \{1, \dots, N_l\}$) is the subgrid geometric quantity stored in the table at the k th interval of $\Delta\eta$. The linearly-interpolated quantity corresponding to the modeled surface elevation η^n (θ^n) is determined as:

$$\theta^{n+1} = \theta_l(\alpha) + \frac{\eta^n - \eta_c}{\Delta\eta} \theta_l(\alpha)$$

Bibliography

- Abu-Aly, T. R., G. B. Pasternack, J. R. Wyrick, R. Barker, D. Massa, and T. Johnson, “Effects of LiDAR-derived, spatially distributed vegetation roughness on two-dimensional hydraulics in a gravel-cobble river at flows of 0.2 to 20 times bank full”, *Geomorphology*, 206:468–482, 2014.
- Aizinger, V., J. Proft, C. Dawson, D. Pothina, and S. Negusse, “A three-dimensional discontinuous Galerkin model applied to the baroclinic simulation of Corpus Christi Bay”, *Ocean Dynamics*, 63:89–113, 2013.
- Anderson, M. G. and P. D. Bates, “Model Validation: Perspectives in Hydrological Science, Edited by Anderson, Malcolm G. and Bates, Paul D.”, John Wiley & Sons, 2001.
- Asquith, W. H., J. G. Mosier, and P. W. Bush, “Status, Trends and Changes in Freshwater Inflows to Bay Systems in the Corpus Christi Bay National Estuary Program Area”, Coastal Bend Bays & Estuaries Program, 1997.
- Begnudelli, L. and B. F. Sanders, “Conservative Wetting and Drying Methodology for Quadrilateral Grid Finite-Volume Models”, *Journal of Hydraulic Engineering*, 133(3):312–322, 2007.
- Blöschl, G. and R. Grayson, “Chapter 2. Spatial Observation and Interpolation, Spa-

- tial Patterns in Catchment Hydrology: Observation and Modeling”, Cambridge University Press, 2001.
- Bradsby, C. B., “The Environmental Flows Allocation Process”, Texas Water Law Institute, 2009.
- Buckman, L., “Hydrodynamics of Partially vegetated channels: stem drag forces and application to an in-stream wetland concept for tropical, urban drainage systems, MSc thesis report”, Delft University of Technology & National University of Singapore, 2013.
- Carney, S. K., B. P. Bledsoe, and D. Gessler, “Representing the bed roughness of coarse-grained streams in computational fluid dynamics”, *Earth Surface Processes and Landforms*, 31:736–749, 2006.
- Casas, A., S. N. Lane, D. Yu, and G. Benito, “A method for parameterizing roughness and topographic sub-grid scale effects in hydraulic modelling from LiDAR data”, *Hydrology and Earth System Sciences (HESS) & Discussions (HESSD)*, 2010.
- Casulli, V., “A semi-implicit finite difference method for non-hydrostatic, free-surface flows”, *International Journal for Numerical Methods in Fluids*, 30(4):425–440, 1999.
- Casulli, V., “A high-resolution wetting and drying algorithm for free-surface hydrodynamics”, *International Journal for Numerical Methods in Fluids*, 60(4):391–408, 2009.

- Casulli, V. and E. Cattani, “Stability, accuracy and efficiency of a semi-implicit method for three-dimensional shallow water flow”, *Computers & Mathematics with Applications*, 27(4):99–112, 1994.
- Casulli, V. and R. T. Cheng, “Semi-implicit finite difference methods for three-dimensional shallow water flow”, *International Journal for Numerical Methods in Fluids*, 15(6):629–648, 1992.
- Casulli, V. and P. Zanolli, “Semi-implicit numerical modeling of nonhydrostatic free-surface flows for environmental problems”, *Mathematical and computer modelling*, 36(9):1131–1149, 2002.
- Cea, L. and M. E. Vázquez-Cendón, “Unstructured finite volume discretization of two-dimensional depth-averaged shallow water equations with porosity”, *International Journal for Numerical Methods in Fluids*, 63(8):903–930, 2010.
- Chen, A. S., B. Evans, S. Djordjević, and D. A. Savić, “A coarse-grid approach to representing building blockage effects in 2D urban flood modelling”, *Journal of Hydrology*, 426:1–16, 2012.
- Chisolm, R. E., “The effect of grid scale on the calibration of two-dimensional river models through the drag coefficient”, Master’s thesis, The University of Texas at Austin, USA, 2011.
- Crowder, D. W. and P. Diplas, “Using two-dimensional hydrodynamic models at scales of ecological importance”, *Journal of Hydrology*, 230(3):172–191, 2000.

- D'Alpaos, L. and A. Defina, “Mathematical modeling of tidal hydrodynamics in shallow lagoons: A review of open issues and applications to the Venice lagoon”, *Computers & Geosciences*, 33(4):476496, 2007.
- Defina, A., “Two-dimensional shallow flow equations for partially dry areas”, *Water Resources Research*, 36(11):3251–3264, 2000.
- Dias, J. a. M., J. M. Valentim, and M. C. Sousa, “A numerical study of local variations in tidal regime of Tagus Estuary, Portugal”, *PLoS one*, 8(12):e80450, 2013.
- Ding, Y., Y. Jia, and S. S. Wang, “Identification of Manning’s roughness coefficients in shallow water flows”, *Journal of Hydraulic Engineering*, 130(6):501–510, 2004.
- Dottori, F. and E. Todini, “Testing a simple 2D hydraulic model in an urban flood experiment”, *Hydrological Processes*, 27(9):1301–1320, 2013.
- Dottori, F., G. D. Baldassarre, and E. Todini, “Detailed data is welcome, but with a pinch of salt: Accuracy, precision, and uncertainty in flood inundation modeling”, *Water Resources Research*, 49(9):6079–6085, 2013.
- Guadalupe, San Antonio, Mission, and Aransas Rivers and Mission, Copano, Aransas, and San Antonio Bays Basin and Bay Expert Science Team, “Environmental Flows Recommendations Report, Final Submission to the Environmental Flows Advisory Group, Nueces River and Corpus Christi and Baffin Bays Basin and Bay Area Stakeholders Committee, and Texas Commission on Environ-

- mental Quality”, Available at http://www.tceq.texas.gov/permitting/water_rights/eflows, 2011.
- Guinot, V. and S. Spares-Frazão, “Flux and source term discretization in two-dimensional shallow water models with porosity on unstructured grids”, *International Journal for Numerical Methods in Fluids*, 50(3):309–345, 2006.
- Hardy, R. J., P. D. Bates, and M. G. Anderson, “The importance of spatial resolution in hydraulic models for floodplain environments”, *Journal of Hydrology*, 216(1):124–136, 1999.
- Hervouet, J., “Hydrodynamics of free surface flows: modelling with the finite element method”, John Wiley & Sons, 2007.
- Hicks, D. M. and P. D. Mason, “Roughness characteristic of New Zealand rivers: a handbook for assigning hydraulic roughness coefficients to river reaches by the “visual comparison” approach”, Water Resources Survey, 1991.
- Hill, E. M., J. W. Tunnell, and L. Lloyd, “Spatial Effects of Rincon Bayou Pipeline freshwater inflows on salinity in the lower Nueces Delta, Texas”, Coastal Bend Bays & Estuaries Program, 2012.
- Hill, E. M., J. W. Tunnell, and B. A. Nicolau, “Spatial and temporal effects of the Rincon Bayou Pipeline on hypersaline conditions in the Lower Nueces Delta, Texas, USA”, *Texas Water Journal*, 6(1):11–32, 2015.
- Hodges, B. R., “Accuracy order of crank-nicolson discretization for hydrostatic free surface flow”, *Journal of Engineering Mechanics*, 130(8):904–910, 2004.

- Hodges, B. R., “Representing hydrodynamically important blocking features in coastal or riverine lidar topography”, *Natural Hazards and Earth System Sciences*, 15(5):1011–1023, 2015.
- Hodges, B. R. and F. J. Rueda, “Semi-implicit two-level predictor-corrector methods for non-linearly coupled, hydrostatic, barotropic/baroclinic flows”, *International Journal of Computational Fluid Dynamics*, 22(9):593–607, 2008.
- Hodges, B. R., J. Imberger, A. Saggio, and K. B. Winters, “Modeling basin-scale internal waves in a stratified lake”, *Limnology and oceanography*, 45(7):1603–1620, 2000.
- Hodges, B. R., K. H. Dunton, P. A. Montagna, and G. H. Ward, “Nueces Delta Restoration Study”, Coastal Bend Bays & Estuaries Program, 2012.
- Horritt, M. S., “Chapter 9. Parameterisation, validation and uncertainty analysis of CFD models of fluvial and flood hydraulics in the natural environment”, In Bates, P. D., S. N. Lane, and R. I. Ferguson, editors, “Computational Fluid Dynamics”, pages 193–213. John Wiley & Sons, 2005.
- Horritt, M. S. and P. D. Bates, “Effects of spatial resolution on a raster based model of flood flow”, *Journal of Hydrology*, 253(1):239–249, 2001.
- Horton, R. E., “Separate roughness coefficients for channel bottom and sides”, *Engineering News Record*, 111(22):652–653, 1933, (recited from [Woo \(2001\)](#)).

- Hossain, A. A., Y. Jia, and X. Chao, “Estimation of Manning’s roughness coefficient distribution for hydrodynamic model using remotely sensed land cover features”, In “2009 17th International Conference on Geoinformatics”. IEEE, 2009.
- Hughes, J. D., J. D. Deckerb, and C. D. Langevinc, “Use of upscaled elevation and surface roughness data in two-dimensional surface water models”, *Advances in Water Resources*, 34(9):11511164, 2011.
- Huthoff, F., D. Augustijn, and S. J. Hulscher, “Analytical solution of the depth-averaged flow velocity in case of submerged rigid cylindrical vegetation”, *Water Resources Research*, 43(6), 2007.
- Ji, Z., “Hydrodynamics and Water Quality: Modeling Rivers, Lakes, and Estuaries”, John Wiley & Sons, 2008.
- Jiang, Y. W. and O. W. H. Wai, “Drying-wetting approach for 3d finite element sigma coordinate model for estuaries with large tidal flats”, *Advances in Water Resources*, 28:779–792, 2005.
- Kärnä, T., A. M. Baptista, J. E. Lopez, P. J. Turner, C. McNeil, and T. B. Sanford, “Numerical modeling of circulation in high-energy estuaries: A Columbia River estuary benchmark”, *Ocean Modelling*, 88:54–71, 2015.
- Knock, C. and S. C. Ryrie, “Parameterization of dispersion in the depth-averaged transport equation”, *Applied mathematical modelling*, 18(10):582–587, 1994.

- Lambrechts, J., E. Hanert, E. Deleersnijder, P. Bernard, V. Legat, J. Remacle, and E. Wolanski, “A multi-scale model of the hydrodynamics of the whole Great Barrier Reef”, *Estuarine, Coastal and Shelf Science*, 79(1):143151, 2008.
- Lane, S. N., R. J. Hardy, L. Elliott, and D. B. Ingham, “Numerical modeling of flow processes over gravelly surfaces using structured grids and a numerical porosity treatment”, *Water Resources Research*, 40(1), 2004.
- Lane, S. N., “Roughness-time for a re-evaluation?”, *Earth Surface Processes and Landforms*, 30(2):251–253, 2005.
- Lellis-Dibble, K. A., K. E. McGlynn, and T. E. Bigford, “Estuarine fish and shellfish species in US commercial and recreational fisheries: economic value as an incentive to protect and restore astatine habitat”, National Oceanic and Atmospheric Administration, National Marine Fisheries Service, Office of Habitat Conservation, Habitat Protection Division, 2008.
- Li, Z., “Area-based subgrid model for Fine Grid Resolution Environmental Hydrodynamic Fluids Model”, *Manuscript in preparation*, 2015.
- Li, Z. and B. R. Hodges, “Modeling Salinity Fluxes in the Nueces Delta”, Texas Water Development Board, 2015.
- Liang, Q. and A. G. Borthwick, “Adaptive quadtree simulation of shallow flows with wet-dry fronts over complex topography”, *Computers & Fluids*, 38(2):221–234, 2009.

- Lightbody, A. F. and H. M. Nepf, “Prediction of velocity profiles and longitudinal dispersion in emergent salt marsh vegetation”, *Limnology and Oceanography*, 51(1):218–228, 2006.
- Liu, Y., P. MacCready, B. M. Hickey, E. P. Dever, P. M. Kosro, and N. S. Banas, “Evaluation of a coastal ocean circulation model for the Columbia River plume in summer 2004”, *Journal of Geographical Research: Oceans*, 114(C2), 2009.
- Lotter, G. K., “Considerations of hydraulic design of channels with different roughness walls”, *Transactions, All-Union Scientific Research Institute of Hydraulic Engineering*, Leningrad 9:238–241, 1933, (recited from [Yang et al. \(2005\)](#)).
- Mallard, G., K. Dickson, T. Hardy, C. Hubbs, D. Maidment, J. Martin, P. McDowell, B. Richter, G. Wilkerson, K. Winemiller, and D. Woolhiser, “The science of in-stream flows: a review of the Texas Instream Flow Program”, National Academies Press, 2005.
- McMillan, H. K. and J. Brasington, “Reduced complexity strategies for modelling urban floodplain inundation”, *Geomorphology*, 90(3):226–243, 2007.
- Montagna, P. A., E. M. Hill, and B. Moulton, “Role of science-based and adaptive management in allocating environmental flows to the Nueces Estuary, Texas, USA”, *WIT Transactions on Ecology and the Environment*, 122, 2009a.
- Montagna, P. A., T. Palmer, M. Gil, E. Hill, B. Nicolau, and K. Dunton, “Response of the Nueces estuarine marsh system to Freshwater Inflow: an integrative data

- synthesis of baseline conditions for faunal communities”, Coastal Bend Bays & Estuaries Program, 2009b.
- Morvan, H., D. Knight, N. Wright, X. Tang, and A. Crossley, “The concept of roughness in fluvial hydraulics and its formulation in 1D, 2D and 3D numerical simulation models”, *Journal of Hydraulic Research*, 46(2):191–208, 2008.
- Néelz, S. and G. Pender, “Sub-grid scale parameterisation of 2D hydrodynamic models of inundation in the urban area”, *Acta Geophysica*, 55(1):65–72, 2007.
- Nicholas, A. P. and C. A. Mitchell, “Numerical simulation of over bank processes in topographically complex floodplain environments”, *Hydrological Processes*, 17(4): 727–746, 2003.
- Nueces River and Corpus Christi and Baffin Bay Basin and Bay Area Stakeholder Committee, “Environmental Flow Standards and Strategies Recommendations Report, Final Submission to the Environmental Flows Advisory Group and the Texas Commission on Environmental Quality”, Available at http://www.tceq.texas.gov/permitting/water_rights/eflows, 2012.
- Özgen, I., K. Teuber, F. Simons, D. Liang, and R. Hinkelmann, “Upscaling the shallow water model with a novel roughness formulation”, *Environmental Earth Sciences*, 74(11):7371–7386, 2015.
- Pasternack, G. B., A. T. Gilbert, J. M. Wheaton, and E. M. Buckland, “Error propagation for velocity and shear stress prediction using 2D models for environmental management”, *Journal of Hydrology*, 328(1):227–241, 2006.

- Platzek, F. W., G. S. Stelling, J. A. Jankowski, R. Patzwahl, and J. D. Pietrzak, “An efficient semi-implicit subgrid method for free-surface flows on hierarchical grids”, *International Journal For Numerical Methods In Fluids*, 80:715–741, 2015.
- Poff, N. L., J. D. Allan, M. B. Bain, J. R. Karr, K. L. Prestegard, B. D. Richter, R. E. Sparks, and J. C. Stromberg, “The natural flow regime: A paradigm for river conservation and restoration”, *BioScience*, 47:769–784, 1997.
- Rasser, M. K., “The role of biotic and abiotic processes in the zonation of salt marsh plants in the Nueces River Delta, Texas”, PhD dissertation, The University of Texas at Austin, USA, 2009.
- Rosatti, G., C. D., and L. Bonaventura, “Semi-implicit, semi-Lagrangian modelling for environmental problems on staggered Cartesian grids with cut cells”, *Journal of Computational Physics*, 204(1):353–377, 2005.
- Rueda, F. J., E. Sanmiguel-Rojas, and B. R. Hodges, “Baroclinic stability for a family of two-level semi-implicit numerical methods for the 3D shallow water equations”, *International Journal of Numerical Methods in Fluids*, 54(3):237–268, 2007.
- Ryan, A. J. and B. R. Hodges, “Modeling hydrodynamic fluxes in the Nueces River Delta”, Coastal Bend Bays & Estuaries Program, 2011.
- Ryan, A. J., “Modeling hydrodynamic fluxes in the Nueces River Delta”, Master’s thesis, The University of Texas at Austin, USA, 2011.
- Sahoo, G. B., C. Ray, and E. H. De Carlo, “Calibration and validation of a physically distributed hydrological model, MIKE SHE, to predict streamflow at high

- frequency in a flashy mountainous Hawaii stream”, *Journal of Hydrology*, 327(1): 94–109, 2006.
- Schubert, J. E. and B. F. Sanders, “Building treatment for urban flood inundation models and implications for predictive skill and modeling efficiency”, *Advances in Water Resources*, 41:49–64, 2012.
- Science Advisory Committee, “Methodologies for establishing a freshwater inflow regime for Texas estuaries within the context of the Senate Bill 3 environmental flows process”, Texas Commission on Environmental Quality, 2009.
- Sehili, A., G. Lang, and C. Lippert, “High-resolution subgrid models: background, grid generation, and implementation”, *Ocean Dynamics*, 64(4):519–535, 2014.
- Smith, L. S. and Q. Liang, “Towards a generalised GPU/CPU shallow-flow modelling tool”, *Computers & Fluids*, 88:334–343, 2013.
- Stachelek, J. J., “Freshwater inflows in the Nueces Delta, TX: Impacts on porewater salinity and estimation of needs”, Master’s thesis, The University of Texas at Austin, USA, 2012.
- Stelling, G. S., “Quadtree flood simulations with sub-grid digital elevation models”, *Proceedings of the Institution of Civil Engineers*, 165(10):567, 2012.
- Stokes, G. G., “On the theories of the internal friction of fluids in motion, and of the equilibrium and motion of elastic solids”, *Transactions of American Geophysical Union*, 8:287–305, 1845.

- Tolan, J. M., “El Niño-Southern Oscillation impacts translated to the watershed scale: Estuarine salinity patterns along the Texas Gulf coast, 1982 to 2004”, *Estuarine, Coastal and Shelf Science*, 72(1):247–260, 2007.
- Tsubaki, R. and Y. Kawahara, “The uncertainty of local flow parameters during inundation flow over complex topographies with elevation errors”, *Journal of Hydrology*, 486:71–87, 2013.
- Tunnell, J. and L. Lloyd, “Effects of Rincon Bayou Pipeline Inflows on Salinity Structure Within the Nueces Delta, Texas”, Coastal Bend Bays & Estuaries Program, 2011.
- United States and Bureau of Reclamation, “Concluding Report: Rincon Bayou Demonstration Project”, United States Department of the Interior, Bureau of Reclamation: in cooperation with University of Texas Marine Science Institute, 2000.
- Volp, N. D., B. C. van Prooijen, and G. S. Stelling, “A finite volume approach for shallow water flow accounting for high-resolution bathymetry and roughness data”, *Water Resources Research*, 49(7):4126–4135, 2013.
- Volp, N. D., B. C. van Prooijen, J. D. Pietrzak, and G. S. Stelling, “A subgrid based approach for morphodynamic modelling”, *Advances in Water Resources*, 93:105–117, 2016.
- Wackernagel, H., “Geostatistical model, covariance structure and cokriging”, In “Statistics and Machine Learning Interface Meeting”, 2009.

- Wadzuk, B. M. and B. R. Hodges, “Isolation of non-hydrostatic regions within a basin”, In “17th ASCE Engineering Mechanics Conference”, 2004.
- Wang, S., Z. Zhang, G. Sun, P. Strauss, J. Guo, and Y. Tang, “Distributed hydrological modeling in a large-scale watershed of Northern China: Multi-site model calibration, validation, and sensitivity analysis”, *Hydrology and Earth System Sciences*, pages 5697–5727, 2012.
- White, F., “Viscous Fluid Flow”, McGraw-Hill series in mechanical engineering, 2006.
- Willmott, C. J., “On the validation of models”, *Physical Geography*, 2(2):184–194, 1981.
- Woo, H. S., “River Hydraulics”, Chengmundang, 2001.
- Wu, G., F. Shi, J. T. Kirby, R. Mieras, B. Liang, H. Li, and J. Shi, “A pre-storage, subgrid model for simulating flooding and draining processes in salt marshes”, *Coastal Engineering*, 108:65–78, 2016.
- Yang, K., S. Cao, and X. Liu, “Study on resistance coefficient in compound channels”, *Acta Mechanica Sinica*, 21(4):353–361, 2005.
- Yu, D. and S. N. Lane, “Urban fluvial flood modelling using a two-dimensional diffusion-wave treatment, part1: mesh resolution effects”, *Hydrological Processes*, 20(7):1541–1565, 2006a.

- Yu, D. and S. N. Lane, “Urban fluvial flood modelling using a two-dimensional diffusion-wave treatment, part2: development of a sub-grid-scale treatment”, *Hydrological Processes*, 20:1567–1583, 2006b.
- Yu, D. and S. N. Lane, “Interactions between subgrid-scale resolution, feature representation and grid-scale resolution in flood inundation modelling”, *Hydrological Processes*, 25:36–53, 2011.
- Zimmerman, R., T. Minello, and L. Rozas, “Salt marsh linkages to productivity of penaeid shrimps and blue crabs in the northern Gulf of Mexico”, In “Concepts and Controversies in Tidal Marsh Ecology”, pages 293–314. Springer, 2002.

Vita

Gihye Shin received her B.S. and M.S. degrees in Civil, Urban and Geosystem engineering from the Seoul National University, Seoul, South Korea. She has been working as an engineer for K-water since 2004, which is a government-owned corporation providing water service nationwide in South Korea. She started her Ph.D. study in the department of Civil, Architectural, and Environmental Engineering in August, 2010.

Permanent address: irisnow@utexas.edu

This dissertation was typeset with L^AT_EX[†] by the author.

[†]L^AT_EX is a document preparation system developed by Leslie Lamport as a special version of Donald Knuth's T_EX Program.